AJNTS

ALBANIAN JOURNAL OF NATURAL AND TECHNICAL SCIENCES

2026

31 (**3**)

PUBLISHED BY ACADEMY OF SCIENCES OF ALBANIA

PUBLISHED BY THE ACADEMY OF SCIENCES OF ALBANIA

AJNTS

ALBANIAN JOURNAL OF NATURAL AND TECHNICAL SCIENCES

2026
31 (3)

Aims and Scope

This Journal is a multidisciplinary publication devoted to all field of Natural and Technical Sciences. The Editor of AJNTS invites original contributions which should comprise previously unpublished results, data and interpretations. Types of contributions to be published are: (1) research papers; (2) shorts communications; (3) reviews; (4) discussions; (5) book reviews;(6) announcements

ISSN 2074-0867
EISSN 3135-1115

Graphic by: Dorina Muka, Printed by “Akademia”

C O N T E N T S

CONTENT-AWARE SEAM-CARVING RESIZING WITH U-NET SEGMENTATION: A PREPROCESSING FRAMEWORK THAT IMPROVES CNN-BASED BREAST-CANCER DETECTION IN MAMMOGRAMS

[1]Anxhelo SHEHU and [2]Enes STASTOLI

[1,2]AI Laboratory, Faculty of Computer Sciences and IT, Metropolitan University of Tirana, Albania

Author for correspondence: anxheloshehu@umt.edu.al

ASh, 0009-0006-0092-4424; ES, 0009-0006-4807-5951

ABSTRACT

Mammography is widely used for the early detection of breast cancer. Although convolutional neural networks (CNNs) have achieved promising results in mammogram classification, preserving critical image features during down sampling for accurate segmentation of regions of interest (ROIs) remains an open challenge. In this study, we introduce a hybrid framework that integrates the Seam Carving Algorithm (SCA) for content-aware image resizing with U-Net-based segmentation as a preprocessing pipeline prior to CNN classification. The proposed approach first reduces the dimensions of mammographic images while preserving high-information structures and subsequently applies a U-Net model to segment breast tissue and lesions. These segmented outputs are then fed into downstream CNN-based classifiers. We evaluated the performance of three deep learning architectures—DenseNet121, ResNet50, and VGG16—on both film-based and digital mammography datasets under two distinct preprocessing strategies: i) Seam Carving followed by Bicubic Interpolation (BSCBI): High-resolution images (exceeding 2500 x 2000 pixels) were first downsized to 750 x 500 pixels using SCA and then resized to 256 x 256 pixels via bicubic interpolation and, ii) Single Bicubic Interpolation (BI): Images were directly resized from their native high resolution to 256 x 256 pixels using bicubic interpolation alone. The results demonstrate that the BSCBI preprocessing strategy consistently outperforms the standard BI approach across all evaluated models and imaging modalities, yielding classification accuracy and sensitivity scores above 98%, compared to approximately 92% for BI. Ultimately, combining Seam Carving-based downsizing with U-Net segmentation markedly improves the detection of malignant cases across all benchmark CNN models. This hybrid framework shows strong potential for advancing computer-aided and fully automated breast cancer screening systems.

***Keywords*:** breast cancer, mammography, CNN, image downsizing, seam carving algorithm, U-Net, bicubic interpolation

Publisher: Academy of Sciences of Albania

Citation: Shehu A, Stastoli E. 2026. Content-aware seam-carving resizing with U-NET segmentation: A preprocessing framework that improves CNN-based breast-cancer detection in mammograms. *Albanian Journal of Natural and Technical Sciences (AJNTS),* **31 (3):** 7-30.
https://doi.org/10.67537/ajnts3103026
Classification: Research
Subject Category: applied sciences+technology subject area: biomedical engineering & artificial intelligence

1. INTRODUCTION

Advancements in medical imaging technologies, paired with well-established population screening programs, have positioned mammography as the cornerstone of early breast cancer screening (Champaign & Cederbom 2000). While these developments have significantly enhanced diagnostic capabilities, keeping high diagnostic accuracy across diverse patient populations remains a formidable challenge. Furthermore, radiological interpretation is inherently subject to inter-observer variability, which can result in ambiguous findings, false negatives, or false positives. Such diagnostic errors not only escalate healthcare costs due to unnecessary downstream diagnostic procedures but also inflict substantial psychological distress on patients. To contextualize the scale of this public health issue, Table 1 outlines the global burden of the most prevalent cancer types based on the 2022 WHO/IARC statistics.

Table 1. Worldwide Cancer Statistics in 2022: Number of new cases and deaths by cancer type

Cancer type	No. of new cases	No. of deaths
Lung cancer	2,480,301	1,817,172
Colorectal cancer	1,926,118	903,859
Breast cancer	**2,308,897**	**665,684**
Liver cancer	865,269	757,948
Prostate cancer	1,466,680	396,792
Stomach cancer	968,350	659,853

Consequently, there is a growing demand for more reliable, intelligent image analysis approaches capable of supporting clinicians in making accurate, reproducible diagnostic decisions. In recent years, artificial intelligence (AI) methodologies, particularly machine learning and deep learning, have emerged as highly promising tools for computer-aided diagnosis (CAD) and fully automated breast cancer detection. When deployed in medical image classification tasks, these networks show robust performance. Nevertheless, critical limitations persist. Mammograms are characterized by complex tissue structures, dense backgrounds, heterogeneous lesion shapes, and low contrast gradients. Furthermore, downsampling high-resolution mammographic images to meet the rigid input size constraints of standard convolutional neural networks (CNNs) often leads to the deletion of subtle, micro-scale features (such as microcalcifications or architectural distortions) that are diagnostically vital.

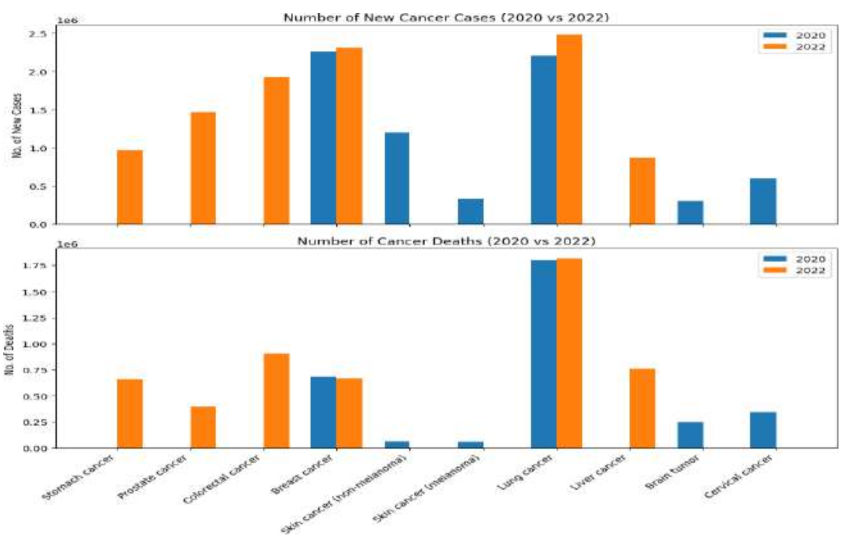

Fig. 1: Comparison of worldwide cancer statistics (2020 and 2022): New cases and deaths. Data source: GLOBOCAN (Bray *et al.* 2024).

A critical challenge in computerized mammography is the preservation of diagnostically meaningful features during resolution adaptation for deep learning architectures. To address this limitation, we propose a hybrid framework that integrates the Seam Carving Algorithm

(SCA) for content-aware image resizing (Avidan & Shamir, 2007) with U-Net-based segmentation (Ronneberger *et al*. 2015). The primary objective of this framework is to downsize high-resolution mammograms while preserving structurally vital regions, thereby focusing the downstream network on relevant anatomical areas prior to classification. By combining intelligent resizing with targeted segmentation, we aim to enhance the quality and integrity of the feature maps delivered to deep learning classifiers.

This study is guided by a central research question: *Does content-aware resizing via seam carving, applied prior to U-Net segmentation, preserve diagnostically relevant high-intensity structures (such as masses and microcalcifications) better than conventional bicubic interpolation, and does this preservation translate into measurably superior CNN classification performance?* We hypothesize that because masses and calcifications manifest as high-energy, high-intensity pixel regions, the seam carving algorithm, which iteratively removes only low-energy paths, will retain these critical structures and their morphological properties during aggressive downsizing. Conversely, uniform interpolation methods tend to blur or degrade these localized features. Consequently, a Seam Carving followed by Bicubic Interpolation (BSCBI) pipeline should yield higher, more stable classification metrics than Bicubic Interpolation (BI) or seam carving alone. This exact gap—the absence of a content-aware, shape-preserving resizing layer within existing segmentation-before-classification pipelines—has not, to our knowledge, been addressed in prior literature.

To evaluate the robustness and generalization capabilities of the proposed framework, experiments were conducted on two distinct datasets:

- **The MIAS Database** (Suckling *et al*. 2015): Consists of digitized film-based mammograms characterized by historical film artifacts and lower contrast gradients.
- **The CMMD Database** (Cai *et al*. 2023): Contains modern Full-Field Digital Mammography (FFDM) images characterized by high dynamic range and crisp spatial resolution.

Evaluating performance across both film-screen and digital imaging modalities allows us to validate the adaptability and clinical viability of the proposed framework under highly diverse image acquisition conditions.

Table 2. Mammographic databases and number of cases in benign and malignant classes

Database	Type	Benign	Malignant	Total Cases
MIAS	Film	64	51	115
CMMD1	Digital	473	553	1026

From CMMD, we selected the sub-dataset CMMD1, which contains 1026 cases (2 images for each) with biopsy-confirmed benign or malignant tumors. Through this work, we aim to contribute to the development of more accurate and reliable computer-assisted systems for breast cancer detection, ultimately supporting radiologists in clinical decision-making and improving patient care.

2. RELATED WORK

The U-Net architecture (Ronneberger *et al.* 2015) has become a benchmark paradigm in medical image segmentation, particularly for delineating malignant structures in deep learning-based breast cancer detection frameworks. Since its inception, numerous architectural variants have been proposed to adapt the network to diverse clinical applications (Soulami *et al*. 2021). Within computer-aided diagnosis (CAD) pipelines, U-Net segmentation is frequently deployed as a specialized preprocessing layer to generate localized regions of interest (ROIs) for downstream deep convolutional neural network (D-CNN) classifiers. Multiple studies (Asiri *et al.* 2023; Reddy & Sujatha 2024) document the efficacy of training U-Net on manually annotated datasets to output accurate pixel-level semantic masks.

While alternative architectures like Mask R-CNN (He *et al*. 2017) integrate object detection with instance segmentation, U-Net stays highly favoured for biomedical pixel-level classification tasks due to its data efficiency with limited medical samples (Tatli & Budak 2023; Ramalakshmi *et al*. 2025). Nevertheless, precision limitations persist when segmenting images characterized by highly heterogeneous tissue structures and varying fibro-glandular tissue densities.

Based on current literature (Khaled *et al*. 2022; Ramalakshmi *et al*. 2025), three primary challenges limit standard U-Net image processing performance in mammographic breast cancer diagnosis:

- **Handling Multifocal Lesions:** Standard U-Net implementations often struggle to segment multifocal lesions accurately, often not isolating multiple, spatially disjoint malignant regions simultaneously.
- **Loss of Fine-Scale Details:** Conventional geometric downsampling needed to satisfy rigid CNN input constraints causes severe spatial degradation, stripping away micro-scale features from high-resolution mammograms.
- **Lack of Content-Aware Rescaling:** Standard interpolation techniques (e.g., bilinear or bicubic) resize images globally without considering semantic feature maps, thereby degrading or erasing localized, high-frequency diagnostic info.

To resolve these limitations, our framework introduces the Seam Carving Algorithm (SCA) to downsize mammographic inputs prior to segmentation. Unlike traditional spatial reduction methods, SCA operates in a content-aware manner by computing a global energy map of the image and iteratively identifying paths of minimum energy—representing the least informative pixel trajectories across the image matrix.

Conceptually, if an image has a uniform background interspersed with localized high-frequency features, the minimum-energy seams will selectively route through the low-gradient background fields, avoiding structural boundaries.

In mammography, clinically significant ROIs (such as masses and microcalcifications) consistently exhibit higher pixel intensities and sharper gradient vectors relative to the surrounding adipose or fibro-glandular tissue. Because seam carving selectively targets and deletes low-energy, low-gradient paths, these vital high-intensity structures are preserved without morphological distortion—a structural property we exploit to prevent the information loss inherent to uniform geometric interpolation (illustrated qualitatively in Figures 5 and 7).

By marrying content-aware resizing with targeted U-Net segmentation, our proposed pipeline ensures that the feature maps presented to state-of-the-art D-CNN classifiers (Abdelhafiz *et al.* 2019) preserve the exact structural properties essential for highly accurate breast cancer detection.

3. METHODOLOGY

Our proposed framework comprises three primary stages: image preprocessing, U-Net segmentation, and CNN-based classification (see Figure 2).

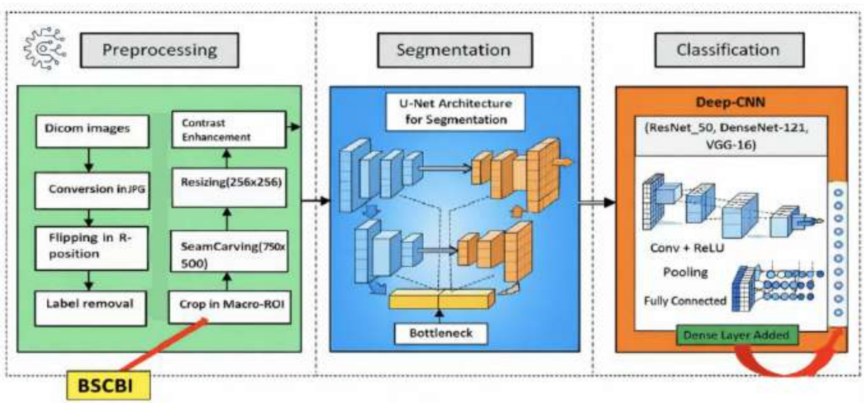

Fig. 2: The complete processing line. Balanced Seam Carving with Bicubic Interpolation (BSCBI), corresponds to the yellow block (Crop in Macro → ROI Seam Carving Resizing → Bicubic Interpolation Resizing).

3.1 Preprocessing

As highlighted by *Shorten and Khoshgoftaar* (2019), preprocessing is a foundational stage in computer vision and object detection pipelines, as the downstream accuracy of deep learning architectures heavily depends on the quality of the input data. In designing a preprocessing pipeline for convolutional neural networks (CNNs), several domain-specific factors must be considered, beginning with the standardized ingestion format of the imaging data. In this work, mammograms from both digital and digitized film-screen sources were standardized by converting the raw files into the JPEG format. Following formatting, a pixel-intensity thresholding operation was implemented to isolate the breast parenchyma and eliminate the non-informative, high-attenuation black background. While the Seam Carving Algorithm (SCA) is technically capable of removing these uniform background regions, direct intensity thresholding was selected for this initial phase as it provides a computationally efficient and deterministic alternative.

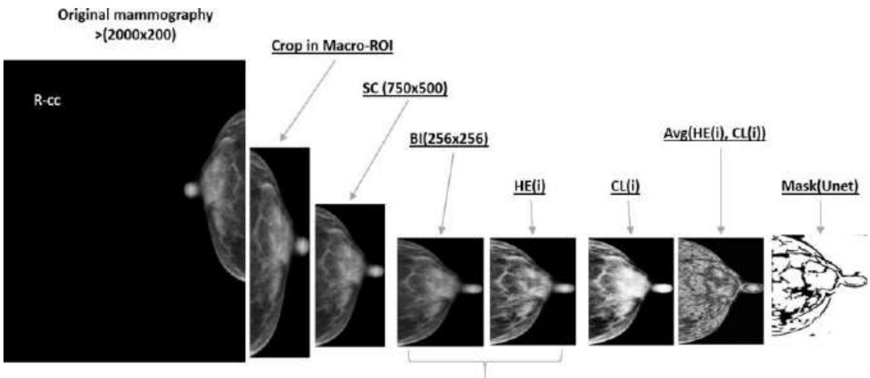

Fig. 3: BSCBI processing: from an original mammogram to the segmented image given as input to CNN.

3.1.2 Contrast Enhancement:

To enhance the contrast of the mammograms, a hybrid spatial-filtering approach combining global Histogram Equalization (HE) and local Contrast Limited Adaptive Histogram Equalization (CLAHE) was applied:

$$I_{Final} = \propto \times I_{HE} + (1 - \propto) \times I_{CL} \qquad (1)$$

Where:

- I_{Final} ⟶ is the final contrast enhanced image,
- I_{HE} ⟶ is the histogram-equalized image,
- I_{CL} ⟶ is the CLAHE (Contrast Limited Adaptive Histogram Equalization) processed image; $\propto \in [0,1]$ is the blending weight (0.25).

This image processing strategy significantly increases the contrast within the target regions of interest (ROIs). This specific modification is performed to establish a highly distinguishable separation between tissue structures and to improve the detection of micro-scale anomalies in multifocal cancer presentations.

Through this method of contrast optimization, we align the pixel statistical distributions of our dataset images with those expected by the pre-trained U-Net model. Additionally, this contrast enhancement method provides a clear boundary delineation for each region, even when the localized pixel intensity of an anomaly is highly similar to that of the surrounding tissue matrix. This optimization markedly increases the probability of detecting obscured lesions within dense breast tissue categories (BI-RADS Breast Density Categories C and D).

3.2 Segmentation

Once the image was re-dimensioned, semantic U-Net segmentation was applied. Specifically, we leveraged a U-Net model pre-trained on biomedical microscopy datasets and applied it directly to the processed mammograms via zero-shot transfer learning (without structural retraining or fine-tuning on breast imaging data). This network architecture computes a pixel-level clustering of tissue types and suspicious masses by mapping structural gradients in a manner analogous to the delineation of cell membranes in the ISBI Cell Tracking Challenge (2014) dataset upon which the model was originally optimized. An empirical analysis of our dataset immediately following the preprocessing phase demonstrates that contrast-enhanced mammograms exhibit a strong morphological and structural similarity to the cell membrane configurations found in the ISBI microscopy imagery (as illustrated qualitatively in Figure 4).

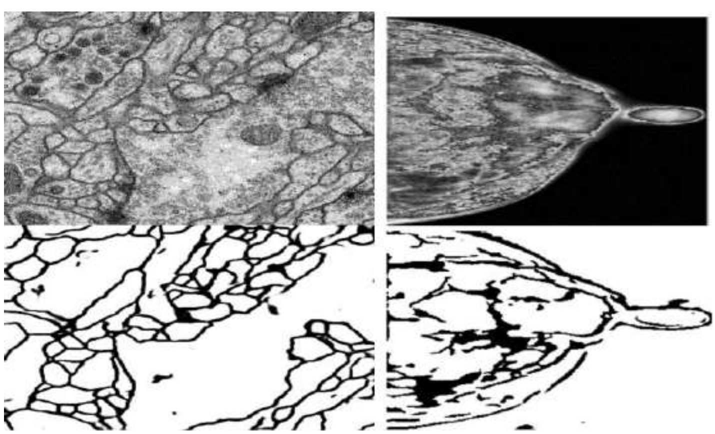

Fig. 4: U-Net trained on biomedical images is applied to segment Mammographic images: left-cell image, right-mammographic image (cell images from the ISBI Cell Tracking Challenge 2014; U-Net architecture: Ronneberger *et al*. 2015).

The architectural framework of the U-Net model enables highly efficient detection of complex lesion geometries by tracing high-frequency contour boundaries within the contrast-enhanced inputs. This capability stays exceptionally stable even when processing dense breast parenchyma (BI-RADS Categories C and D), which traditionally presents the greatest structural challenge and the highest rate of false negatives in computer-aided screening pipelines.

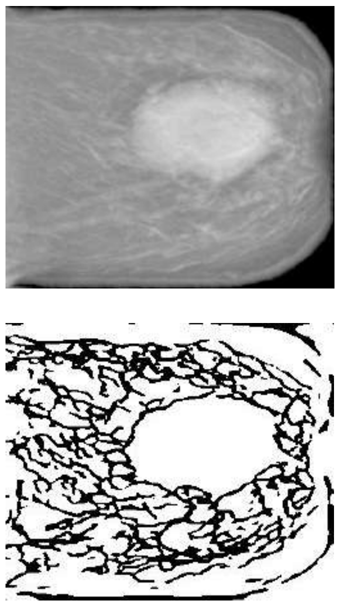

Fig. 5: Segmentation of a mammographic image that was significantly downsized. Left: downsized from 4K to 256x256 by SCA. Right: mask after segmentation.

Similarly, the pixel-level segmentation of each candidate area demonstrates distinct feature boundaries relative to adjacent regions. This sharp delineation proves highly advantageous for identifying multifocal cancer presentations, which, as noted in literature, often serves as a primary point of failure in conventional architectures (see Section 2, Related Work). This approach ensures that the framework consistently captures distinct, spatially disjoint ROIs. Delivering these isolated, high-contrast segmented maps to the downstream CNN architecture enables the network to classify them highly effectively based on their unique morphological and geometric profiles.

3.3 Classification with CNN

Following semantic segmentation, the output masks were normalized to scale pixel values strictly between 0 and 1. To evaluate the stability and robustness of the framework in binary classification (benign vs. malignant), we integrated three benchmark convolutional neural network (CNN) architectures: DenseNet121 (Huang *et al*. 2017), ResNet50 (He et al. 2016), and VGG16 (Simonyan & Zisserman 2014). These models represent classic paradigms in deep learning computer vision literature since the inception of AlexNet (Krizhevsky *et al*. 2017). Pairing localized U-Net segmentation with these deep CNN classifiers consistently improves diagnostic accuracy while minimizing the total computational overhead. This efficiency is achieved because the input feature maps fed into the CNNs are spatially optimized ROIs containing targeted morphological geometries of suspicious tissues, rather than uncompressed, full-field mammographic frames.

To ensure uniform dimensionality and manage computational costs, each architecture was appended with a single fully connected hidden layer consisting of 1,000 neurons prior to the final classification layer, maintaining a streamlined profile optimized for feature extraction.

As established by Lehman *et al*. (2015), models trained directly on native digital datasets exhibit superior diagnostic accuracy and reliability in identifying breast cancer compared to those optimized on digitized film-screen data. Consequently, the CNN classifiers in this framework were trained exclusively on the digital CMMD1 dataset, while their cross-domain generalization capabilities were subsequently evaluated on both the digital and the film-based MIAS datasets. To prevent data leakage, partitions were strictly enforced at the patient level; patients were never shared between the training, validation, and testing splits, ensuring that the cross-domain evaluation on the film-based MIAS dataset remained completely held-out.

To clarify the operational parameters of the segmentation layer: the U-Net model was pre-trained solely on the ISBI cell-membrane microscopy dataset (Cell Tracking Challenge 2014) and was not fine-tuned or retrained on mammograms. It operates on the contrast-enhanced mammograms via direct, zero-shot transfer learning, a step justified by the structural and gradient similarities achieved after our hybrid contrast-stretching pipeline (as shown in Figure 4). Conversely, the downstream CNN classifiers (DenseNet121, ResNet50, and VGG16) were fully trained in this study utilizing an NVIDIA Quadro P6000 GPU. The high-performance threshold (97%) referenced during validation represents the U-Net architecture's baseline segmentation performance on its native microscopy source task, not an architecture optimized on mammography training targets.

4. RESULTS

The classification metrics reported herein represent the average values obtained via a 5-fold cross-validation protocol, expressed as the mean across all five validation folds. Within the MIAS dataset, the minority class (benign) was balanced against the majority class using random oversampling to mitigate class-imbalance bias. For the CMMD1 dataset, the class distributions were inherently balanced, negating the need for data augmentation or oversampling. The baseline U-Net model achieved a segmentation accuracy exceeding 97\% on its native ISBI microscopy source task within 5 training epochs (1,500 steps/epoch), using a batch size of 2 across a dataset configuration of 24 training and 6 validation images. The downstream CNN models were trained for 25 epochs utilizing an early stopping regularization mechanism that monitored validation loss at 5-epoch intervals. This exact 5-fold cross-validation scheme was strictly maintained across all architectural configurations to ensure parity.

4.1 Ablation: Performance of BSCBI vs BI and SC

To isolate the explicit structural advantages of our proposed framework, controlled ablation experiments were conducted to compare Balanced Seam Carving with Bicubic Interpolation (BSCBI) against both standalone Bicubic Interpolation (BI) and standalone Seam Carving (SC). Because these three distinct configurations vary solely in their image preprocessing component while keeping the U-Net segmentation layer, the CNN classifier topologies, and the training hyperparameters entirely fixed, this comparison isolates the specific contribution of each resizing method. The underlying CNN backbone was held uniform across all three configurations to ensure strict experimental control.

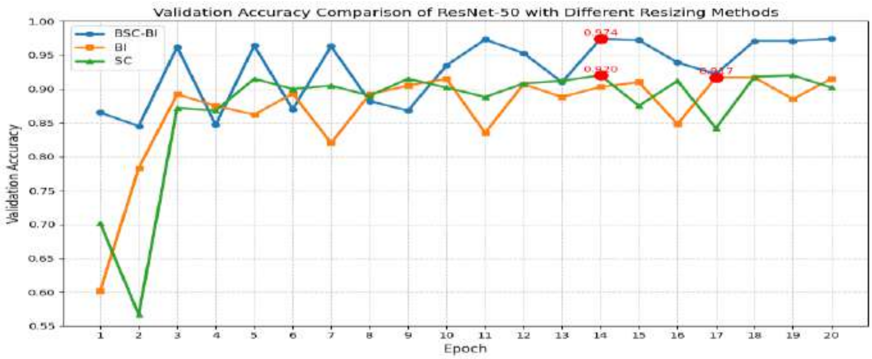

Fig.6: Accuracy of ResNet50 model in test set. Blue: BSCBI, orange: BI, green: SC.

As illustrated in Figure 6, the model integrated with the BSCBI preprocessing framework achieved superior classification performance compared to alternative setups. Notably, this configuration converged rapidly, exceeding a validation accuracy of 96% by the 3rd training epoch. Conversely, the ResNet50 models utilizing either standalone BI or standalone SC exhibited significantly lower performance curves. This degradation is attributed to sub-optimal upstream U-Net segmentation, as uniform geometric interpolation and unmitigated seam carving alone fail to adequately preserve the structural and morphological integrity of the target lesions during aggressive downsampling.

4.1.1 Resizing with Seam Carving:

To accommodate variations in anatomical breast dimensions while matching the static field-of-view constraints of the network architecture, the Seam Carving Algorithm (SCA) was deployed to systematically downsize the high-resolution mammograms to an intermediate footprint of 750 x 500 pixels.

Empirical testing indicated that downsizing aggressively beyond this threshold introduced severe spatial degradation, resulting in the structural loss of micro-scale features such as microcalcifications and detailed lesion geometries. Unlike standard geometric scaling operators that compute pixel values uniformly within localized spatial neighborhoods, SCA operates globally by calculating dynamic programming paths across minimum-energy pixel trajectories. Consequently, the relative surface area occupied by a given region of interest (ROI) becomes significantly higher in the downsized matrix than in the native 4K full-format mammogram, maximizing the spatial salience of localized anomalies. To systematically evaluate the mathematical impact of this content-aware resolution reduction on the diagnostic accuracy of the downstream convolutional neural network, a series of controlled downsizing scenarios were tested using combinations of Seam Carving (SC) and Bicubic Interpolation (BI). All input variations were targeted toward a uniform final classification resolution:

- (a) No SC, 2500 x 2000 resized to 128x128,
- (b) SC downsized to 1000 x 1000 then resized to 128x128 with BI,
- (c) SC downsized to 700 x 700 then resized to 128x128 with BI,
- (d) SC downsized to 500 x 500 then resized to 128x128 with BI,
- (e) SC downsized to 256 x 256 then resized to 128x128 with BI,
- (f) SC downsized to 128 x 128 no resizing with BI,
- (g) SC downsized to 64 x 64 no resizing with BI,
- (h) SC downsized to 32 x 32 no resizing with BI.

For training, the same VGG16 architecture was used, and we calculated the average accuracy for each case (Figure 7).

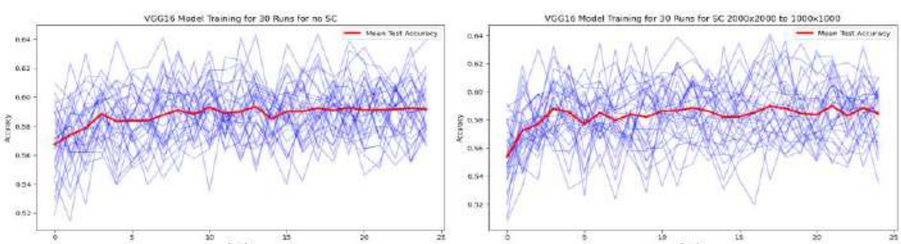

(a) (b)

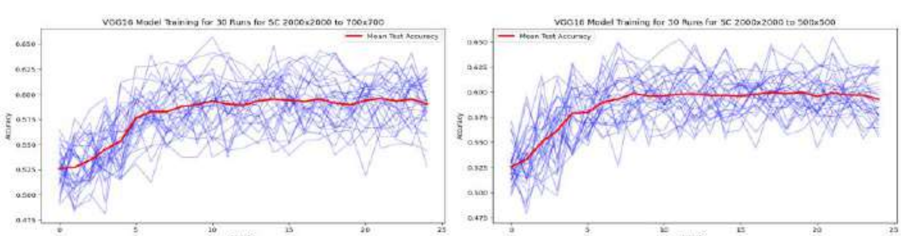

(c) (d)

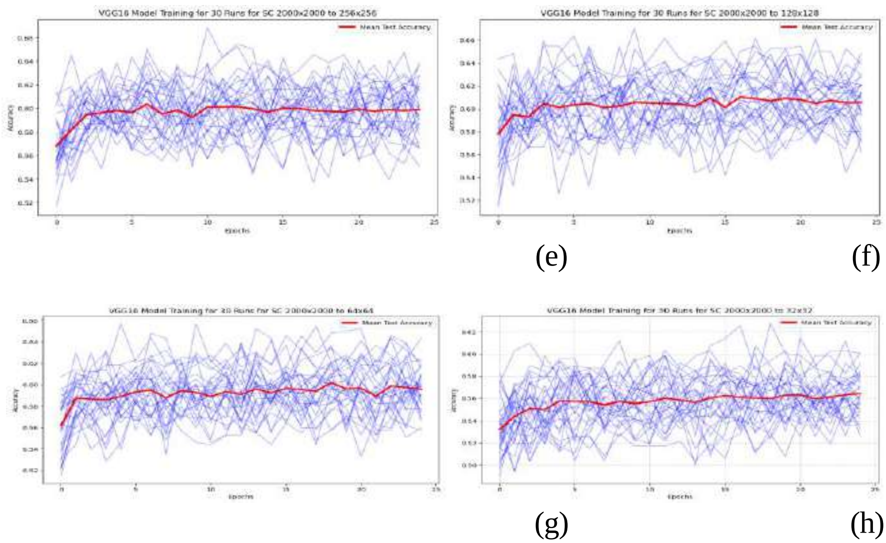

Fig. 7: Mean accuracy (red line) for different types of resizing for 30 runs each (performance during training on test set [blue lines]).

Based on the empirical data collected across scenarios (a) through (h), the classification architecture exhibits optimal performance when content-aware Seam Carving (SC) is paired with subsequent Bicubic Interpolation (BI) at intermediate target bounds of either 700x700 → 128x128 or 500x500 → 128x128. Specifically, shifting the preprocessing paradigm from standalone geometric interpolation (scenario a) to the hybrid pipelines of scenarios (c) and (d) drives a mean accuracy increase from 0.587 to approximately 0.600, while simultaneously reducing the standard deviation from 0.021 to 0.017. A corresponding performance trajectory is observed when transitioning from hyper-aggressive standalone seam carving (scenario h) to the balanced 500 x 500 intermediate footprint of scenario (d); here, the average classification accuracy rises from 0.560 to 0.600, accompanied by a drop in standard deviation from 0.022 to 0.017. To establish rigorous statistical significance, the network was trained independently 30 times across 25 epochs for each distinct scenario. Crucially, the primary U-Net segmentation and advanced filtering blocks described in previous sections were purposefully omitted during these specific trials. This constraint isolates the mathematical influence of the dimensional reduction layers, enabling a controlled evaluation of standalone SC, standalone BI, and their hybrid combinations.

4.2 Best classifier in classification tasks

Having established the empirical efficiency of the Balanced Seam Carving with Bicubic Interpolation (BSCBI) configuration as the baseline preprocessing engine, the complete hybrid framework was evaluated on the binary classification task. Within the downstream classifier block, we benchmarked the three state-of-the-art CNN architectures detailed in the literature review. This phase evaluates the explicit macro-level performance enhancements provided by the BSCBI framework by directly contrasting the classification metrics against baseline models operating entirely without content-aware resizing.

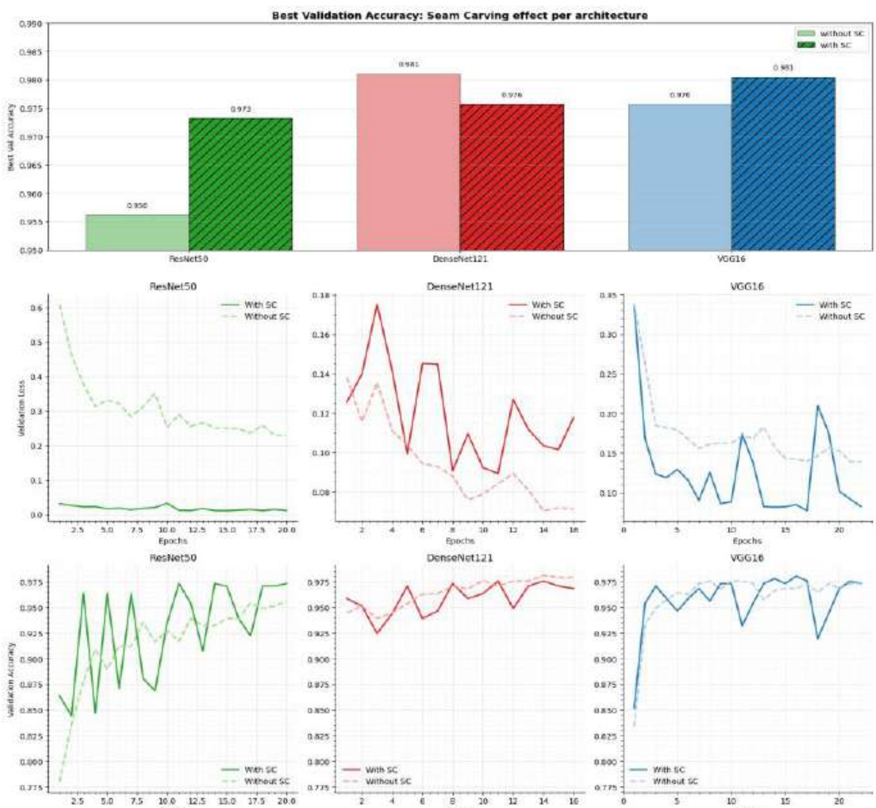

Fig. 8: Performances of ResNet-50, DenseNet-121, and VGG-16 in CMMD1 dataset with and without Seam Carving image downsizing. First row: Best performance for each model with & without the use of Seam Carving. Second and third row: Performance report on validation data.

The VGG16 model achieved the highest peak validation classification accuracy (>0.98) by the 16th training epoch. Performance metrics were remarkably consistent across both the benign and malignant classes, with individual scores tightly constrained between 0.97 and 0.99. This lack of variance indicates that the VGG16 backbone, when integrated into our hybrid framework, is exceptionally well-suited for high-fidelity binary classification. It maintains a highly balanced predictive capability across distinct metric groups, ensuring clinical reliability for both benign and malignant diagnoses. These findings corroborate the robust performance characteristics of the architecture noted by BreastNet18 (Montaha *et al*. 2021) and extend its empirical validity to this specific hybrid downsampling pipeline.

Because the reference baseline studies utilized for performance comparison traditionally report only peak empirical values, we have presented our average metrics without confidence intervals to ensure strict structural comparability across the literature. Furthermore, because the performance vectors obtained through our proposed BSCBI-U-Net framework consistently approach the theoretical maximum performance thresholds (near-saturation accuracy), calculating confidence intervals yields negligible statistical or analytical value for this specific comparative study.

Table 3: Classification performance in test data of state-of-the-art CNN Models with BSCBI resizing.

Model	**Class**	**Precision**		**Recall**	**F1-Score**	**Accuracy**
ResNet50	Benign	0.98		0.97	0.98	0.98
	Malignant	0.97		0.98	0.98	
DenseNet121	Benign	0.98		0.97	0.98	0.98
	Malignant	0.97		0.98	0.98	
VGG-16	Benign	0.97		0.99	0.98	0.98
	Malignant	0.99		0.97	0.98	

The DenseNet121 model also emerged as a high-performing architecture, reaching a validation classification accuracy exceeding 0.97 by the 11th training epoch. The corresponding precision, recall, and F1-score vectors closely mirrored those of the VGG16 network, with all values converging at approximately 0.98. This architecture demonstrates strong competitiveness with VGG16 regarding overall classification efficacy, particularly during the initial training phases, which indicates highly efficient feature learning and rapid convergence properties.

The ResNet50 backbone exhibited performance trajectories closely aligned with those of DenseNet121, similarly achieving a validation accuracy greater than 0.97 at the 11th epoch. Its core evaluation metrics (precision, recall, and F1-score) remained stable, consistently averaging 0.98. This high degree of consistency across both the benign and malignant classes underscores the robustness of the model. While its peak validation accuracy was marginally lower than the thresholds established by DenseNet121 and VGG16, ResNet50 maintains excellent generalization capabilities within the proposed preprocessing framework.

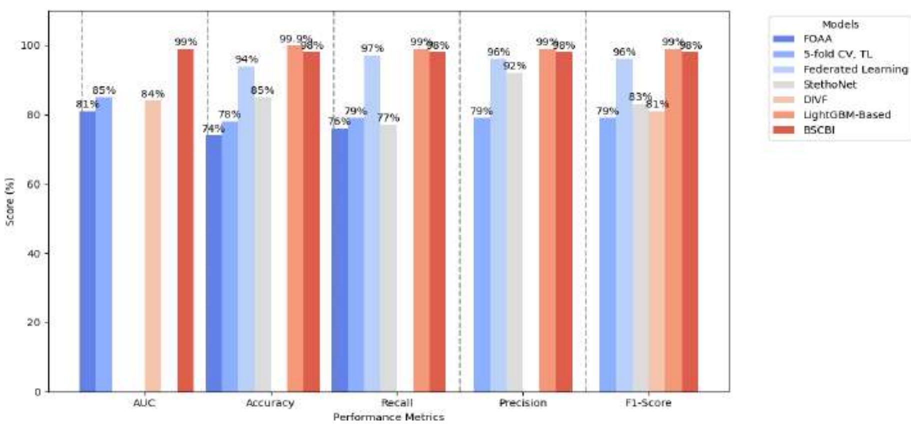

Fig. 9: Breast Cancer diagnosis performances: Area Under the ROC curve (AUC), Accuracy (ACC), Recall, Precision (Prec), and F1-score. Performance results from FOAA (Bobowicz *et al*. 2023), 5-fold CV, TL (Alwazzan *et al*. 2024), Federated Learning (AlSalman *et al*. 2024), StethoNet (Lamprou *et al*. 2024), DIVF Average (Nguyen *et al*. 2023), LightGBM-Based (Sait & Nagaraj 2024), and BSCBI (our method).

In summary, evaluating the BSCBI preprocessing framework across the three deep convolutional architectures demonstrated exceptionally high-performance metrics, even when generalizing to legacy film-screen mammograms where both sensitivity and specificity converged at approximately 99%. The VGG16 and DenseNet121 architectures delivered the highest and most balanced predictive performance across all validation domains. Conversely, while the performance metrics of the ResNet50 model were marginally lower, they exhibited superior stability across training epochs, indicating that the ResNet50 backbone provides enhanced structural robustness compared to the other two architectures. Furthermore, although the performance metrics presented in this study represent rigorous average values derived via a 5-fold cross-validation protocol, they were benchmarked against historical baselines extracted from the literature evaluating the CMMD1 dataset (where results are occasionally reported solely as peak performance vectors rather than cross-validated averages). Because these external studies do not utilize uniform dataset splits, validation folds, or identical evaluation metrics, these cross-study comparisons are presented exclusively as indicative context rather than a direct, like-for-like baseline evaluation.

5. CONCLUSIONS

In this study, we evaluated an array of preprocessing configurations for resizing medical mammographic images, establishing Balanced Seam Carving with Bicubic Interpolation (BSCBI) as highly effective approach. Leveraging this structural advantage, we introduced a hybrid approach for breast cancer detection in mammography that integrates BSCBI for image resizing with U-Net segmentation and downstream deep CNN classification. This architectural coupling markedly enhances the performance of classification networks by preserving localized, highly informative regions of interest (ROIs). When evaluated on the digital CMMD1 dataset, the proposed framework achieved a classification accuracy and F1-score of ≈ 0.98 and sensitivity/specificity ≈ 0.99 across ResNet-50, DenseNet-121 and VGG-16 on CMMD1 for the proposed pipeline, as compared to the bicubic interpolation alone (accuracy ≈ 0.92).

These empirical milestones underscore the clinical necessity of maintaining the morphological integrity of primary ROIs, particularly when aggressive downsampling is required to process microcalcifications and micro-scale malignant structures. Compared to the decoupled execution of either Seam Carving or Bicubic Interpolation, the hybrid BSCBI framework proved to be the most proficient method for binary classification (benign vs. malignant). Mechanistically, this performance dividend stems from the selective deletion of low-energy, low-gradient pixel seams. High-intensity pixel configurations encoding masses and microcalcifications safely survive the dimensional reduction stage. Consequently, the U-Net layer receives sharply delineated boundaries, and the downstream CNN is fed shape-faithful structural inputs. Conversely, uniform geometric interpolation (BI) inherently flattens these high-frequency spatial cues, leading to localized feature degradation and poorer downstream classification. Furthermore, our dual-domain contrast-stretching strategy effectively accentuates tissue boundaries, significantly optimization the U-Net's segmentation fidelity.

The performance gains enabled by the BSCBI engine remained highly consistent across all evaluated CNN configurations (ResNet50, DenseNet121, and VGG16). Crucially, this optimization was sustained even when transferring a U-Net model trained exclusively on non-mammographic biomedical microscopy images, demonstrating the exceptional cross-domain robustness and adaptability of the pipeline. Furthermore, the framework demonstrated reliable generalization across both native digital and legacy film-screen mammographic formats. The unified integration of content-aware resizing, semantic segmentation, and deep feature classification enables highly efficient feature representation, successfully navigating clinical edge cases—such as dense breast parenchyma (BI-RADS Categories C and D) and multifocal lesion distributions—that typically confound conventional deep learning networks.

The integration of preprocessing, segmentation, and classification stages allowed for a more efficient extraction and representation of relevant features, particularly in complex cases such as high-density breast tissues and multifocal cancer regions, which are often challenging for traditional approaches.

Despite the strong empirical validation of the proposed framework, several limitations must be acknowledged:

- **Domain Transfer Boundaries:** The integrated U-Net model was transferred directly from microscopy tasks without mammogram-specific fine-tuning or target weight optimization; thus, segmentation stability cannot be uniformly guaranteed across highly atypical or rare clinical tissue presentations.
- **Dataset Constraints:** While the film-screen validation on the MIAS dataset provides a completely held-out, cross-domain test, the sample size remains restricted (115 cases).
- **Single-Center Biases:** Both the CMMD1 and MIAS datasets are single-source cohorts; consequently, comprehensive multi-center

external validation is required in future work to fully confirm clinical generalizability.

- **Extreme Density Overlap:** While BSCBI provides distinct classification advantages and accelerated model convergence compared to uniform interpolation, persistent failure modes remain concentrated within extremely dense breast tissue matrices where the relative intensities of target ROIs and background fibro-glandular tissue overlap heavily.

Conflict of Interest. The authors declare no conflicts of interest.

Originality and Authorship. This work is based on the original data (public data) and ideas developed by the authors. No artificial intelligence tools were employed in the writing or preparation of this manuscript.

Author contributions. A.Sh.: concep the study, developed the methodology and software, designed and performed the experiments, analyzed the results, and wrote the manuscript. **E.S.:** contributed to this study through manuscript analysis and writing.

Declaration of AI use. We confirm that no AI-assisted technologies were used to create this article.

Ethics. This study used only publicly available, de-identified mammography databases (MIAS and CMMD), for which no additional ethical approval was required.

REFERENCES

Abdelhafiz D, Yang C, Ammar R, Nabavi S. 2019. Deep convolutional neural networks for mammography: Advances, challenges, and applications. *BMC Bioinformatics*, **20 (Suppl.11): 281.** https://doi.org/10.1186/s12859-019-2823-4.

AlSalman H, Al-Rakhami MS, Alfakih T, Hassan MM. 2024. Federated learning approach for breast cancer detection based on DCNN. *IEEE Access*, **12:**40114–40138. https://doi.org/10.1109/ACCESS.2024.3374650.

Alwazzan O, Patras I, Slabaugh G. 2024. FOAA: Flattened outer arithmetic attention for multimodal tumor classification. arXiv preprint arXiv:2403.06339. https://doi.org/10.48550/arXiv.2403.06339.

Asiri AA, Shaf A, Ali T, Aamir M, Irfan M, Alqahtani S, Mehdar KM, Halawani HT, Alghamdi AH, Alshamrani AFA, Alqhtani SM. 2023. Brain tumor detection and classification using fine-tuned CNN with ResNet50 and U-Net model: A study on TCGA-LGG and TCIA dataset for MRI applications. *Life (Basel)* **13(7):**1449. https://doi.org/10.3390/life13071449.

Avidan S, Shamir A. 2007. Seam carving for content-aware image resizing. *ACM Transactions on Graphics*, **26(3):** 1-9. https://doi.org/10.1145/1276377.1276390.

Bobowicz M, Rygusik M, Buler J, Buler R, Ferlin M, Kwasigroch A, Szurowska E, Grochowski M. 2023. Attention-based deep learning system for classification of breast lesions-Multimodal, weakly supervised approach. *Cancers* **15(10):**2704. https://doi.org/10.3390/cancers15102704.

Bray F, Laversanne M, Sung H, Ferlay J, Siegel RL, Soerjomataram I, Jemal A. 2024. Global cancer statistics 2022: GLOBOCAN estimates of incidence and mortality worldwide for 36 cancers in 185 countries. *CA: Cancer Journal for Clinicians*, **74(3):**229-263. Epub 2024 Apr 4. PMID: 38572751. https://doi.org/10.3322/caac.21834.

Cai H, Wang J, Dan T, Li J, Fan Zh, Yi W, Cui Ch, Jiang X, Li L. 2023. An online mammography database with biopsy confirmed types. *Scientific Data*, **10(1):**123. https://doi.org/10.1038/s41597-023-02025-1.

Champaign JL, Cederbom GJ. 2000. Advances in breast cancer detection with screening mammography. *Ochsner Journal*, **2(1):**33–35. PMCID: PMC3117552 PMID: 21765659 https://pmc.ncbi.nlm.nih.gov/articles/PMC3117552/.

He K, Gkioxari G, Dollár P, Girshick R. 2017. Mask R-CNN. *In Proceedings of the IEEE International Conference on Computer Vision* (ICCV) (pp. 2961–2969). IEEE. https://doi.org/10.1109/ICCV.2017.322.

He K, Zhang X, Ren S, Sun J. 2016. Deep residual learning for image recognition. *In Proceedings of the IEEE Conference on Computer Vision and Pattern Recognition* (CVPR) (pp. 770–778). IEEE. https://doi.org/10.1109/CVPR.2016.90.

Huang G, Liu Z, van der Maaten L, Weinberger KQ. 2017. Densely connected convolutional networks. *In Proceedings of the IEEE*

Conference on Computer Vision and Pattern Recognition (CVPR) (pp. 4700–4708). IEEE. https://doi.org/10.1109/CVPR.2017.243.

Khaled R, Vidal J, Vilanova JC, Martí R. 2022. A U-Net ensemble for breast lesion segmentation in DCE MRI. *Computers in Biology and Medicine,* 140:105093. https://doi.org/10.1016/j.compbiomed.2021.105093.

Krizhevsky A, Sutskever I, Hinton GE. 2017. ImageNet classification with deep convolutional neural networks. *Communications of the ACM* **60(6)**:84–90. https://doi.org/10.1145/3065386

Lamprou C, Katsikari K, Rahmani N, Hadjileontiadis LJ, Seghier M, Alshehhi A. 2024. StethoNet: Robust breast cancer mammography classification framework. IEEE Access 12:144890–144904. https://doi.org/10.1109/ACCESS.2024.3473010 .

Lehman CD, Wellman RD, Buist DSM, Kerlikowske K, Tosteson ANA, Miglioretti DL, for the Breast Cancer Surveillance Consortium. 2015. Diagnostic accuracy of digital screening mammography with and without computer-aided detection. *JAMA Internal Medicine,* **175(11):**1828–1837. https://doi.org/10.1001/jamainternmed.2015.5231.

Montaha S, Azam S, Rafid AKMRH, Ghosh P, Hasan MZ, Jonkman M, De Boer F. 2021. BreastNet18: A high accuracy fine-tuned VGG16 model evaluated using ablation study for diagnosing breast cancer from enhanced mammography images. *Biology* **10(12)**:1347. https://doi.org/10.3390/biology10121347

Nguyen T-H, Kha QH, Truong ThNTT, Lam BT, Ngo BH, Dinh QV, Le NQK. 2023. Towards robust natural-looking mammography lesion synthesis on ipsilateral dual-views breast cancer analysis. In *Proceedings of the IEEE/CVF International Conference on Computer Vision Workshops* (ICCVW) (pp. 2564–2573). https://doi.org/10.48550/arXiv.2309.03506.

Ramalakshmi E, Gunisetti L, Lingamgunta S. 2025. Comparative analysis of different U-Net variants for breast cancer detection in histological images. International Journal of Computer Information Systems and Industrial Management Applications 17:350–361. https://doi.org/10.70917/ijcisim-2025-0023.

Reddy TS, Sujatha S. 2024. U-Net segmentation for CNN classification to improve the accuracy of automatic prediction of brain tumors using MRI images. *Journal of Electrical Systems* **20(2)**:2284–2295. https://doi.org/10.52783/jes.1995

Ronneberger O, Fischer P, Brox T. 2015. U-Net: Convolutional networks for biomedical image segmentation. *In Proceedings of the International Conference on Medical Image Computing and Computer-Assisted Intervention* (MICCAI) (pp. 234–241). Springer. https://doi.org/10.1007/978-3-319-24574-4_28.

Sait ARW, Nagaraj R. 2024. An enhanced LightGBM-based breast cancer detection technique using mammography images. Diagnostics 14(2):227. https://doi.org/10.3390/diagnostics14020227.

Shorten C, Khoshgoftaar TM. 2019. A survey on image data augmentation for deep learning. *Journal of Big Data*, **6(1):**60. https://doi.org/10.1186/s40537-019-0197-0.

Simonyan K, Zisserman A. 2014. Very deep convolutional networks for large-scale image recognition. arXiv preprint arXiv:1409.1556. https://doi.org/10.48550/arXiv.1409.1556.

Soulami A, Cherradi B, El Hassani A, Sayyouri N. 2021. Breast cancer: One-stage automated detection, segmentation, and classification of digital mammograms using U-Net model based semantic segmentation. *Biomedical Signal Processing and Control*, 66:102481. https://doi.org/10.1016/j.bspc.2021.102481.

Suckling, J., Parker, J., Dance, D., Astley, S., Hutt, I., Boggis, C., Ricketts, I., Stamatakis, E., Cerneaz, N., Kok, S., Taylor, P., Betal, D., & Savage, J. 2015. *Mammographic Image Analysis Society (MIAS) database v1.21*. Apollo - University of Cambridge Repository. https://doi.org/10.17863/CAM.105113

Tatli U, Budak C. 2023. Biomedical image segmentation with modified U-Net. Traitement du Signal 40(2):211–218. https://doi.org/10.18280/ts.400211.

EVALUATION OF URBAN VEGETATION COVER USING GOOGLE EARTH HIGH-RESOLUTION IMAGES: A CASE STUDY OF ELBASANI CITY

[1]Neki FRASHERI, [2]Hajri HASKA

[1]Academy of Sciences of Albania, [2]Metropolitan University, Tirana, Albania

Author for correspondence: nfrasheri@fti.edu.al

NF, 0000-0001-5928-275X; HH, 0000-0003-0361-1109

ABSTRACT

In the present investigation, high-resolution Google Earth imagery was analysed by exploiting exclusively the visible red-green-blue (RGB) color channels. The methodology was designed to be straightforward and reproducible, utilizing free and open-source software (FOSS), and relying on fundamental theoretical principles alongside an empirical evaluation of spectral differences between built-up areas (roads and buildings) and urban parks. The results regarding the urban vegetation cover of Elbasan are presented, providing a comprehensive overview of its spatial distribution across the city.

Keywords: urban vegetation cover, visible- spectrum imagery, Elbasani

Publisher: Academy of Sciences of Albania

Citation: Frasheri N, Haska H. 2026. On the evaluation of urban vegetation cover using google earth high-resolution images: A case study for Elbasani city. *Albanian Journal of Natural and Technical Sciences* (*AJNTS),* **31 (3):** 31-43.
https://doi.org/10.67537/ajnts3103027
Classification: Research
Subject Category: applied sciences subject area earth sciences +environmental sciences

1. INTRODUCTION

Traditional remote sensing evaluation of vegetation cover relies heavily on near- infrared (NIR) imagery. This reliance stems from the biophysical mechanisms of photosynthesis, in which chlorophyll pigments strongly absorb light in the visible blue and red wavelengths, whereas internal leaf structures reflect and transmit near-infrared radiation.

However, a significant constraint arises from spatial resolution of imagery provided by free online satellite repositories, such as those of NASA, USGS, and ESA. The spatial resolution of the open-access datasets, specifically those including NIR bands, typically ranges from 10 to 30m (e.g., Landsat and Sentinel-2). This medium-to-coarse spatial resolution introduces significant sub-pixel mixing in heterogeneous urban landscapes, where green spaces and non-vegetated artificial features smaller than the pixel size frequently coexist within individual pixels. To overcome this limitation, this study investigated the utility of visible red, green, and blue (RGB) channels extracted from high-resolution imagery available via the Google Earth platform, which offers a metric-scale spatial resolution.

2. METHODOLOGY

The traditional benchmark for assessing vegetation density in remote sensing is the Normalized Vegetation Index (NDVI), which is mathematically formulated as:

$$NDVI = (NIR - RED) / (NIR + RED)$$

where NIR and RED are the spectral reflectance values recorded in the near-infrared and red bands, respectively. Calculating NDVI requires multispectral datasets containing both bands, which are typically acquired from satellite constellations, such as MODIS, LANDSAT, and Sentinel-2. However, these open-access products generally offer low-to-medium spatial resolutions (ranging from 10m-30m), rendering them inadequate for highly detailed intra-urban canopy assessments. Conversely, free high-resolution imagery, such as that provided by the Google Earth platform, consists strictly of visible-spectrum red, green, and blue (RGB) channels, lacking the critical near-infrared band. To circumvent this limitation, several visible-spectrum vegetation indices (VVis) have been developed. These indices leverage the natural colour, missing the infrared. Several other vegetation indices are known, based only on visible colours that exploit the ability of plants to react differently with lights of different colours, mostly because plants absorb red and reflect green and partially blue lights. Lussem *et al.* (2018) compiled a comparative overview of seven prominent vegetation indices, as detailed in Table 1. Within this framework, RGBVI, GLI, VARI, and NGRDI operate exclusively within the visible spectrum, whereas NDVI and Simple Ratio (SR) indices require near-infrared bands.

Table 1: Mathematical Equations of Selected Vegetation Indices (VIs)

Vi Name	Mathematical Equation	References
RGBVI	(RG*RG – RR*RB) / (RG*RG + RR*RB)	Bendig *et al.* 2015
GLI	(2*RG – RR – RB) / (2*RG + RR + RB)	Louhaichi *et al.* 2001
VARI	(RG – RR) / (RG + RR – RB)	Gitelson *et al.* 2002
NGRDI	(RG – RR) / (RG + RR)	Tucker, 1979
NDVI	(RNIR – RR) / (RNIR + RR)	Rouse *et al.* 1974
NDVI 800 750	(R800 – R750) / (R800 + R750)	Gnyp *et al.* 2015
SR 810 750	R810 / R750	Gnyp *et al.* 2015

Note: R_R, R_G, and R_B denote the reflectance values of the red, green, and blue bands, respectively; R_{NIR} represents near-infrared reflectance, Rxyz signifies narrow-band reflectance at a specific wavelength (λ) in nanometres (ex. R800=800 nm) (Lussem *et al.* 2018).

In this study, the Red-Green-Blue Vegetation Index (RGBVI; Bendig *et al.* 2015) was used to evaluate the urban canopy of Elbasan. This index yields normalized values ranging from -1 to +1, mirroring the primary chlorophyll absorption and reflectance mechanisms of foliar tissue, where higher positive values represent healthy and dense green vegetation. Among the visible-spectrum indices detailed in the literature, RGBVI represents one of the most structurally refined formulations for isolating green biomass without near-infrared data.

High-resolution visible-spectrum RGB imagery covering the Elbasan study area was acquired from Google Earth. The underlying data source consisted of orthophotos captured by Airbus Defence and Space on July 30, 2024. To preserve the maximum spatial resolution during data extraction, the city's geographic extent was divided into a 5 x 5 grid consisting of 25 discrete sectors. Each sector was exported at the maximum digital resolution and subsequently mosaicked within a geographic information system (GIS) environment to construct a seamless orthomosaic of the entire urban area (Figure 1), with sector boundaries delineated by red vector lines. The RGBVI script was executed on the open-source platform, QGIS to generate a continuous grayscale raster output. The raw RGBVI raster underwent linear contrast stretching optimize visual interpretation and maximize the contrast between urban features. The native pixel values were mapped into an 8-bit unsigned range [0,255] (Fig. 2) using the automated histogram equalization function (colours: auto: equalize) within the image processing software function of image processing software GIMP. The pre- and post-equalization radiometric distributions, along with the corresponding transformation mapping functions, are illustrated via histograms in Fig. 3.

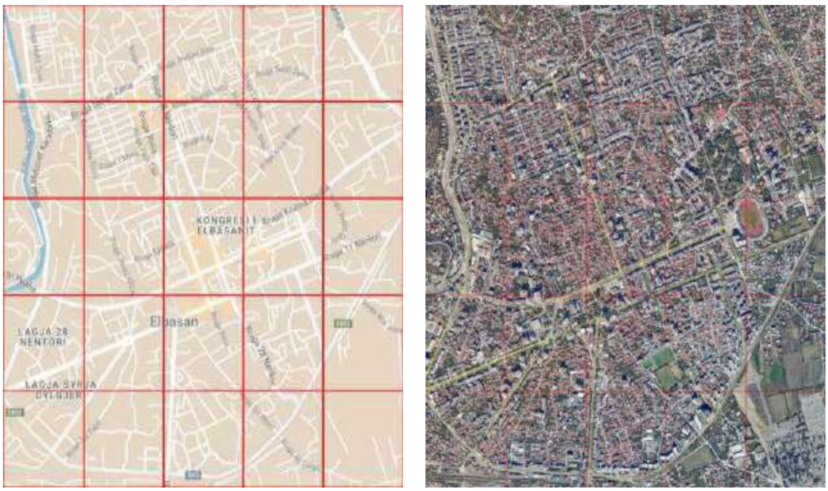

Fig.1. Map view of Elbasan and its RGB image divided into sections (Google Mymaps).

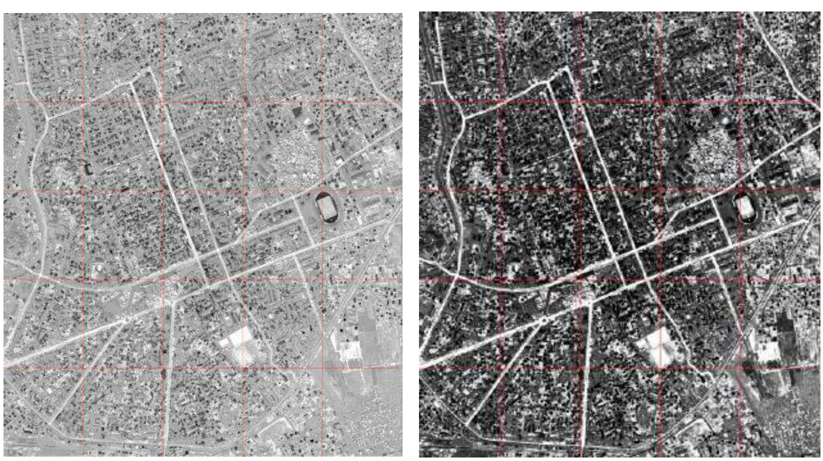

Fig. 2. RGBVI image of Elbasan and its enhanced version.

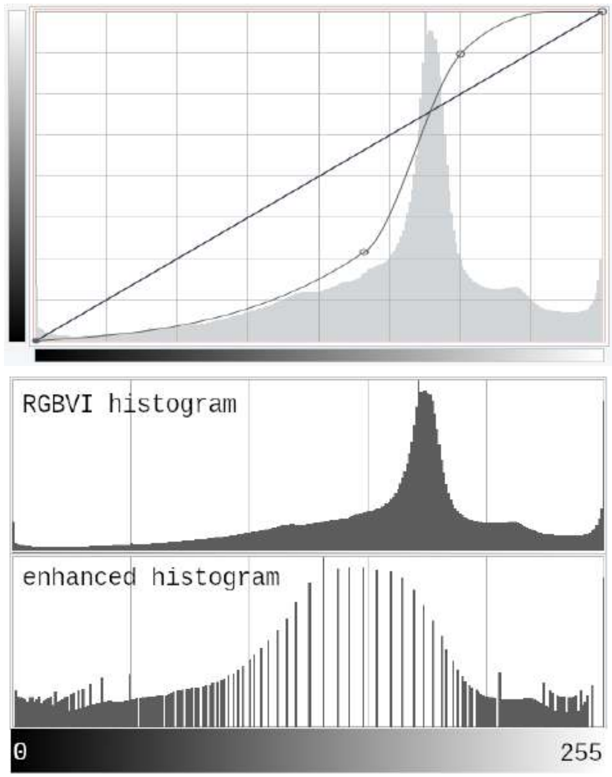

Fig.3. Enhancing function and images histograms

A monotonic mapping function was applied to the entire urban imagery dataset. This transformation preserved the relative ranking and proportional ratios between the RGBVI pixel values for the war, while significantly enhancing the visual contrast and discriminability of urban park spaces.

While the vegetation canopy is highly discernible within the contrast-enhanced imagery, establishing a precise radiometric threshold within the 8-bit [0:255] digital number (DN) range to separate vegetated from non-vegetated pixels presents a classification challenge. Typically, the maximum saturation value of 255 indicates dense, healthy, full-canopy vegetation; however, this accounts for only a fraction of the total urban vegetation cover, omitting areas with sparse or mixed canopies. To calibrate the thresholding methodology, a validation subset-designated as Sector [2:4] within the 5x5 grid – isolated. This area is characterized by an environmental composition consisting of approximately 25% tree-covered parkland and 75% built-up urban matrix (Fig. 4).

Two homogeneous urban areas were extracted from the validation sector to perform a discrete comparative analysis: a dedicated parkland zone (Fig. 5). The radiometric distribution profiles of these zones were evaluated using both pixel-density histograms and inverse cumulative percentage frequency curves.

Fig.4. Section [2:4] of Elbasan (street Koco Brisku) and its enhanced RGBVI image.

An empirical threshold at the 75% pixel-value level (corresponding to a digital number of 192) was established to separate non-vegetated urban surfaces from vegetated parklands This value was derived from the geometric profile of the histograms: given that the vast majority of pixels within the scene represent non-vegetated surfaces, the predominant urban spectral peak occurred at 175, while the distinct vegetative pixel distribution initiated at approximately 200. To isolate the canopy, the contrast-enhanced RGBVI image of the park zone was converted into a binary (black-and-white) mask via a hard-threshold operation. Pixels with values greater than or equal to 192 (75% of the maximum 8-bit value of 255) were classified as 255 (white, representing vegetation), while all remaining pixels below this threshold were assigned a value of 0 (black, representing non-vegetated surfaces). The resulting binary mask yielded white pixel values of 60%, which was designated as the definitive baseline for healthy vegetation canopy coverage within the park. This threshold of 192 was subsequently applied to the purely urban area and the entire multi-zone sector [2,4] to calculate their respective vegetation coverage percentages (Figure 6).

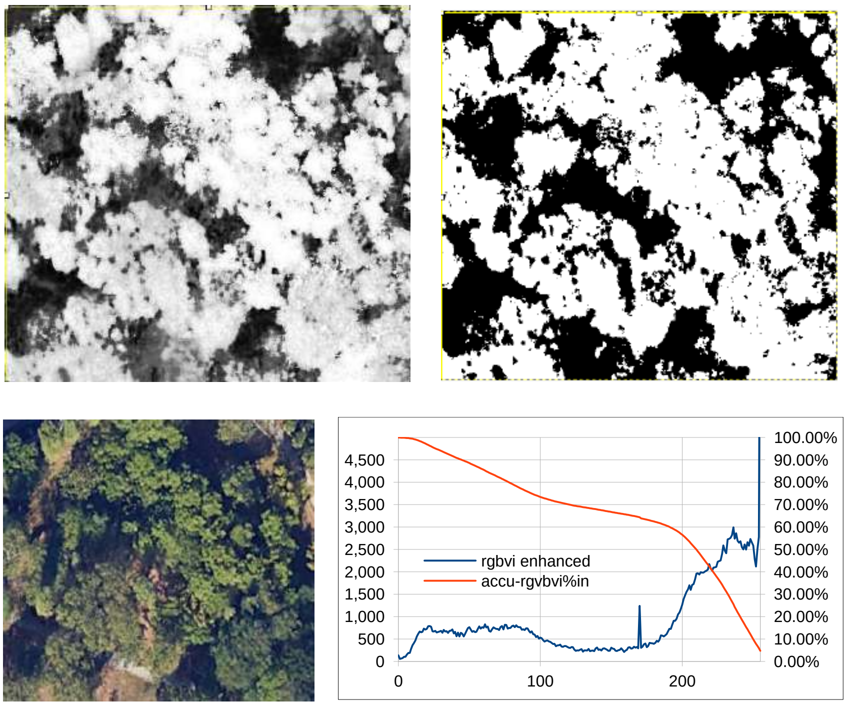

Fig.5. Enhanced and black-and-white RGBVI images of the park area and histograms.

The radiometric histograms for the comprehensive sector [2:4] (previously displayed in Fig. 4) are detailed in Figure 7. Using the calibrated threshold the calibrated threshold, the fractional vegetation cover was calculated as 11% for the dedicated urban area and 25% for the entire sector mosaic.

To scale this analysis across boarder studies, the contrast-enhanced RGBVI image of the entire city was exported and converted into numerical raster matrix using the image processing software IMAGEJ. This matrix was subsequently processed via a custom –built proprietary to compute the exact fractional vegetation coverage percentages, mean pixel values, and corresponding standard deviations (σ) for each individual sector within a 5x5 grid.

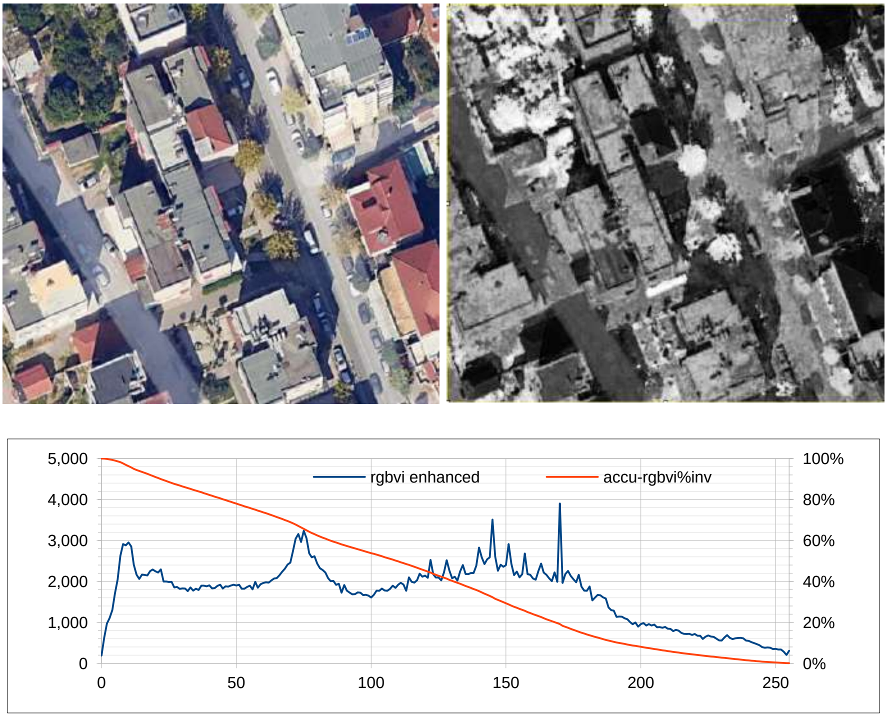

Fig. 6. Visible and enhanced RGBVI image of the urban area and its histogram.

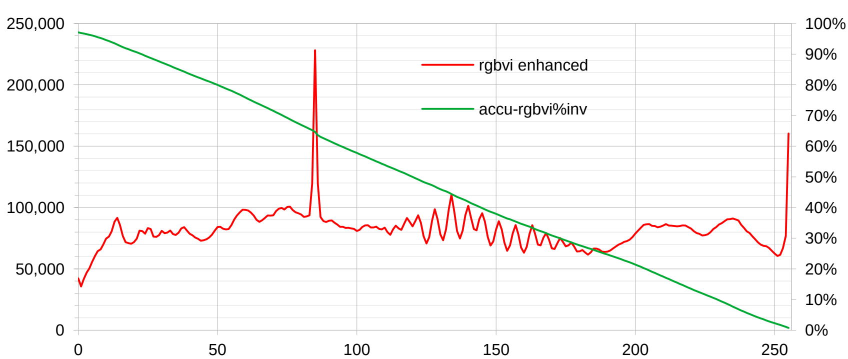

Fig.7. Histograms of the city section [2:4] (Fig. 4).

3. Evaluation of vegetation cover in the city of Elbasani

The descriptive statistics for calculated fractional vegetation coverage percentages, mean contrast-enhanced RGBVI values (mapped to 8-bit [0,255] digital number range), and their corresponding standard deviation (σ) for each grid sector are presented in Table 2—4.

Table 1. RGBVI Averages

126	121	115	120	131
122	109	107	127	130
128	102	109	130	150
133	130	131	137	158
129	130	127	154	154

Table 2. RGBVI STDEV

68	73	68	69	76
71	72	72	72	74
70	75	77	73	73
73	74	79	72	68
67	74	77	72	63

Table 3. Vegetation coverage

20.36%	22.01%	16.97%	20.52%	29.23%
21.23%	17.11%	17.23%	24.73%	27.20%
22.55%	18.03%	20.95%	24.19%	37.75%
26.31%	26.24%	28.93%	25.99%	40.70%
20.70%--	24.34%	24.38%	36.27%	32.55%

Figure 8 illustrates the mapping of calculated values into the city map. 8.

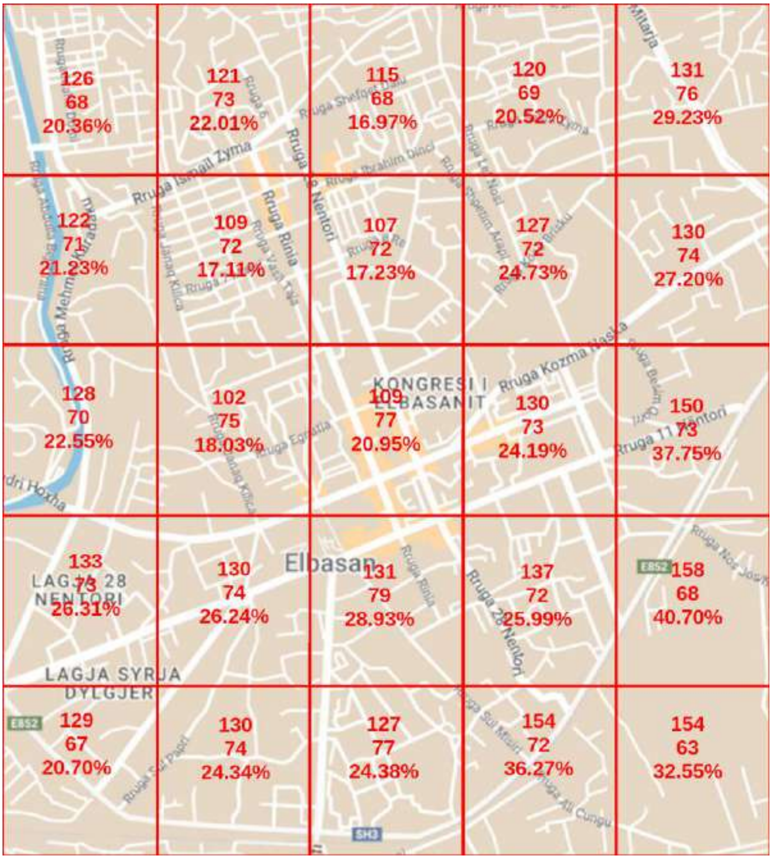

Fig. 8. Distribution in the city map of RGBVI averages and related standard deviations, and the vegetation coverage percentage of the surface

Across the entire administrative extent of the city, the mean radiometric RGBVI value was calculated at 128 (within absolute [0:255] range] with a standard deviation (σ) of 74. The total fractional vegetation canopy cover for the entire urban area was determined to be 25.14%. When analysing the spatial variation between the between the 25 discrete grid sectors, the inter-sector standard deviation for vegetation coverage was 6.38%.

4. CONCLUSIONS

This study demonstrates that visible-spectrum (RGB) remote sensing imagery can effectively serve as an accessible proxy for evaluating and benchmarking relative greenspace distribution within urban environments. However, the performance and accuracy of these visible-spectrum indices are highly sensitive to the phenological state of the vegetation, atmospheric illumination intensity, and sensor-look-angles at the time of data acquisition. Consequently, prior to scaling a specific visible-spectrum vegetation index (VVi) across an entire urban landscape, it is methodologically imperative to perform localized radiometric calibration within highly homogenous, micro-scale validation subsets.

For the case of Elbasan City, the total urban vegetation canopy cover was quantified at 25.14% ± 6.38% across the 25 sectors. Accounting for localized radiometric distortions -such as chromatic aberrations, structural shadows, structural edge effects in high resolution aerial orthophotos, and varying seasonal or meteorological conditions-an empirical margin of error of ±2% to 3%should be factored into the final classification accuracy assessment. Furthermore, an inherent constraint of relying purely on visible spectrums is the potential for spectral confusion; for instance, synthetic surfaces such as artificial turf (plastic grass) or faux decorative plants exhibit a green spectral signature identical to natural foliage within the RGB bands and will be misclassified as true vegetation.

Spatially, the lowest vegetation densities within Elbasan are heavily concentrated in the “triangle” zone, which directly borders the industrial the metallurgic plant and acts as major transportation crossroads. Conversely, significantly higher canopy densities are observed across the southern and eastern sectors of the city, culminating in peak vegetative abundance within suburban southeastern perimeter adjacent to the Shkumbin River corridor.

ACKNOWLEDGEMENTS

This study was conducted within the framework of the research e project titled, *Optimizing the relationship between building infrastructures and green infrastructures as one of the main elements in improving the environment and the sustainable development of urban areas. A comparative observation of these issues in some cities/neighbourhoods of our country* (*Case study: Elbasan and Tirana*). This project was executed by a collaborative a group of researchers and Metropolitan University of Tirana (UMT), and the Academy of Sciences of Albania, with the financial support of the National Agency for Scientific Research, Technology and Innovation (AKKSHI / NASRT). The case study focusing on the urban vegetation cover in Elbasan city was implemented as a key component of

this project, aimed at assessing methodologies for improving the urban microclimate, environmental quality, and ambient air safety.

Ethics approval. Not applicable. This study does not involve human participants, animals, or sensitive personal data. The research is based entirely on the analysis of publicly available satellite imagery and open-source data.

Data sharing statement. The datasets generated and analysed during the current study (including the processed Google Earth imagery and software scripts) are available from the corresponding author upon reasonable request.

Authors' Contributions. **NF.:** conceptualization, methodology, software, data curation, formal analysis, writing – original draft, **H.H.:** validation, investigation, visualization, writing – review & editing, supervision.

All authors have read and agreed to the published version of the manuscript.

AI Statement. The authors declare that no AI-assisted technologies were used in the generation of the data analysis, or image processing.

Declaration of Interest. The authors declare that they have no competing financial interests.

Funding. A project on this subject carried out by the University Metropolitan Tirana, in recent years, supported by modest funding from National Agency for Scientific Research, Technology and Innovation (NASRTI) has produced some data that have been used in this paper. For this, more specifically, there is also an acknowledgement at the end of the paper.

REFERENCES

Bendig J, Yu K, Aasen H, Bolten A, Bennertz S, Broscheit J, Gnyp ML, Bareth G. 2015. Combining UAV-based plant height from crop surface models, visible, and near infrared vegetation indices for biomass monitoring in barley. *International Journal of Applied Earth Observation and Geoinformation*, **39:** 79-87. 10.1016/j.jag.2015.02.012.

GIMP. Gnu Image Manipulation Program. https://gimp.org/.

Google Earth. https://earth.google.com/.

Google Maps. https://maps.google.com/.

IMAGEJ. Image Processing and Analysis in Java. https://imagej.net/.

Lussem U, Bolten A, Gnyp ML, Jasper J, Bareth G. 2018. Evaluation of RGB-based vegetation indices from UAV imagery to estimate forage yield in grassland. *The International Archives of the Photogrammetry, Remote Sensing and Spatial Information Sciences*, **Volume XLII-3**, 1215-1219. https://doi.org/10.5194/isprs-archives-XLII-3-1215-2018.

QGIS. Spatial without Compromise. https://qgis.org/.

ENERGY OF A SPIN-UNPOLARISED TWO-DIMENSIONAL ELECTRON GAS SEPARATED FROM A NEUTRALISING LAYER

Orion CIFTJA
Department of Physics, Prairie View A&M University, Prairie View, Texas 77446, USA

Author for correspondence: ogciftja@pvamu.edu
OC, 0000-0001-5107-0533

ABSTRACT

We study a system of electrons forming a spin-unpolarised two-dimensional electron gas suspended over a neutralising jellium background layer. While a spin-unpolarised two-dimensional electron gas system represents the theoretical ground state in absence of interactions, we employ an anti-symmetrized Slater determinant wave function of plane waves to investigate the system when interactions are introduced. We analyse the dependence of the total energy on the density of the system and the separation between the two-dimensional electron gas and its neutralising layer. Our findings reveal that this layer separation introduces an added energy contribution that effectively behaves like a kinetic energy term. Consequently, the total energy of the electron liquid state increases with growing separation, an effect that becomes significantly more pronounced in the high-density regime.

Keywords: Energy, Two-dimensional electron gas, Spin-unpolarised state, Jellium background

Publisher: Academy of Sciences of Albania

Citation: Ciftja O. 2026. Energy of a spin-unpolarised two-dimensional electron gas separated from a neutralising layer. *Albanian Journal of Natural and Technical Sciences (AJNTS),* **31 (3):** 45-63.
https://doi.org/10.67537/ajnts3103028
Classification: Research
Subject Category Applied Sciences subject category: Applied Physics + Condensed Matter Engineering

1. INTRODUCTION

Recent advances in fabrication techniques have renewed interest in two-dimensional electron gas (2DEG) systems, which serve as versatile platforms for exploring a wide range of quantum phenomena. Such systems can be created in metal-oxide-semiconductor field-effect transistors (MOSFETs), where electrons beneath the gate oxide are confined to the semiconductor-oxide interface in inversion mode (Shenoy *et al*. 1997; Li *et al*. 2002; Hasanuzzaman *et al*. 2004). By tuning the transverse potential well, only the lowest quantum level is populated, effectively freezing motion perpendicular to the interface and creating an essentially two-dimensional (2D) system. Alternative methods for realizing 2D structures use heterojunctions, in which electrons are confined at the interface between two semiconductors (Kane *et al*. 1993; Harrell *et al*. 1999; Mak *et al*. 2010). This approach is particularly favoured in quantum Hall studies (Morf and Halperin, 1986; Lado 2003; Ciftja and Wexler, 2003), as it allows the formation of a triangular quantum well that restricts motion normal to the interface. Electrons in heterojunctions such as GaAs/AlGaAs typically show much higher mobilities than those in MOSFETs, making them ideal for studying low-temperature quantum phenomena.

From a theoretical perspective, an established framework for modelling 2DEGs is the uniform electron gas in a jellium background, where electrons interact through Coulomb forces within a uniform, positively charged 2D layer (Farid *et al*. 1993; Fetter and Walecka, 2003). This simple model has been remarkably successful in capturing the essential physics of 2DEGs and has served as the foundation for many studies under different approximations (Sim *et al*. 1986; Choudhury and Ghosh, 1995). It provides a natural platform to study quantum phase transitions as a function of electron density. At high densities, the electrons typically form a liquid state, but at sufficiently low densities, they crystallize into a 2D Wigner solid (Crandall and Williams, 1971; Pudalov *et al*. 1994). In the thermodynamic limit, an infinite 2DEG is fully characterized by its electron number density (Ciftja 2021) and determining the precise density at which the liquid-solid transition occurs remains an active area of research (Tanatar and Ceperley, 1989; Kwon *et al*. 1993; Attaccalite *et al*. 2003; Ceperley, 1978; Zong *et al*. 2002), due to the extremely small energy differences between these two quantum phases.

The basic treatment of a 2DEG employs an antisymmetrised Slater determinant within the Hartree-Fock (HF) approximation (Slater, 1929; Ashcroft and Mermin, 1976; Giuliani and Vignale, 2005). This approach yields an analytical expression for the total energy in terms of two competing contributions: kinetic energy and exchange (potential) energy. Other contributions, collectively termed correlation energy, are neglected

(Gell-Mann and Brueckner, 1957; Rajagopal and Kimball, 1977; Isihara and Ioriatti, 1980; Sun *et al*, 2010), but more sophisticated methods can include these effects for a higher accuracy. Conventional treatments typically assume that both the 2DEG and 2D neutralising layers are on the same plane.

In this study, we alter this model and, consider a 2DEG in which the electron layer is parallel to, but separated by a finite distance from, the 2D neutralising jellium background. If a constant and isotropic effective mass for the electrons is assumed, the system in the thermodynamic limit will be fully described by two parameters: the average inter-particle distance (which is related to the density) and the 2DEG-background layer separation. The main aim of our research is to investigate how the separation between the layers influences the total energy of the 2DEG and to define whether it gives rise to subtle, additional effects.

This study is focused on a spin-unpolarised 2DEG, which represents the lowest-energy configuration in the absence of interactions. The corresponding fully spin-polarised 2DEG system has been analysed in earlier studies (Ciftja *et al*. 2021). This study considers an added geometric degree of freedom and offers new insights into how finite separations between electrons and the neutralising background influence the energetics and stability of 2D electron systems, potentially guiding future experiments and theoretical studies on high-mobility 2DEGs and layered 2D materials.

The reminder of this paper is organised as follows. In Section 2, we define the model, the Hamiltonian, and the wave function for a spin-unpolarised 2DEG system. In Section 3, we explain the calculation of the kinetic energy. In Section 4, we explain the formalism for calculating various potential energy terms and derive several analytic expressions. In Section 5, we present the main results of this study. Finally, in Section 6, we briefly present the conclusions and discuss some important implications of our findings for future work.

2. MODEL

We consider a 2DEG system of N electrons separated by an arbitrary distance, d from a neutralising 2D jellium background layer (Ciftja *et al*. 2015). The 2DEG and jellium layers are assumed to occupy the same area, A. The electron number density is expressed as:

$$\rho_0 = \frac{N}{A} = \frac{1}{\pi\,(r_s\,a_B)^2}\,, \qquad (1)$$

where r_s is the dimensionless Wigner-Seitz parameter and a_B is the Bohr radius. For an infinite 2DEG system in the thermodynamic limit, the electron number number, ρ_0 is constant as $N \to \infty$ and $A \to \infty$. A schematic view of the system under consideration is shown in Fig. 1.

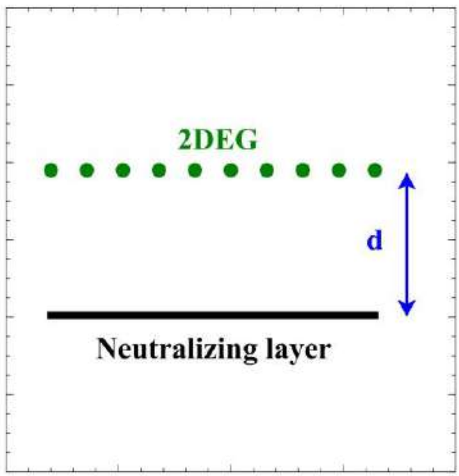

Fig. 1: Schematic view of a 2DEG system (filled circles) over a neutralising 2D jellium layer. The separation between the two layers is denoted as d.

In the absence of interactions, the electrons are considered as free particles moving in a 2D square region with area, $A = L^2$. If periodic boundary conditions (PBC) are imposed in both the x and y directions, the single-particle states of electrons are 2D plane waves:

$$\phi_{\vec{k}}(\vec{r}) = \frac{1}{\sqrt{A}}\, e^{i\,\vec{k}\,\vec{r}}\,, \qquad (2)$$

where $\vec{r} = (x, y)$ is a 2D position vector and $i = \sqrt{-1}$ is the imaginary unit. The allowed values of the wave vector $\vec{k} = (k_x, k_y)$ consistent with the imposed PBC are:

$$\begin{cases} k_x = \frac{2\pi}{L} n_x \quad ; \quad n_x = 0, \pm 1, \pm 2, \ldots \\ k_y = \frac{2\pi}{L} n_y \quad ; \quad n_y = 0, \pm 1, \pm 2, \ldots \end{cases} \tag{3}$$

Electrons are fermions and occupy the quantum states from the lowest to the highest energy, consistent with Pauli's exclusion principle.

Let us assume that N_α is the number of electrons with spin "α" ("up") and N_β is the counterpart with spin "β" ("down"). One can write:

$$N_\alpha + N_\beta = N \ , \tag{4}$$

where N is the total number of electrons. One defines the spin-resolved number densities as follows:

$$\rho_\alpha = \frac{N_\alpha}{A} \quad ; \quad \rho_\beta = \frac{N_\beta}{A} \ . \tag{5}$$

At this juncture, it is easy to see that:

$$\rho_\alpha + \rho_\beta = \rho_0 \ , \tag{6}$$

where $\rho_0 = N/A$ is the total number density. In absence of interactions, one has N_α electrons filling a 2D Fermi disk up to the state with wave vector, $k_{F\,\alpha}$ and N_β electrons filling a 2D Fermi disk up to the state with wave vector, $k_{F\,\beta}$. The two spin-resolved number densities can be written as:

$$\rho_\alpha = \frac{k_{F\,\alpha}^2}{4\pi} \quad ; \quad \rho_\beta = \frac{k_{F\,\beta}^2}{4\pi} \ . \tag{7}$$

The electron system is described by the Hamiltonian:

$$\hat{H} = \hat{T} + \hat{V} \ , \tag{8}$$

where

$$\hat{T} = \sum_{i=1}^{N} \frac{\hat{p}_i^2}{2\,m} \ , \tag{9}$$

is the kinetic energy operator and

$$\hat{V} = \hat{V}_{ee} + \hat{V}_{eb} + \hat{V}_{bb} \,, \qquad (10)$$

is the potential energy operator that represents, the electron-electron (ee), electron-background (eb), and background-background (bb) interaction potential energy operators.
The *ee* potential energy operator is written as:

$$\hat{V}_{ee} = \frac{1}{2}\sum_{i=1}^{N}\sum_{j\neq i}^{N} v\,(|\vec{r}_i - \vec{r}_j|) \,, \quad (11)$$

where

$$v(|\vec{r}_i - \vec{r}_j|) = \frac{k_e\, e^2}{|\vec{r}_i - \vec{r}_j|} \,, \qquad (12)$$

is the Coulomb interaction potential between two electrons with charge $-e$ $(e > 0)$ and k_e is Coulomb's electric constant. Note that $\vec{r}_{i,j}$ are 2D vectors. The *eb* potential energy operator is written as:

$$\hat{V}_{eb} = -\rho_0 \sum_{i=1}^{N} \iint_A d^2\, r'\, v_d(|\vec{r}_i - \vec{r}\,'|) \,, \quad (13)$$

where

$$v_d(|\vec{r}_i - \vec{r}\,'|) = \frac{k_e\, e^2}{\sqrt{|\vec{r}_i - \vec{r}\,'|^2 + d^2}} \,, \qquad (14)$$

with $d \geq 0$ being the separation distance between the layer of electrons and the 2D jellium background layer. The 2D vector $\vec{r}\,'$ in Eq.(13) is the continuous background coordinate while $\vec{r}_i$ is the 2D position vectors of electrons. The *bb* energy term is written as:

$$\begin{aligned} \hat{V}_{bb} \quad = \quad & \frac{\rho_0^2}{2} \iint_A d^2\, r \iint_A d^2\, r'\ v(|\vec{r} - \vec{r}\,'|) = \\ & \frac{\rho_0^2}{2} \iint_A d^2\, r_1 \iint_A d^2\, r_2\ v(|\vec{r}_1 - \vec{r}_2|) \,, \end{aligned} \qquad (15)$$

where the background dummy variables, $\vec{r}$ and $\vec{r}\,'$ have been replaced by $\vec{r}_1$ and $\vec{r}_2$ under the sign of the integral.

In the case of an arbitrary spin polarisation of the system, the system of electrons can be described with a normalised anti-symmetric N-particle wave function that is built as a Slater determinant of the ortho-normalised single-particle space-spin orbitals. A normalised N-particle wave function that is properly antisymmetric and is an eigenstate of the many-particle free Hamiltonian is constructed as:

$$|\Psi\rangle = \frac{1}{\sqrt{N!}}\, Det\left\{\phi_{\vec{k}_j\,\alpha,\beta}(\vec{r})\right\}, \qquad (16)$$

where the single-particle states, $\phi_{\vec{k}_j\,\alpha,\beta}(\vec{r})$ are ortho-normalised 2D plane waves. Note that the prefactor multiplying the Slater determinant is suitably chosen to normalise to one the overall wave function.

For a spin-unpolarised state, the following equation is obtained:

$$N_\alpha = N_\beta = \frac{N}{2}, \qquad (17)$$

which implies:

$$\rho_\alpha = \rho_\beta = \frac{\rho_0}{2}. \qquad (18)$$

3. KINETIC ENERGY

It is easy to calculate the expectation value of the total kinetic energy operator for the spin-resolved system as follow:

$$\langle\hat{T}\rangle = \frac{N_\alpha}{2}\,\epsilon_{F\,\alpha} + \frac{N_\beta}{2}\,\epsilon_{F\,\beta}, \qquad (19)$$

where

$$\epsilon_{F\,\alpha} = \frac{\hbar^2}{2\,m}\,k_{F\,\alpha}^2 \quad ; \quad \epsilon_{F\,\beta} = \frac{\hbar^2}{2\,m}\,k_{F\,\beta}^2, \qquad (20)$$

are the spin-resolved Fermi energies. In a shorthand notation, $\langle\hat{O}\rangle = \langle\Psi|\hat{O}|\Psi\rangle/\langle\Psi|\Psi\rangle$ represents the quantum expectation value of operator $\hat{O}$ with respect to the wave function, $|\Psi\rangle$. One can see from Eq. (7) that:

$$k_{F\,\alpha}^2 = 4\,\pi\,\rho_\alpha \quad ; \quad k_{F\,\beta}^2 = 4\,\pi\,\rho_\beta. \qquad (21)$$

From this, we can conclude that:

$$k_{F\,\alpha}^2 + k_{F\,\beta}^2 = 4\,\pi\,(\rho_\alpha + \rho_\beta) = 4\,\pi\,\rho_0\,. \qquad (22)$$

Because we are dealing with a spin-unpolarised state, we define the Fermi energy of the spin-unpolarised state simply as ϵ_F and write:

$$\epsilon_F = \epsilon_{F\,\alpha} = \epsilon_{F\,\beta} = \frac{\hbar^2}{2\,m}\,k_F^2\,, \qquad (23)$$

Where

$$k_F^2 = k_{F\,\alpha}^2 = k_{F\,\beta}^2 = 2\,\pi\,\rho_0\,. \qquad (24)$$

For a spin-unpolarised state, $N_\alpha = N_\beta = N/2$ as in Eq.(17). Therefore, based on Eq.(17) and Eq.(23), one can write the expression in Eq.(19) for the expectation value of the total kinetic energy operator as:

$$\langle\hat{T}\rangle = \frac{N}{2}\,\epsilon_F\,, \qquad (25)$$

where ϵ_F is defined in Eq.(23).

4. POTENTIAL ENERGY

To calculate the expectation value of various potential energy terms, one must first define the spin-resolved one-particle density functions:

$$\rho_\alpha(\vec{r}) = \sum_{j=1}^{N_\alpha} |\,\phi_{\vec{k}_j\,\alpha}(\vec{r})|^2 \quad ; \quad \rho_\beta(\vec{r}) = \sum_{j=1}^{N_\beta} |\,\phi_{\vec{k}_j\,\beta}(\vec{r})|^2\,, \qquad 26)$$

where $\phi_{\vec{k}_j\,\alpha}(\vec{r})$ are the plane-wave states for spin "α" electrons and $\phi_{\vec{k}_j\,\beta}(\vec{r})$ are the spin "β" counterparts. Note that:

$$\rho_\alpha(\vec{r}) + \rho_\beta(\vec{r}) = \rho(\vec{r}) = \rho_0\,, \qquad (27)$$

where $\rho(\vec{r})$ is the total one-particle density function. Similarly, the spin-resolved one-particle density matrices can be defined as follows:

$$\rho_\alpha(\vec{r}_1,\vec{r}_2) = \sum_{j=1}^{N_\alpha} \phi_{\vec{k}_j\,\alpha}(\vec{r}_1)^* \phi_{\vec{k}_j\,\alpha}(\vec{r}_2) \qquad (28)$$

and

$$\rho_\beta(\vec{r}_1,\vec{r}_2) = \sum_{j=1}^{N_\beta} \phi_{\vec{k}_j\,\beta}(\vec{r}_1)^* \phi_{\vec{k}_j\,\beta}(\vec{r}_2)\,. \qquad (29)$$

At this juncture, we have listed all the necessary elements that allow us to derive general expressions when we have two types of spin polarisation. One can verify that the expectation values of $\hat{V}_{ee}$ are:

$$\langle \hat{V}_{ee} \rangle = \frac{1}{2}\iint_A d^2 r_1\, \rho(\vec{r}_1) \iint_A d^2 r_2\, \rho(\vec{r}_2)\; v(r_{12}) - \frac{1}{2}\iint_A d^2 r_1 \iint_A d^2 r_2\, |\rho_\alpha(\vec{r}_1,\vec{r}_2)|^2\; v(r_{12})$$
$$-\frac{1}{2}\iint_A d^2 r_1 \iint_A d^2 r_2\, |\rho_\beta(\vec{r}_1,\vec{r}_2)|^2\; v(r_{12})\,, \qquad (30)$$

where $v(r_{12})$ is the Coulomb interaction potential, $r_{12} = |\vec{r}_1 - \vec{r}_2|$ is the pair separation distance in shorthand notation, $\rho_{\alpha,\beta}(\vec{r})$ are defined in Eq. (26), and $\rho_{\alpha,\beta}(\vec{r}_1,\vec{r}_2)$ are defined in Eq. (28) and Eq. (29), respectively.

The expectation value of $\hat{V}_{eb}$ can be written as:

$$\langle \hat{V}_{eb} \rangle = -\rho_0 \iint_A d^2 r_1\, \rho(\vec{r}_1) \iint_A d^2 r_2\; v_d(r_{12})\,, \quad (31)$$

where we substituted the dummy variable $\vec{r}\,'$ in Eq. (13) with $\vec{r}_2$.

Finally, the expectation value of $\hat{V}_{bb}$ is:

$$\langle \hat{V}_{bb} \rangle = \frac{\rho_0^2}{2} \iint_A d^2 r_1 \iint_A d^2 r_2\; v(r_{12})\,. \qquad (32)$$

For a spin-unpolarised state, the following equation is obtained:

$$\rho_\alpha(\vec{r}) = \rho_\beta(\vec{r}) = \frac{\rho(\vec{r})}{2} = \frac{\rho_0}{2}\,. \qquad (33)$$

It is straightforward to show that the spin-resolved one-particle density matrices are, respectively:

$$\rho_\alpha(\vec{r}_1,\vec{r}_2) = 2\,\rho_\alpha\, \frac{J_1(k_{F\,\alpha}\, r_{12})}{(k_{F\,\alpha}\, r_{12})} \qquad (34)$$

and

$$\rho_\beta(\vec{r}_1,\vec{r}_2) = 2\,\rho_\beta\,\frac{J_1(k_{F\,\beta}\,r_{12})}{(k_{F\,\beta}\,r_{12})}\,, \qquad (35)$$

where $J_1(x)$ denotes the Bessel function of the first kind of order one. Without lack of generality one can rewrite the potential, $v_d(r_{12})$ in Eq. (31) as:

$$v_d(r_{12}) = v(r_{12}) + v_d(r_{12}) - v(r_{12})\,. \qquad (36)$$

This simple step allows one to easily see which terms cancel in the aggregate expression for the potential energy:

$$\langle \hat{V} \rangle = \langle \hat{V}_{ee} \rangle + \langle \hat{V}_{eb} \rangle + \langle \hat{V}_{bb} \rangle\,. \qquad (37)$$

The final result reads:

$$\langle \hat{V} \rangle = \;\; = \; -\frac{1}{2}\iint_A d^2 r_1 \iint_A d^2 r_2\, |\rho_\alpha(\vec{r}_1,\vec{r}_2)|^2\; v(r_{12}) - \frac{1}{2}\iint_A d^2 r_1 \iint_A d^2 r_2\, |\rho_\beta(\vec{r}_1,\vec{r}_2)|^2\; v(r_{12})$$
$$-\rho_0^2 \iint_A d^2 r_1 \iint_A d^2 r_2\; [v_d(r_{12}) - v(r_{12})]\,. \qquad (38)$$

The first two integrals on the right-hand-side (RHS) of Eq.(38) represent the exchange energy, $\langle \hat{V}_x \rangle$ which can be calculated analytically in the thermodynamic limit. The mathematical details of such a calculation can be found in the Appendix A of (Ciftja, 2015). After calculating the exchange energy, the result can be written in a compact form as:

$$\langle \hat{V} \rangle = \langle \hat{V}_x \rangle + \Delta V(d)\,, \qquad (39)$$

where

$$\langle \hat{V}_x \rangle = -\frac{4}{3\,\pi}\,N_\alpha\,k_{F\,\alpha}\,k_e\,e^2 - \frac{4}{3\,\pi}\,N_\beta\,k_{F\,\beta}\,k_e\,e^2 \qquad (40)$$

and

$$\Delta V(d) = \rho_0^2 \iint_A d^2 r_1 \iint_A d^2 r_2\; [v(r_{12}) - v_d(r_{12})] \qquad (41)$$

is the last integral in the RHS of Eq.(38) slightly rewritten. The energy term, $\Delta V(d)$ originates from the separation in space between the 2DEG and the neutralising 2D jellium background layer.

For a spin-unpolarised state, $N_\alpha = N_\beta = N/2$ and, $k_{F\,\alpha} = k_{F\,\beta} = k_F$ leading to an exchange energy of:

$$\langle \hat{V}_x \rangle = -\frac{4}{3\,\pi}\, N\, k_F\, k_e\, e^2\, . \qquad (42)$$

Consequently, the expression for $\langle \hat{V} \rangle$ in Eq. (39) becomes:

$$\langle \hat{V} \rangle = -\frac{4}{3\,\pi}\, N\, k_F\, k_e\, e^2 + \Delta V(d)\, . \qquad (43)$$

The calculation of $\Delta V(d)$ in the thermodynamic limit requires careful consideration. To start with, we write it explicitly as:

$$\Delta V(d) \;=\; k_e\, e^2\, \rho_0^2 \iint_A d^2\, r_1 \iint_A d^2\, r_2 \left(\frac{1}{r_{12}} - \frac{1}{\sqrt{r_{12}^2 + d^2}} \right) = k_e\, e^2\, \rho_0^2\; I(d)\, , \qquad (44)$$

where

$$\mathrm{I(d)} = \iint_{\mathrm{A}} \mathrm{d}^2\, \mathrm{r}_1 \iint_{\mathrm{A}} \mathrm{d}^2\, \mathrm{r}_2 \left(\frac{1}{\mathrm{r}_{12}} - \frac{1}{\sqrt{\mathrm{r}_{12}^2 + \mathrm{d}^2}} \right). \qquad (45)$$

To obtain the correct result in the thermodynamic limit ($N \to \infty$; $A \to \infty$, but $\rho_0 = N/A$ constant), we initially assume that the surface area is very large (but finite) and has circular disk symmetry, $A = \pi\, R^2$. It is only at the end of the calculations that one takes the explicit $R \to \infty$ limit (when necessary). It follows that:

$$\mathrm{I(d)} = \mathrm{A} \iint_{\mathrm{A}\to\infty} \mathrm{d}^2\, \mathrm{r}_{12} \left(\frac{1}{\mathrm{r}_{12}} - \frac{1}{\sqrt{\mathrm{r}_{12}^2 + \mathrm{d}^2}} \right). \qquad (46)$$

The next step is to write:

$$\mathrm{I(d)} = \mathrm{A}\,(2\,\pi) \int_0^{\mathrm{R}\to\infty} \mathrm{d}\,\mathrm{r}_{12} \left(1 - \frac{\mathrm{r}_{12}}{\sqrt{\mathrm{r}_{12}^2 + \mathrm{d}^2}} \right). \qquad (47)$$

By using the integral formula $\int dx\, x/\sqrt{x^2+d^2} = \sqrt{x^2+d^2}$ and carefully performing the $R \to \infty$ limit, the result for $I(d)$ becomes:

$$\mathrm{I(d) = A\,(2\,\pi)\,d\,.} \qquad (48)$$

By substituting the result from Eq. (48) into Eq. (44), we obtain:

$$\mathrm{\Delta V(d) \;=\; k_e\, e^2\, \rho_0^2\, A\,(2\,\pi)\,d = (2\,\pi)\,N\,\rho_0\,k_e\,e^2\,d\,.} \qquad (49)$$

One sees that $\Delta V(d)$ is positive and proportional to the separation distance ($\propto d$) between the 2DEG and 2D neutralising layer.

5. RESULTS

It is customary in the literature covering this field to express the energies of a 2DEG system in units of Rydbergs (Ry) as follows:

$$1\text{ Ry} = \frac{\hbar^2}{2\,m\,a_B^2} = \frac{k_e\,e^2}{2\,a_B}\,, \qquad (50)$$

where Bohr's radius is defined as:

$$a_B = \frac{\hbar^2}{m\,k_e\,e^2}\,. \qquad (51)$$

The density of a 2DEG is typically expressed in terms the Wigner-Seitz dimensionless parameter, r_s defined in Eq.(1).

The following units transformations of are useful for the results that follow:

$$\epsilon_F = \frac{\hbar^2}{2\,m}\,k_F^2 = (k_F\,a_B)^2\,\frac{\hbar^2}{2\,m\,a_B^2} = (k_F\,a_B)^2\,\frac{k_e\,e^2}{2\,a_B} \qquad (52)$$

and

$$k_F\,k_e\,e^2 = (k_F\,a_B)\,\frac{k_e\,e^2}{a_B} = 2\,(k_F\,a_B)\,\frac{k_e\,e^2}{2\,a_B}\,. \qquad (53)$$

One can also verify that for the spin-unpolarised state:

$$(k_F\,a_B\,r_s)^2 = 2\,. \qquad (54)$$

Based on these results, the kinetic energy per particle can be written as:

$$t = \frac{\langle \hat{T} \rangle}{N} = \frac{1}{2}\,(k_F\,a_B)^2\,\frac{k_e\,e^2}{2\,a_B} = \frac{1}{r_s^2}\,\frac{k_e\,e^2}{2\,a_B}\,. \qquad (55)$$

Similarly, the exchange energy per particle can be written as:

$$\epsilon_x = \frac{\langle \hat{V}_x \rangle}{N} = -\frac{4}{3\,\pi}\,k_F\,k_e\,e^2 = -\frac{8}{3\,\pi}\,(k_F\,a_B)\,\frac{k_e\,e^2}{2\,a_B} = -\frac{8\sqrt{2}}{3\,\pi}\,\frac{1}{r_s}\,\frac{k_e\,e^2}{2\,a_B}\,. \qquad (56)$$

The energy per particle resulting from the layer separation is derived using the result from Eq.(49) as follows:

$$\Delta\epsilon(d) = \frac{\Delta V(d)}{N} = (2\,\pi)\,\rho_0\,k_e\,e^2\,d = \frac{4}{r_s^2}\,\frac{d}{a_B}\,\frac{k_e\,e^2}{2\,a_B}\,. \qquad (57)$$

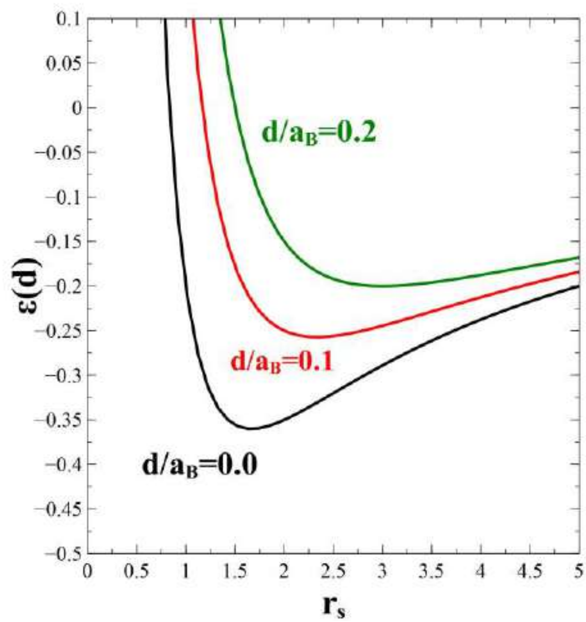

Fig. 2: Energy per particle, $\epsilon(d)$ as a function of r_s for several values of the separation distance, $d/a_B = 0{,}0.1$ and 0.2 (from left to right). The results correspond to a fully spin-unpolarised 2DEG system in which the 2DEG is separated from the background layer by a distance, d. The minimum of energy shifts to larger values of r_s as d/a_B increases. The energy per particle is expressed in units of $k_e\,e^2/(2\,a_B)$.

The total energy per particle in the thermodynamic limit is calculated by adding all the terms:

$$\epsilon(d) = t + \epsilon_x + \Delta\epsilon(d)\ . \qquad (58)$$

The final expression is as follows:

$$\epsilon(d) = \left[\left(1 + 4\,\frac{d}{a_B}\right)\frac{1}{r_s^2} - \frac{8\sqrt{2}}{3\,\pi}\frac{1}{r_s}\right]\frac{k_e\,e^2}{2\,a_B}\ . \qquad (59)$$

The result for $d = 0$ recovers the conventional energy for a spin-unpolarised 2DEG located on the same 2D plane as the layer of the jellium background:

$$\epsilon(d = 0) = \left(\frac{1}{r_s^2} - \frac{8\sqrt{2}}{3\,\pi}\frac{1}{r_s}\right)\frac{k_e\,e^2}{2\,a_B}\ . \qquad (60)$$

The first term on the RHS of the expression in Eq.(60) represents the kinetic energy per particle, while the second term is the (exchange) potential energy per particle.

In Figure 2, we show the dependence of the energy per particle, $\epsilon(d)$ as a function of r_s for three values of the parameter, $d/a_B = 0$, 0.1 and 0.2. The energy per particle is given in units of $k_e\,e^2/(2\,a_B)$. One notes that as d/a_B increases, the overall energy per particle increases while the energy minimum shifts to larger r_s values. The expression in Eq. (59) suggests that the separation distance d affects more the high-density states (small r_s). For a given d/a_B, the energy at small r_s increases much more than the energy at larges r_s (for instance, consider the cases $r_s = 1.5$ and $r_s = 5$). We know that liquid electronic states are typically stable at high density (small r_s), while Wigner solid states stabilize at low density (large r_s). This means that the layer separation will affect the stability of the liquid states at high density by considerably increasing their energy and, thus, may make them energetically less competitive relative to a Wigner crystal state.

Another interesting finding concerns the new energy contribution, $\Delta\epsilon(d)$ in Eq.(57). From the outset, we expected this term to provide a positive correction to the total energy, thereby shifting the overall energy upward. This behaviour is indeed observed. What is more surprising, however, is the way this correction scales with the density parameter r_s. Rather than exhibiting a distinct density dependence, $\Delta\epsilon(d)$ is found to scale as $1/r_s^2$, precisely the same scaling as the kinetic energy per particle,

$t = \langle \hat{T} \rangle / N \propto 1/r_s^2$. Consequently, $\Delta\epsilon(d)$ effectively behaves like an additional kinetic energy contribution, despite originating from a different physical mechanism. This correspondence is not obvious a priori and suggests that the effect encoded in $\Delta\epsilon(d)$ modifies the energetic balance of the system in a manner closely analogous to the kinetic term.

6. CONCLUSIONS

In this work, we investigate a modified spin-unpolarised 2DEG model in which the 2D electron layer is suspended above and separated by an arbitrary distance from a neutralising 2D jellium background. Our study demonstrates that introducing such a finite separation generates an additional positive energy contribution. Remarkably, this contribution behaves as an effective kinetic energy term, leading to an overall increase in the system's total energy. This effect is particularly pronounced at high electron densities (small r_s) values, where kinetic energy naturally dominates the energetics of the system.

The results have important implications for the stability of 2DEG phases. Under normal conditions, high-density electron liquids are energetically favored over Wigner solid phases due to the dominance of kinetic energy and the suppression of long-range correlations. However, our findings indicate that the effective increase in kinetic energy caused by the electron–background layer separation may reduce the energetic advantage of the liquid state, potentially destabilizing it relative to the crystalline Wigner phase. This suggests that even modest geometric modifications, such as lifting the 2D electron layer above the neutralising background, can strongly influence the liquid-to-solid transition, possibly facilitating Wigner crystallization at densities where it would otherwise be suppressed.

These observations highlight the sensitivity of 2DEG systems to structural modifications and underscore the importance of considering geometric factors in both theoretical and experimental studies. While our calculations are based on a HF framework, which captures the leading-order kinetic and exchange effects, additional correlation effects, neglected in this work, could further modify the magnitude of the energy contributions and alter the detailed phase boundaries.

Looking forward, it would be highly valuable to extend this investigation using more sophisticated many-body wave functions, such as Jastrow-Slater or multi-determinant expansions, coupled with accurate quantum Monte Carlo techniques. Such studies could provide quantitative estimates of the separation-induced energy shifts and more precisely determine their impact on the energetic competition between liquid and Wigner solid phases. Furthermore, experimental realizations of 2DEG systems with tuneable electron-background separations which are potentially achievable in layered semiconductor heterostructures or van der Waals materials, could directly test the predictions of this work.

In summary, our study demonstrates that even a simple geometric modification to the conventional 2DEG model can induce nontrivial energetic effects. By introducing an effective kinetic contribution, the electron–background layer separation alters the energy landscape in a way that could influence phase stability, particularly favouring Wigner crystallization under conditions that were previously dominated by the electron liquid phase. These findings provide a foundation for future theoretical and experimental explorations, emphasizing the rich and tuneable physics of low-dimensional electron systems and the critical role of electron–background geometry in determining their collective behaviour.

ACKNOWLEDGMENTS

The research of O. Ciftja was supported in part by the U.S. National Science Foundation (NSF) Grant No. DMR-2001980.

Data accessibility (websites, platforms). The data are available from the author upon reasonable request.

Declaration of AI use. The author declares that no artificial intelligence (AI) tools were used in the writing of this manuscript.

Author Contributions. The author confirms sole responsibility for the conception and design of the study, data collection, analysis and interpretation of results, manuscript preparation, and final approval of the submitted version.

Conflict of interest declaration. The author declares no competing interests.

REFERENCES

Ashcroft NW, Mermin ND. 1976. Solid State Physics, Saunders College, Philadelphia.

Attaccalite C, Moroni S, Gori-Giorgi P, Bachelet GB. **2002**. Correlation energy and spin polarization in the 2D electron gas. *Physical Review Letters*, **88**, 256601 (2002). Erratum.; *Physical Review Letters*, **91**, 109902(E) (2003). DOI: https://doi.org/10.1103/PhysRevLett.88.256601.

Ceperley D. 1978. Ground state of the fermion one-component plasma: A Monte Carlo study in two and three dimensions. *Physical Review B*, **18**: 3126. DOI: https://doi.org/10.1103/PhysRevB.18.3126 .

Choudhury N, Ghosh KS. 1995. Density-functional theory of Wigner crystallization in two dimensions. *Physical Review*, **B 51**: 2588-2591. DOI: https://doi.org/10.1103/PhysRevB.51.2588.

Ciftja O, Batle J, Pons-Viver M. 2021. A two-dimensional electron gas suspended above a neutralising background. *Annals of Physics*,. (N.Y.) **429**, 168468. https://doi.org/10.1016/j.aop.2021.168468.

Ciftja O, Escamilla L, Mills R. **2015.** Shape-dependent energy of an elliptical jellium background, Adv. Condens. Matter Phys. **2015**, 851356. **https://doi.org/10.1155/2015/851356**.

Ciftja O, Wexler C. 2003. Monte Carlo simulation method for Laughlin-like states in a disk geometry. *Physical Review*, B **67**: 075304. https://doi.org/10.1103/PhysRevB.67.075304.

Ciftja O. 2015. Hartree-Fock energy of a finite two-dimensional electron gas system in a jellium background. *Physica B*, **458**: 92. 10.1016/j.physb.2014.11.019.

Ciftja O. **2021**. Deformation of the Fermi surface of a spinless two-dimensional electron gas in presence of an anisotropic Coulomb interaction potential. *Scientific Reports*, **11:** 3181 https://doi.org/10.1038/s41598-021-82564-y.

Crandall RS, Williams RW. 1971. Crystallization of electrons on the surface of liquid helium. *Physical Letters*, **A 34 (7):** 404. https://doi.org/10.1016/0375-9601(71)90938-8.

Farid B, Heine V, Engel GE, Robertson IJ. **1993**. Extremal properties of the Harris-Foulkes functional and an improved screening calculation for the electron gas. *Physical Review*, **B 48**: 11602. https://doi.org/10.1103/PhysRevB.48.11602.

Fetter AL, Walecka JD. **2003.** *Quantum theory of many-particle systems*. Dover Publications, Mineola, New York.

Gell-Mann M, Brueckner KA. **1957.** Correlation energy of an electron gas at high density. *Physical Review*, **106**: 364. DOI: https://doi.org/10.1103/PhysRev.106.364.

Giuliani GF, Vignale G. **2005**. Quantum theory of the electron liquid Cambridge University Press, Cambridge.

Harrell RH, Pyshkin KS, Simmons MY, Ritchie DA, Ford CJB, Jones GAC, Pepper M. **1999**. Fabrication of high-quality one- and two-dimensional electron gases in undoped GaAs/AlGaAs heterostructures. *Applied Physics Letters*, **74(16):2328-2330**. **DOI:10.1063/1.123840.**

Hasanuzzaman M, Islam SK, Tolbert L, Alam MT. 2004. Temperature dependency of MOSFET device characteristics in 4H- and 6H-Silicon Carbide (SiC). *Solid State Electronics*, **48 (**10–11): 1877-1881. https://doi.org/10.1016/j.sse.2004.05.029.

Isihara A, Ioriatti L. 1980. Exact evaluation of the second-order exchange energy of a two-dimensional electron fluid. *Physical Review B*, **22**: 214. DOI: https://doi.org/10.1103/PhysRevB.22.214

Kane BE, Pfeiffer LN, West KW, Harnett CK. 1993. Variable density high mobility two-dimensional electron and hole gases in a gated GaAs/$Al_xGa_{1-x}As$ heterostructure. *Applied Physics Letters*, **63:** 2132. https://doi.org/10.1063/1.110563.

Kwon Y, Ceperley DM, Martin RM. 1993. Effects of three-body and backflow correlations in the two-dimensional electron gas. *Physical Review B*, **48**: 12037. DOI: https://doi.org/10.1103/PhysRevB.48.12037 .

Lado F. 2003. Effective potentials in the integral quantum Hall effect. *Physical Review*, **B 67**: 245322. https://doi.org/10.1103/PhysRevB.67.245322 .

Li Y, Cooper JA, Capano MA. 2002. High-voltage (3kV) UMOSFETs in 4H-SiC. *IEEE Transactions on Electron Devices*, **49 (6):** 972-975. 10.1109/TED.2002.1003714.

Mak WY, Das Gupta K, Beere HE, Farrer I, Sfigakis F, Ritchie DA. 2010. Distinguishing impurity concentrations in GaAs and AlGaAs using very shallow undoped heterostructures. *Applied Physics Letters*, **97**: 242107. https://doi.org/10.1063/1.3522651.

Morf R, Halperin BI. 1986. Monte Carlo evaluation of trial wave functions for the fractional quantized Hall effect: Disk geometry.

Physical Review B **33**: 2221. https://doi.org/10.1103/PhysRevB.33.2221.

Pudalov VM, D'Iorio M, Campbell JW. 1994. Electron solid at zero magnetic field in a dilute 2D electron system in Si. *Physica B: Condensed Matter*, **1289:** 194 10.1016/0921-4526(94)90974-1.

Rajagopal AK, Kimball JC. 1977. Correlations in a two-dimensional electron system. *Physical Review B,* **15**: 2819. DOI: https://doi.org/10.1103/PhysRevB.15.2819

Shenoy JN, Cooper JA, Melloch MR. 1997. High-voltage double implanted power MOSFETs in 6H-SiC. *IEEE Electron Devices Letters*, **18**, 93. DOI:10.1109/55.556091.

Sim H-K, Tao R, Wu FY. 1986. Ground-state energy of charged quantum fluids in two dimensions. *Physical Review*, B **34**, 7123. DOI: https://doi.org/10.1103/PhysRevB.34.7123.

Slater JC. 1929. The theory of complex spectra. *Physical Review*, **34:** 1293. DOI: https://doi.org/10.1103/PhysRev.34.1293.

Sun J, Perdew JP, Seidl M. **2010**. Correlation energy of the uniform electron gas from an interpolation between high- and low-density limits. *Physical Review B,* **81**: 085123. Erratum *Physical Review B,* **98**: 079903 (2018). DOI: https://doi.org/10.1103/PhysRevB.81.085123.

Tanatar B, Ceperley DM. 1989. Ground state of the two-dimensional electron gas. *Physical Review B,* **39**: 5005. DOI: https://doi.org/10.1103/PhysRevB.39.5005

Zong FH, Lin C, Ceperley DM. 2002. Spin polarization of the low-density three-dimensional electron gas. *Physical Review E*, **66**: 036703. DOI: https://doi.org/10.1103/PhysRevE.66.036703 .

Ni–rGO NANO-SENSOR FOR PESTICIDE DETECTION IN FOOD SAMPLES

[1,2]Lueda KULLA, [1,2]Ana AMEDA, [1,2] Majlinda VASJARI

[1] Department of Chemistry, Faculty of Natural Sciences, University of Tirana, Albania

[2] Nano-Alb Unit, Academy of Sciences of Albania

Author for correspondence: kullalueda@gmail.com

LK, 0009-0007-4949-5517; **AA**, 0009-0003-2842-0066; **MV,** 0000-0003-2504-2138

ABSTRACT

The development of reliable strategies for the concurrent identification of structurally analogous pesticides remains a significant challenge in electrochemical sensing. This study presents a nickel nanoparticle-decorated reduced graphene oxide (Ni–rGO) laser-scribed electrode designed for the simultaneous determination of neonicotinoids, particularly imidacloprid (IMI) and thiamethoxam (THMX).The Ni–rGO composite demonstrated enhanced electrochemical performance through synergistic effects, leading to improved electron-transfer kinetics and elevated electrochemically performance, as confirmed by cyclic voltammetry and electrochemical impedance spectroscopy. Under optimized conditions, differential pulse voltammetry facilitated sensitive detection of the IMI–THMX mixture, showing a linear response with a sensitivity of 0.17 µA ppm-1 and a coefficient of determination(R^2) of 0.9925. The sensor exhibited a limit of detection (LoD) of 0.39 ppm and a limit of quantification (LoQ) of 1.18 ppm. High selectivity was confirmed in the presence of common inorganic ions and structurally similar compounds, with minimal signal variation (95–104%). Additionally, the sensor demonstrated good repeatability and reproducibility (RSD $\leq$ 6.7%) and retained stable performance over time. The applicability of the method was validated in real food samples, yielding satisfactory recovery and reliable detection in complex matrices. This work introduces an efficient electrochemical approach for the simultaneous determination of pesticides using a Ni–rGO platform, offering a simple, cost-effective and portable solution for rapid screening of neonicotinoid residues in food safety applications.

Keywords: Graphene oxide, nanoparticles, neonicotinoids, laser-scribed technology, portable nanosensor

Publisher: Academy of Sciences of Albania

Citation: Kulla L, Ana Ameda A, Vasjari M. 2026. Ni–rGO nano-sensor for pesticide detection in food samples. *Albanian Journal of Natural and Technical Sciences* (*AJNTS*), **31 (3):**65-83.
https://doi.org/10.67537/ajnts3103029
Classification: Research
Subject Category: applied sciences subject area: nanotechnology + analytical chemistry (electrochemistry / food safety)

1. INTRODUCTION

Neonicotinoids, a class of systemic insecticides with neurotoxic effects, are the fastest-growing and most widely used globally, accounting for 25% of the pesticide market in 2014 (Klingelhöfer *et al*. 2022). These insecticides are preferred due to their presumed lower toxicity to non-target organisms, humans, and the environment compared to older chemistries like organophosphates or carbamates, as well as their versatile application and systemic mode of action. However, concerns over their environmental and health impacts have risen due to their persistence in plant tissues. Studies have shown that neonicotinoids can accumulate in crops, potentially entering the food chain (Zhao *et al*. 2020). Human exposure occurs predominantly through dietary intake, water consumption, and inhalation of dust and pollen, posing potential risks to human health and non-target species (Chen *et al*. 2014; Zhang and Lu, 2022; Dasmodak *et al*. 2024).

Traditional techniques have been developed for detecting pesticides in environmental or food samples, offering excellent detection and precision, enabling simultaneous determination of similar structure pesticides. On the other hand, they are costly, time-consuming, require skilled personnel, and are unsuitable for on-site or real-time analysis (Liu *et al*. 2010; Farouk *et al*. 2016; Hou *et al*. 2019; Han *et al*. 2025).

To overcome the limitations of traditional methods, electrochemical techniques have emerged as effective solutions for pesticide detection. The electrochemical techniques provide advantages such as high sensitivity, low cost, rapid response times, and the ability for in situ and real-time monitoring. Their affordability, ease of use, good selectivity, and suitability for on-site analysis make them particularly well-suited for pesticide detection (Barton *et al*. 2024; Ding *et al*. 2024).

The performance of electrochemical analysis is strongly dependent on electrode design and surface modification. Recent advances in composite materials have significantly improved sensitivity, selectivity, and overall analytical performance. Carbon-based nanomaterials, such as graphene and carbon nanotubes (CNTs), are particularly attractive due to their high electrical conductivity, large surface area, and electrochemical stability. Their ability to promote rapid electron transfer and enhance adsorption and catalytic activity enables faster and more accurate detection compared to conventional electrodes, especially for pesticide analysis (Luo *et al*. 2022; Kulla et al. 2024; Almenhali *et al*. 2025; Repič *et al*. 2025; Tadawattana *et al*. 2025).

In parallel, fabrication techniques such as screen printing, laser-scribed electrodes, and inkjet printing have enabled the development of scalable, low-cost, and disposable sensors, supporting on-site applications in environmental and food monitoring (Hua *et al*. 2019; Johnson *et al*. 2021; Liang *et al*. 2022; Nalepa *et al*. 2025; Cui *et al*. 2025).

Graphene derivatives, such as graphene oxide (GO) and reduced graphene oxide (rGO), are widely used in electrochemical sensors due to their flexibility, hydrophilicity, and ability to form stable nanocomposites (Tadawattana *et al*. 2025; Kulla *et al*. 2026). Incorporating metal or metal oxide nanoparticles into rGOstructures, enhance catalytic activity and electron transfer, eliminating of rGO aggregation and reducingπ–π interactions (Liu and Lin, 2005; Yang and Cao, 2024; Piskin *et al*. 2025; Fernandes *et al*. 2025). Despite these advantages, rGO decorated with nanoparticle composites still face challenges in the simultaneous detection of structurally similar pesticides due to signal overlap (Urbanová *et al*. 2017; Wu *et al*. 2021; Kaewket and Ngamchuea, 2023). In particular, imidacloprid (IMI) and thiamethoxam (THMX) exhibit nearly identical electrochemical behaviour, undergoing irreversible nitro-group reduction between −0.8 and −1.3 V vs. Ag/AgCl, which results in overlapping cathodic peaks and complicates their simultaneous quantification, necessitating the development of more selective sensing strategies (Yue *et al*. 2020; Almenhali *et al*. 2025; Cardenas *et al*. 2025; Kulla *et al*. 2026). Nickel nanoparticles (NiNPs) integrated with rGO composite enhance electron transfer, conductivity, catalytic activity (Davar *et al*. 2009; Mohd Zaid and Idris, 2016; Samimi *et al*. 2024), dispersion, and structural stability due to synergistic interactions (Zhang *et al*. 2015; Mohd Zaid and Idris, 2016; Kulla *et al*. 2024; Kulla. 2026; *et al* Ameda *et al*. 2026).

An electrochemical strategy for the determination of neonicotinoids is proposed to address the limitations in simultaneously detecting structurally similar pesticides, enabling their combined quantification instead of individual discrimination (Kulla et al. 2026). In this study, group determination refers to the simultaneous electrochemical determination of neonicotinoid pesticides based on the reduction of their common electroactive nitro functional group. Since both analytes undergo a similar electrochemical reduction mechanism, they can be collectively determined through a single electrochemical response. Based on this platform, laser-scribed electrodes modified with Ni–rGO were applied for the detection of imidacloprid and thiamethoxam. To the best of our knowledge, this represents the first use of a Ni–rGO laser-scribed electrode for neonicotinoid detection, highlighting its potential for portable food monitoring.

2. MATERIALS AND METHODS

2.1. Chemicals and reagents

Pesticides (≥98.0%) were purchased from Sigma-Aldrich. Stock solutions of all pesticides were prepared in 0.1 mol/L phosphate-buffered saline (PBS) and stored at 4 °C. All other solutions were prepared using double-distilled water. $K_4Fe(CN)_6$ and $K_3Fe(CN)_6$ was obtained from Merck (KGaA, Darmstadt, Germany). Graphene oxide (10 mg/mL) and a 30 mM nickel (II) chloride solution were used for the preparation of the Ni-rGO sensing film. Silver and dielectric pastes were used for the fabrication of the screen-printed electrodes on PET substrates, while PVDF membranes (0.1 μm pore size, 47 mm diameter) were employed during the vacuum filtration step for film preparation.

2.2 Instrumentation and Experimental Setup

An XTOOL CO_2 laser plotter, was used for the laser reduction of the Ni-rGO film. The laser uses the software CorelDRAW for the pattern designs, which allow to design the desire pattern on the film during the reduction process. The film was fabricated filtrating Ni-rGO composite under a vacuum system after that the film was dried in thermostats and reduced using laser. Ater that the laser patterned of the electrode into the films were transferred into PET substrates using a hydraulic press.

Electrode fabrication was performed using screen printing for the electrode contact and laser technology, well-established techniques that allow for precise material deposition on the substrate.

Differential pulse voltammetry (DPV) measurements were conducted in 0.1M PBS pH 7, following the parameters: equilibration time of 10 s, step potential (E_step) of 0.01 V, pulse amplitude (E_pulse) of 0.05 V, pulse width (t_pulse) of 0.05 s, scan rate of 50 mV/s and the potential was swept from −0.3 to −1.4 V. Electrochemical characterization was performed in a 5 mM solution of $K_4[Fe(CN)_6]/K_3[Fe(CN)_6]$ 0.1 M KCl, using cyclic voltammetry (CV) and electrochemical impedance spectroscopy (EIS: frequency range of 100 kHz to 0.01 Hz , 10 mV sinusoidal AC signal amplitude).All electrochemical measurements were carried out using a potentiostat/galvanostat system (PalmSens, Netherlands).

2.3 *Sensor fabrication*

For the fabrication of theNi-rGO sensor, the GO dispersion and nickel (II) chloride solution were mixed and magnetically stirred for 15 min to obtain a homogeneous suspension. The resulting mixture was vacuum-filtered through a PVDF membrane to form a uniform GO/Ni^{2+} film, which was dried at 37 °C for 10 minutes. The film was then subjected to CO_2 laser irradiation to induce the co-reduction of GO and Ni^{2+} ions, resulting in the formation of the Ni-rGO nanocomposite. The film was transferred into a PET substrate using a hydraulic press under 11 tons for 2 minutes. The PET substrate served as the electrode platform. Silver conductors were incorporated before the film was transferred onto it using screen printing technology. The same procedure was employed for the preparation of Bi-rGO or Ag-rGO electrodes, where Bi^{2+} or Ag^{+} solutions were used in place of Ni^{2+} (Scroccarello *et al*. 2023). For comparison, a rGO film was prepared without the addition of the metal. The electrodes were subsequently used for pesticide detection (Figure 1). Figure 1 presents a schematic illustration of the sensor fabrication strategy, including laser-assisted preparation of the Ni-rGO sensing material and its integration into the electrochemical sensor for pesticide detection. It is intended as a conceptual representation of the fabrication procedure.

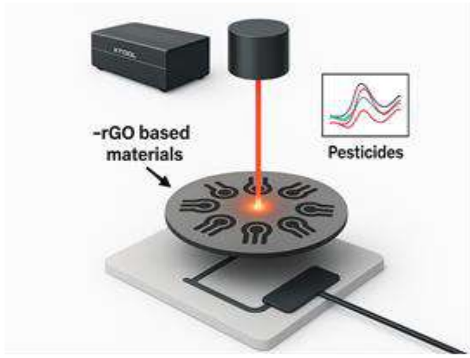

Fig. 1. Schematic illustration of the laser-assisted fabrication of the rGO-based electrochemical sensor for pesticide determination.

2.4 *Real sample analysis*

The Ni–rGOlaser-scribed sensor was validated in real food matrices using the standard addition method through spiking–recovery experiments. Mandarin and pepper samples were purchased from a random supermarket. The samples were washed with water and then squeezed. The extracted juice was filtered to remove impurities or any solid particles. All samples were diluted in a 1:1 (v/v) ratio with PBS, pH = 7, to ensure stable electrochemical conditions. The samples were spiked individually with varying concentrations of pesticides.

3. RESULTS AND DISCUSSION

3.1 Electrochemical characterization of rGO-based electrodes (CV and EIS)

The electrochemical behavior of rGO sensor and metal-decorated electrodes (Me–rGO, Me = Ni, Bi, Ag) was investigated by cyclic voltammetry (CV) and electrochemical impedance spectroscopy (EIS) using 5 mM $K_4[Fe(CN)_6]/K_3[Fe(CN)_6]$ in 0.1 M KCl. All electrodes exhibited well-defined redox peaks (Figure 2A). The rGO electrode showed a large peak-to-peak separation ($\Delta Ep = 0.543$ V), indicating slow electron-transfer kinetics, while modification significantly reduced ΔEp to 0.241 V (Ag–rGO), 0.166 V (Ni–rGO), and 0.121 V (Bi–rGO), reflecting improved charge-transfer properties due to synergistic effects between rGO and metal nanoparticles (Zhang *et al*. 2015; Trikkaliotis *et al*. 2021; Chen et al. 2022; Samimi *et al*. 2024; Ma *et al*. 2025; Kulla *et al*. 2026). The Ia/Ic ratio (0.93–0.98) confirmed a quasi-reversible process for all electrodes. EIS results (Figure 2B) supported these findings. The Nyquist plots were fitted using a Randles equivalent circuit (Figure 3) comprising solution resistance (Rs), charge-transfer resistance (Rct), double-layer capacitance (Cdl), and Warburg impedance (W) (Magar *et al*. 2021; Nalepa *et al*. 2025; Kulla *et al*. 2026). The charge-transfer resistance (Rct) decreased from 419.6 Ω (rGO) to 270.5 Ω (Ag–rGO) and 143.3 Ω (Ni–rGO), indicating faster electron transfer. In contrast, Bi–rGO exhibited a higher Rct value (1910 Ω), suggesting less favourable charge-transfer behaviour despite its low ΔEp. The double-layer capacitance (Cdl), reflecting charge storage at the electrode/electrolyte interface, increased markedly from 0.054 µF (rGO) to 100.2 µF (Ni–rGO), indicating a substantial increase in electrochemically active sites.

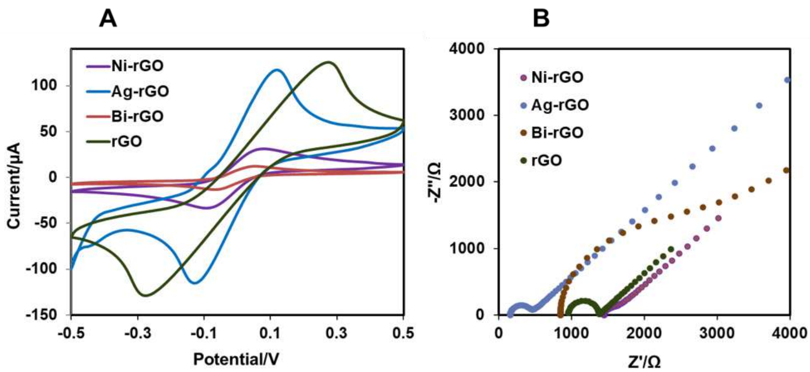

Fig. 2: (A) Cyclic voltammograms recorded at 50 mV s^{-1} for rGO (green), Bi–rGO (red), Ag–rGO (blue), and Ni–rGO (purple) electrodes. (B) Nyquist plots showing the EIS responses of the corresponding electrodes. All measurements were performed in 5 mM $[Fe(CN)_6]^{4-}/[Fe(CN)_6]^{3-}$ in 0.1 M KCl.

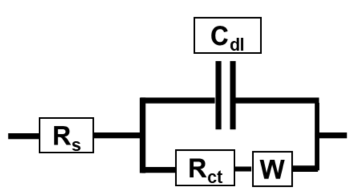

Fig. 3: The Randles equivalent circuit.

The electrochemically active surface area (ESCA) was calculated using a specific capacitance of 40 µF cm^{-2} (Eq. 1) (Magar *et al*. 2021; Martínez-Hincapié *et al*. 2024). Accordingly, the ESCA increased from 0.00135 cm² (rGO) to 2.505 cm² (Ni–rGO), confirming the significant enhancement in active surface area upon Ni modification. This increase in ESCA is consistent with the observed decrease in Rct and ΔEp, demonstrating that the improved electrochemical performance of Ni–rGO originates from the combined effects of increased surface area and enhanced electron-transfer kinetics. A summary of the electrochemical parameters is provided in Table 1.

$$\boldsymbol{ESCA = \frac{Cdl}{Cs}} \quad (1)$$

Table 1. Electrochemical parameters of laser-scribed electrodes

Electrode	ΔEp (V)	Rct (Ω)	Cdl (μF)	Ia/Ic
Ni-rGO	0.166	143.3	100.2	0.97
Ag-rGO	0.241	270.5	1.069	0.96
Bi-rGO	0.121	1910	9.16	0.93
rGO	0.543	419.6	0.054	0.98

3.2 *Electrochemical behaviour of neonicotinoids at graphene-based sensor*

The electrochemical behaviour of IMI and THMX was studied by differential pulse voltammetry (DPV) using rGO, Ag–rGO, Bi–rGO, and Ni–rGO electrodes. The reduction of nitro-functionalized neonicotinoids is governed by proton-coupled electron transfer processes and is therefore highly sensitive to the solution pH, as reported in previous studies (Kulla *et al*. 2024; Kulla *et al*. 2026). Accordingly, phosphate-buffered saline (PBS, pH 7.0) and optimized DPV parameters were selected based on literature precedents to ensure stable and comparable electrochemical responses.

The responses obtained for the IMI–THMX mixture (10 ppm) reveal clear differences in electrode performance, consistent with the trends observed in CV and EIS characterization. The corresponding differential pulse voltammograms are presented in Figure 4. While no significant faradaic signals were detected in the PBS blank, the modified electrodes exhibited distinct cathodic peaks associated with nitro-group reduction. The appearance of multiple peaks in the DPV curves is attributed to the stepwise electrochemical reduction of the nitro group and the formation of intermediate species during the reduction process. The last reduction peak was selected for quantification because it provided the highest current response, the best repeatability, and the most reliable analytical signal. This peak also showed the lowest background interference, making it the most suitable for analytical quantification. The Ni–rGO electrode showed the highest current response (~−32 µA at ~−0.95 V), followed by Ag–rGO (~−30 µA at ~−0.90 V), whereas Bi–rGO displayed a weaker signal (~−15 µA at ~−1.05 V). In contrast, the bare rGO electrode produced a poorly defined response, indicating limited electrocatalytic activity.

The enhanced performance of Ni–rGO agrees with its lower charge-transfer resistance and higher electrochemically active surface area determined from EIS analysis, confirming that the incorporation of Ni nanoparticles promotes faster electron-transfer kinetics and increases the density of active sites. This results in reduced overpotential and improved sensitivity toward nitro-group reduction, highlighting the effectiveness of the Ni–rGO platform for neonicotinoid detection (Sassykova *et al*. 2021; Singh *et al*. 2025).

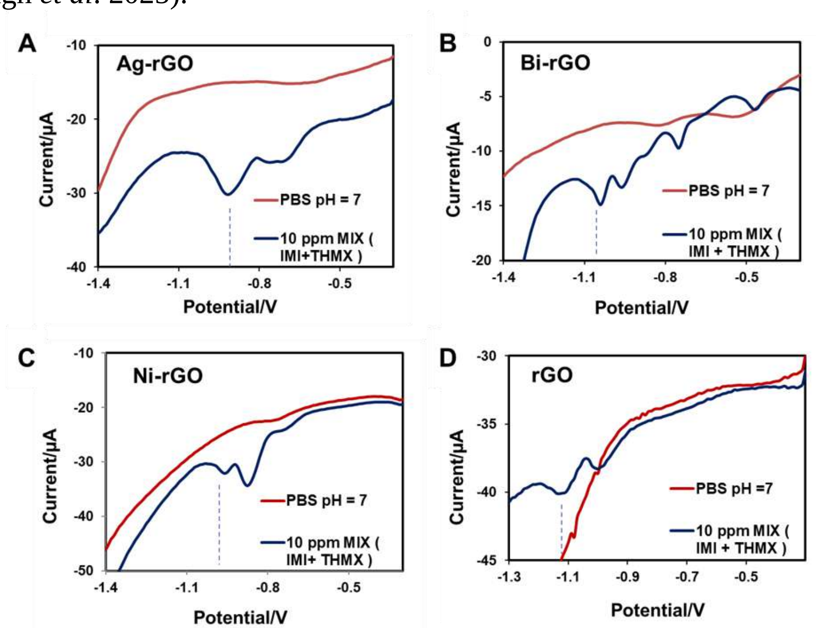

Fig.4: Differential pulse voltammograms (DPVs) of a 10-ppm mixture of imidacloprid (IMI) and thiamethoxam (THMX) recorded in PBS (pH 7.0) using (A) Ag–rGO, (B) Bi–rGO, (C) Ni–rGO, and (D) rGO electrodes. The blue curves

correspond to measurements in the pesticide mixture, while the red curves represent the PBS blank.

Repeatability, evaluated as relative standard deviation (RSD, Figure 5), showed low variability for rGO, Ni–rGO, and Bi–rGO electrodes (≤ 2–3%), whereas Ag–rGO exhibited comparatively higher values (≤ 6%). Although similar precision was observed for rGO-, Ni-, and Bi-based electrodes, the selection of Ni–rGO is justified by its overall superior electrochemical performance, including higher current response, lower charge-transfer resistance, and larger electrochemically active surface area. This combination of sensitivity and stability highlights Ni–rGO as the most suitable platform for subsequent analytical applications.

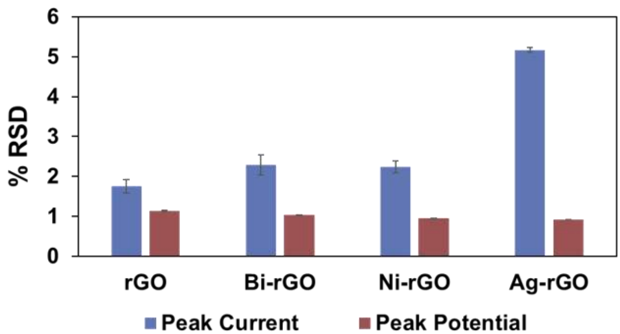

Fig.5: Repeatability of the sensors expressed as relative standard deviation (RSD, %).

3.3 Electrochemical detection of IMI and THMX using DPV

Figure 6 shows the DPV responses recorded under optimized conditions for the IMI–THMX mixture. As illustrated in Figure 6A, the peak current increases progressively with increasing pesticide concentration. The corresponding calibration plot (Figure 6B) exhibits a linear relationship between peak current and concentration, with an intercept of −0.23, a sensitivity of 0.17 µA ppm-1, and a coefficient of determination(R^2) of 0.9925. The limit of detection (LoD) and limit of quantification (LoQ) were worked out using the following equations:

$$\text{"LoD"}=3.3(s/S) \; ; \; \text{"LoQ"}=10(s/S)$$

where s is the standard deviation of the blank and S is the slope of the calibration curve (Kulla et al. 2026). The obtained LoD and LoQ values were 0.39 ppm and 1.18 ppm, respectively.

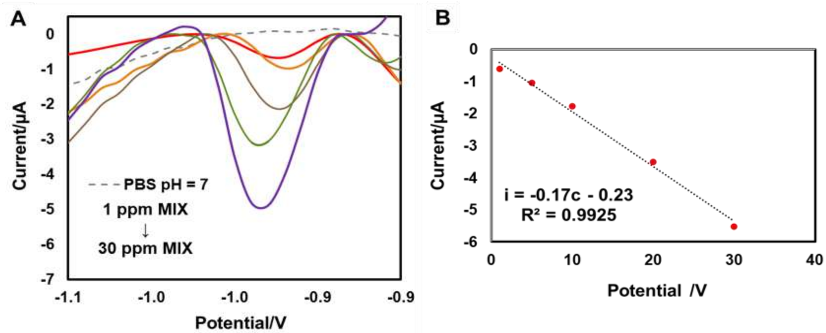

Fig.6: DPV responses and calibration for the IMI–THMX mixture using the Ni–rGO electrode. (A) DPV voltammograms at increasing concentrations; (B) corresponding calibration plot. DPV parameters: E_step = 0.01 V, E_pulse = 0.05 V, t_pulse = 0.05 s, scan rate = 50 mV s-1 (n = 3).

3.4. Selectivity and interference study

The selectivity of the developed sensor was evaluated by investigating the effect of potential interfering species under optimized conditions. As shown in Figure 7, the presence of common inorganic ions (Na^+, K^+, Ca^{2+}, Mg^{2+}, Cl^-) and other pesticides such as HCB did not significantly affect the DPV response of a 30-ppm IMI–THMX mixture. These species caused only minor variations in the peak current (97–104% of the initial signal), indicating negligible interference.

In addition, inorganic nitrogen species (NO^{2-}, NO^{3-}), were analysed, showing relative responses of 95–98% compared to the initial signal. This confirms the high selectivity of the sensor toward neonicotinoids, even in the presence of structurally related nitro-containing compounds. The relative current response in all cases was calculated as (I_i/I_0) × 100%.

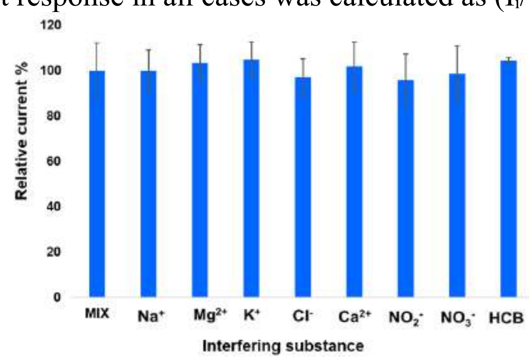

Fig.7: Relative current response of the Ni-rGO laser electrode in 30 ppm IMI and THMX mixture, under the influence of various affecting substances.

3.5 Repeatability, reproducibility and stability of the Ni–rGO sensor

The repeatability, reproducibility, and stability of the developed Ni–rGO sensor for IMI–THMX detection were evaluated. Repeatability was assessed through five successive measurements of a 30-ppm standard solution, while reproducibility was evaluated using three independently prepared electrodes. Relative standard deviation (RSD) values of ≤ 6.7% were obtained in both tests, confirming the sensor's consistent and reliable performance. The storage stability of the sensor was further examined, showing that after one week under laboratory conditions, the sensor retained 108.6% of its initial response, demonstrating good stability and robustness.

3.6 *Sensor performance under matrix effects*

The practical utility of the sensor for group detection was assessed using a binary mixture of imidacloprid (IMI) and thiamethoxam (THMX). Measurements performed in undiluted extracts exhibited unstable baseline currents therefore, dilution (1:1, v/v) with PBS was employed to optimize sample heterogeneity and reproducibility.

Known concentrations of the IMI–THMX mixture (3, 5, and 10 ppm) were spiked into the sample's matrix to assess the recovery. The limit of detection (LoD) for the mixed system was 0.39 ppm. In pepper matrices, recoveries ranged from 75.4% to 96.7%, with relative standard deviation (RSD) values between 7.1% and 8.1%, indicating acceptable precision under relatively complex conditions. In mandarin, recoveries ranged from 71.7% to 100.7%, with RSD values between 9.7% and 12.3%. The comparatively higher variability observed in mandarin suggests a stronger contribution of matrix components, likely affecting both signal stability and analyte response in the mixed system.

Notably, the detectable signal in non-spiked samples, particularly in mandarin (≈LoD), indicates the presence of background electrochemical contributions, which can influence both recovery and precision. This effect is consistent with the broader recovery range and elevated RSD values observed in this matrix, reflecting matrix-induced signal variability.

Furthermore, high linearity was obtained using the standard addition method ($R^2 > 0.9809$), confirming reliable quantification in complex matrices.

Overall, the results summarized in Table 2 demonstrate the accuracy, reproducibility, and robustness of the proposed sensor in real food samples. Notably, its capability for simultaneous group detection of neonicotinoids highlights strong potential for rapid on-site food safety monitoring.

Table 2. Quantification of neonicotinoids (IMI + THMX) in spiked food samples using Ni–rGO laser-scribed

Sample	Added (ppm)	Found (ppm)	Recovery (%)	RSD (%)
Pepper	0	<LoD (0.18)	–	–
	3	2.3	75.4	8.1
	5	4.8	95.9	7.7
	10	9.7	96.7	7.1
Mandarin	0	0.4	–	–
	3	2.2	71.7	12.3
	5	5.4	107.6	11.0
	10	10.1	100.7	9.7

4. CONCLUSIONS

In this work, a Ni-rGO laser-scribed electrochemical sensor was successfully developed for the simultaneous detection of neonicotinoid IMI and THMX pesticides in food samples. The incorporation of nickel nanoparticles significantly enhanced the electrochemical performance of the sensor, resulting in faster electron-transfer kinetics, lower charge-transfer resistance, and increased active surface area, as confirmed by CV and EIS. The proposed sensor demonstrated good sensitivity, linearity, and low detection limits (LoD 0.39 ppm), along with excellent selectivity. Further experiments confirm the good repeatability, reproducibility (RSD $\leq$ 6.7%) and storage stability (108.6% of its initial response). The proposed electrochemical strategy presented here provides a practical alternative for the determination of structurally similar pesticides while maintaining analytical accuracy.

Overall, the developed Ni–rGO platform represents a promising option for portable and on-site monitoring of pesticide residues, with potential for further integration into rapid screening technologies for food safety.

Ethics Approval. Not applicable. This study does not involve human participants, animals, or sensitive personal data. The research is based entirely on the analysis of publicly available satellite imagery and open-source data.

Data Sharing Statement. The datasets generated and analysed during the current study (including the processed Google Earth imagery and software scripts) are available from the corresponding author upon reasonable request.

Authors' Contributions. L.K.: Writing- original draft, conceptualization, visualization, methodology, software, investigation, formal analysis and data curation, **A.A.:** Investigation, formal analysis, data curation, software and writing – review &editing, **M.V.:** Conceptualization, validation, visualization, writing – review &editing, project administration and supervision.

All authors have read and agreed to the published version of the manuscript.

AI Statement. The authors declare that no AI-assisted technologies were used in the generation of the data analysis, or image processing.

Declaration of Interest. The authors declare that they have no competing financial interests.

Funding. This research received no specific grant from any funding agency in the public, commercial, or not-for-profit sectors.

AKNOWLEDGEMENT

L. Kulla and A. Ameda contributed equally to this work. This work was supported by the project "Nano-Biosensors for Pesticide Residues in Agriculture/Food Industry" funded by the Academy of Sciences of Albania. The authors also sincerely acknowledge the Department of Chemistry, Faculty of Natural Sciences, University of Tirana, for their support and contributions.

REFERENCES

Almenhali Z, Kanagavalli P, Abd-Ellah M. 2025. Reduced graphene oxide-based electrochemical aptasensor for multiplexed detection of imidacloprid, thiamethoxam, and clothianidin in food samples. *Scientific Reports*, **15**: 10329. DOI: 10.1038/s41598-025-94313-6.

Ameda A, Kulla L, Shehu A, Baraj B, Cenolli S, Broli N, Vasjari M. 2026. A new rGO@Ni nanocomposite for simultaneous detection of Pb(II) and Cd(II). *Sensing and Bio-Sensing Research,* **51**: 100951. DOI: 10.1016/j.sbsr.2026.100951.

Barton B, Ullah N, Koszelska K. 2024. Reviewing neonicotinoid detection with electroanalytical methods. *Environmental Science and Pollution Research,* **31:** 37923–37942. DOI: 10.1007/s11356-024-33676-1.

Cardenas MA, Vignati M, Pierini GD, Robledo SN, Moressi MB, D'Eramo F. 2025. Chemometric-assisted electrochemical sensor for simultaneous determination of neonicotinoids imidacloprid and thiamethoxam in honey samples. *Analytical Methods,* **17 (13):** 2686–2696. DOI: 10.1039/d4ay02247e.

Chen C-T, Fan W-S, Chiang K-H, Wu C-Y. 2022. Bismuth and nitrogen co-doped graphene oxide for efficient electrochemical sensing of Pb(II) by synergistic dual-site interaction. *Journal of Solid State Electrochemistry*, **26:** 3475–3485. DOI: 10.1007/s10008-022-05277-w.

Chen M, Tao L, McLean J, Lu C. 2014. Quantitative analysis of neonicotinoid insecticide residues in foods: implication for dietary exposures. *Journal of Agricultural and Food Chemistry,* **62**: 6082–6090. DOI: 10.1021/jf501397m.

Cui X, Gu T, Ma K, Zeng J, Xia H. 2025. Laser-induced graphene electrochemical sensors: an emerging platform for Agri-Food and Environmental Detection. *Chemosensors,* **13:** 432. DOI: 10.3390/chemosensors13120432.

Dasmodak S, Paramanik S, Mukherjee S, Paramanik M. 2024. Food chain contamination by neonicotinoids—A matter of concern. In: *Neonicotinoids in the Environment*. Springer, 9. DOI: 10.1007/978-3-031-45343-4_9 .

Davar F, Fereshteh Z, Salavati-Niasari M. 2009. Nanoparticles Ni and NiO: synthesis, characterization and magnetic properties. *Journal of Alloys and Compounds,* **476:** 797–801. DOI: 10.1016/j.jallcom.2008.09.121.

Ding L, Guo J, Chen S, Wang Y. 2024. Electrochemical sensing mechanisms of neonicotinoid pesticides and recent progress in utilizing functional materials for electrochemical detection platforms. *Talanta,* 273: 125937. DOI: 10.1016/j.talanta.2024.125937.

Farouk M, Abd El Aziz Hussein L, Fathy El Azab N. 2016. Simultaneous determination of three neonicotinoid insecticide residues and their metabolite in cucumbers and soil by QuEChERS clean up and liquid chromatography with diode-array detection. *Analytical Methods*, **8:** 4563–4575. DOI: 10.1039/c6ay01161f.

Fernandes JO, Bernardino CAR, Marques MCDC, de Souza OPL, Mahler CF, Braz BF, Santelli RE, Canevari TC, Cincotto FH. 2025. A highly sensitive disposable electrochemical sensor based on copper nanoparticles for pesticide imidacloprid determination in contaminated water sources. *Environmental Science: Water Research & Technology*, **11:** 1517–1526. DOI: 10.1039/d4ew00829d.

Han Y, Tian Y, Li Q, Yao T, Yao J, Zhang Z, Wu L. 2025. Advances in detection technologies for pesticide residues and heavy metals in rice A Comprehensive Review of Spectroscopy, Chromatography, and Biosensors. *Foods*, **14:** 1070. DOI: 10.3390/foods14061070.

Hou J, Xie W, Hong D, Zhang W, Li F, Qian Y, Han C. 2019. Simultaneous determination of ten neonicotinoid insecticides and two metabolites in honey and royal jelly by solid-phase extraction and liquid chromatography-tandem mass spectrometry. *Food Chemistry*, **270:** 204–213. DOI: 10.1016/j.foodchem.2018.07.068.

Hua QT, Ruecha N, Hiruta Y, Citterio D. 2019. Disposable electrochemical biosensor based on surface-modified screen-printed electrodes for organophosphorus pesticide analysis. *Analytical Methods*, **11:** 3439–3445. DOI: 10.1039/c9ay00852g.

Johnson ZT, Williams K, Chen B, Sheets R, Jared N, Li J, Smith EA, Claussen JC. 2021. Electrochemical sensing of neonicotinoids using laser-induced graphene. *ACS Sensors* **6**: 3063–3071. DOI: 10.1021/acssensors.1c01082.

Kaewket K, Ngamchuea K. 2023. Microporous carbon for electrochemical detection of imidacloprid insecticide in fruit and water samples. *RSC Advances*, **13:** 4532–4541. DOI: 10.1039/d3ra00192j.

Klingelhöfer D, Braun M, Brüggmann D, Groneberg DA. 2022. Neonicotinoids: A critical assessment of the global research landscape of the most extensively used insecticide. *Environmental Research*, **213:** 113727. DOI: 10.1016/j.envres.2022.113727.

Kulla L, Ameda A, Jakubec P, Baraj B, Shehu A, Cenolli S, Broli N, Vasjari M. 2026. Factorial design–assisted simultaneous electrochemical sensing of neonicotinoid pesticides using a Ni-rGO-modified electrode. *Sensing and Bio-Sensing Research,* **51:** 100992. DOI: 10.1016/j.sbsr.2026.100992.

Kulla L, Ameda A, Vasjari M. 2024. A rapid electrochemical platform for detecting thiamethoxam using a Ni-rGO carbon paste composite. *Journal of Natural Sciences,* **36:** 95–115. DOI: 10.70827/1224arepft.

Liang G, He Z, Zhen J, Tian H, Ai L, Pan L, Gong W. 2022. Development of screen-printed electrodes for pesticide detection. *Environmental Technology & Innovation*, **28:** 102922. DOI: 10.1016/j.eti.2022.102922

Liu G, Lin Y. 2005. Electrochemical sensor for organophosphate pesticides and nerve agents using zirconia nanoparticles as selective sorbents. *Analytical Chemistry,* **77:** 5894–5901. DOI: 10.1021/ac050791t.

Liu S, Zheng Z, Wei F, Ren Y, Gui W, Wu H, Zhu G. 2010. Simultaneous determination of seven neonicotinoid pesticide residues in food by ultraperformance liquid chromatography tandem mass spectrometry. *Journal of Agricultural and Food Chemistry*, **58:** 3271–3278. DOI: 10.1021/jf904045j.

Luo J, Li S, Wu Y, Pang C, Ma X, Wang M, Zhang C, Zhi X, Li B. 2022. Electrochemical sensor for imidacloprid detection based on graphene oxide/gold nanoparticles. *Microchemical Journal* 183, 107979. DOI: 10.1016/j.microc.2022.107979.

Ma G, An Z, Yang Y, Wang W, Wang Y, Tian S, Gao J, Gong X-Z, Belfiore LA, Tang J. 2025. Synergistic regulation of Ag nanoparticles and reduced graphene oxide. n Boosting TiO_2 Microspheres Photocatalysis for Wastewater Treatment. *Nanomaterials,* **15:** 1510. DOI: 10.3390/nano15191510.

Magar HS, Hassan RYA, Mulchandani A. 2021. Electrochemical impedance spectroscopy: principles, construction, and biosensing applications. *Sensors,* **21**: 6578. DOI: 10.3390/s21196578.

Martínez-Hincapié R, Wegner J, Anwar MU, Raza-Khan A, Franzka S, Kleszczynski S, Čolić V. 2024. The determination of the electrochemically active surface area and its effects electrocatalytic properties of structured nickel electrodes produced by additive manufacturing. *Electrochimica Acta*, **476**: 143663. DOI: 10.1016/j.electacta.2023.143663.

Mohd Zaid N, Idris N. 2016. Enhanced capacitance of hybrid layered graphene/nickel nanocomposite for Supercapacitors. *Scientific Reports*, **6**: 32082. DOI: 10.1038/srep32082.

Nalepa M-A, Kulla L, Jakubec P, Hrubý V, Panáček D, Dědek I, Vasjari M, Otyepka M. 2025. Scalable fabrication of electrochemical sensors via inkjet printing of functionalized graphene for pesticide detection. *Advanced Materials Technologies*, **11**: e01765. DOI: 10.1002/admt.202501765.

Piskin E, Alakus Z, Budak F, Cetinkaya A, Ozkan SA. 2025. Nanoparticle-supported electrochemical sensors for pesticide analysis in fruit juices. *Journal of Pharmaceutical and Biomedical Analysis Open* **5**, 100056. DOI: 10.1016/j.jpbao.2025.100056.

Repič B, Marolt G, Kuscer D. 2025. Carbon-based thick films for electrochemical detection of neonicotinoid insecticides. *Journal of Electroanalytical Chemistry* **984**: 119054. DOI: 10.1016/j.jelechem.2025.119054.

Samimi G, Ashrafi H, Tashkhourian J, Haghighi B. 2024. rGO@Ni/NiO composite as an effective electrocatalyst for methanol oxidation reaction in alkaline media. *Journal of Physics and Chemistry of Solids,* **184**: 111724. DOI: 10.1016/j.jpcs.2023.111724.

Sassykova L, Kubekova AR, Batyrbayeva ShN, Azhigulova A, Zhaxibayeva R, Kozhaisakova ZhM, Zhusupova M. 2021. Hydrogenation of aromatic nitro compounds to amines on nickel and iron-containing catalysts. *Rasayan Journal of Chemistry* **14**: 1223–1229. DOI: 10.31788/RJC.2021.1426124.

Scroccarello A, Álvarez-Diduk R, Della Pelle F, de Carvalho Castro e Silva C, Idili A, Parolo C, Compagnone D, Merkoçi A. 2023. One-step laser nano structuration of reduced graphene oxide films embedding metal nanoparticle for sensing applications. *ACS Sensors* **8**: 598–609. DOI: 10.1021/acssensors.2c01782.

Singh A, Khurana M, Mishra A, Pani B, Awasthi SK. 2025. Nickel-Guanidine Functionalized Graphene Oxide as a Heterogeneous Catalyst for the Reduction of Nitro Compounds to Amines at Room Temperature. *Chemistry Select*, **10**: e01357. DOI: 10.1002/slct.202501357.

Tadawattana P, Kawashima K, Sittiwanichai S, T-Thienprasert J, Mori T, Pongprayoon P. 2025. Exploring the capabilities of nanosized graphene oxide as a pesticide nanosorbent: Simulation

Studies. *ACS Omega* **10**: 8951–8959. DOI: 10.1021/acsomega.4c06036.

Trikkaliotis DG, Christoforidis AK, Mitropoulos AC, Kyzas GZ. 2021. Graphene oxide synthesis, properties and characterization techniques: A comprehensive review. *ChemEngineering,* **5:** 64. DOI: 10.3390/chemengineering5030064.

Urbanová V, Bakandritsos A, Jakubec P, Szambó T, Zbořil R. 2017. A facile graphene oxide-based sensor for electrochemical detection of neonicotinoids. *Biosensors and Bioelectronics,* **89**: 532–537. DOI: 10.1039/d4ew00829d

Wu Y, Li Z, Han D, Duan Q, Wang F. 2021. A robust electrochemical sensor for determination of thiamethoxam based on electrochemical reduced graphene oxide-cationic pillar[6]arene composite film. *Journal of The Electrochemical Society* **168: 126506. DOI:** 10.1149/1945-7111/ac3abd**.**

Yang Z, Cao L. 2024. Electrochemical sensor based on silver nanoparticles/carboxylated multi-walled carbon nanotubes modified glassy carbon electrode for detection of carbamate pesticide in food. *Food Measurement and Characterization* **18**: 6225–6236. DOI: 10.1007/s11694-024-02642-3.

Yue X, Li Z, Zhao S. 2020. A new electrochemical sensor for simultaneous detection of sulfamethoxazole and trimethoprim antibiotics based on graphene and ZnO nanorods modified glassy carbon electrode. *Microchemical Journal* **159**: 105440. DOI: 10.1016/j.microc.2020.105440.

Zhang D, Lu S. 2022. Human exposure to neonicotinoids and the associated health risks: a review. *Environment International,* 163: 107201. DOI: 10.1016/j.envint.2022.107201.

Zhang W, Li Y, Zeng X. 2015. Synergetic effect of nickel and graphene for enhanced photocatalytic hydrogen evolution via dye sensitization. *Scientific Reports* **5**: 10589. DOI: 10.1038/srep10589.

Zhao Y, Yang J, Ren J, Hou Y, Han Z, Xiao J, Li Y. 2020. Exposure level of neonicotinoid insecticides in the food chain and the evaluation of their human health impact and environmental risk: an overview. *Sustainability,* **12:** 7523. DOI: 10.3390/su12187523.

CONSERVATION STATUS AND PRODUCTION CHARACTERISTICS OF INDIGENOUS SHEEP BREEDS IN KOSOVA: IMPLICATIONS FOR GENETIC RESOURCE CONSERVATION

Hysen BYTYQI [1], Hajrip MEHMETI [2], Alltane KRYEZIU [3], Xhavit RAMADANI [4], Fatos KRASNIQI [5]

[1,2,3,5]Department of Animal Science, Faculty of Agriculture and Veterinary, University of Prishtina, Kosova

[4] Department of Technology and Biotechnology, Faculty of Agriculture and Veterinary, University of Prishtina, Kosova

Author for correspondence: fatos.krasniqi@uni-pr.edu

HB, 0000-0001-7352-695X; HM, 0000-0002-8851-123X; AK, 0000-0002-0968-3990; XhR, 0000-0001-5104-0908; FK, 0009-0004-9570-0081

ABSTRACT

This study evaluated the conservation status, phenotypic, morphometric, productive, reproductive, and demographic performances of four indigenous sheep breeds in Kosova-Balusha (BAL), Kosova (KOS), Bardhoka (BAR), and Sharri (SHA) -following FAO guidelines. Data were collected in 2025 through a cross-sectional survey across 20 farms. The results revealed significant breed-related variations. SHA sheep exhibited the highest reproductive efficiency, with 92–96% fertility and 90–95% lamb survival rates, demonstrating strong adaptation to mountainous systems. BAR sheep produced the highest milk yield (138.4 ± 6.4kg/lactation) under lowland semi-intensive conditions. BAL sheep showed moderate performance and good adaptation to extensive mountain grazing. In contrast, KOS sheep displayed the lowest morphometric values, milk production (84.2 ± 4.9kg/lactation), fertility (82–88%), and lamb survival, indicating high vulnerability. Population risk assessments classified SHA and BAR as ”not at risk”, while BAL was” endangered” and KOS was ”critically endangered”. These findings underscore high regional genetic variability and highlight the urgent need for targeted *in situ* and *ex situ* conservation programs, particularly for the BAL and KOS breeds.

***Keywords*:** Indigenous sheep breeds; morphometric examination; productivity; reproductive performance; genetic conservation

Publisher: Academy of Sciences of Albania

Citation: Bytyqi H, Mehmeti H, Kryeziu A, Ramadani Xh, Krasniqi F. 2026. Conservation status and production characteristics of indigenous sheep breeds in Kosova: Implications for genetic resource conservation. *Albanian Journal of Natural and Technical Sciences* (AJNTS), **31 (3):**85-108.
https://doi.org/10.67537/ajnts3103030
Classification: Research
Subject Category: life sciences subject area: agricultural sciences subject area + veterinary sciences+ animal sciences

1. INTRODUCTION

Genetic resources of livestock constitute a vital element of agricultural biodiversity worldwide, providing essential support for maintaining sustainable food production systems. Resulting from centuries of natural and artificial selection processes, indigenous livestock breeds have acquired unique adaptive features that allow them to cope with challenging environmental conditions. These adaptive traits include resistance to climatic stress, tolerance to endemic diseases, the ability to utilize low-quality feedstuffs, and sustained productivity under extensive husbandry practices (Ajmone-Marsan *et al*. 2010; FAO, 2011; Dagnew *et al*. 2017). Given the emerging challenges associated with climate change, environmental volatility, and increasing pressure on the agricultural sector, the protection and sustainable management of native animal breeds has become a critical issue from both scientific and socio-economic perspectives (Tesema *et al*. 2024).

Sheep were the earliest domesticated livestock species, originating approximately 10,000 years ago in the Near East (Notter, 1999). Following domestication, sheep spread widely throughout Europe, diversifying into numerous distinct breeds through evolution and adaptation to local agro-environmental conditions and production systems (Handley *et al*. 2007; Gandini *et al*. 2007). The Balkan Peninsula represents a crucial geographic hub in the history of European sheep diversification. Owing to its diverse landscape and rich pastoral heritage, the region preserves a wide array of sheep breeds characterized by unique phenotypic and productive traits (Cinkulov *et al*. 2008).

Kosova serves as a compelling example of this Balkan livestock tradition (Bytyqi *et al*. 2014). The country features diverse agro-climatic conditions, ranging from fertile lowlands to hilly and mountainous grazing regions. Natural pastures and meadows occupy a significant share of agricultural land, providing a robust forage base for local ruminants (Bytyqi *et al*. 2015; Kosova Agency of Statistics, 2024). Under these conditions, sheep husbandry remains a primary agricultural occupation. Four indigenous sheep breeds are currently recognized in Kosova: Bardhoka (BAR), Balusha (BAL), Sharri (SHA), and Kosova (KOS) (Bytyqi *et al*. 2014; Bytyqi *et al*. 2015). These breeds belong predominantly to the long-tailed, coarse-wooled Pramenka group, traditionally raised under extensive or semi-intensive production systems. Historically utilized as multi-purpose animals for milk, meat, and wool, recent decades have seen a shift toward milk and lamb production due to the declining economic value of wool. Consequently, enhancing productive and reproductive performance traits has become central to local breeding strategies (Silveira Cougo *et al*. 2024).

Among these indigenous resources, the BAL sheep represents one of Kosova's most distinctive and culturally valuable genetic assets. This breed is characterized by a unique coat pigmentation pattern featuring a black head and neck coupled with a white body fleece. Beyond its distinct morphology, molecular research indicates that the BAL breed exhibits low heterozygosity and a small effective population size, placing it at a high risk of genetic erosion and inbreeding (Bytyqi et al., 2015). Similarly, the KOS sheep breed has faced a drastic population decline, surviving only in isolated flocks managed with traditional pastoral techniques. Furthermore, all native sheep breeds in Kosova exhibit genetic vulnerability due to the absence of systematic conservation frameworks and structured breeding schemes (Hoda *et al*. 2014; Bytyqi *et al*. 2015; FAO, 2015).

The decline of native livestock breeds is a significant concern across Europe. Intensive agriculture, urbanization, uncontrolled crossbreeding, replacement by high-yielding commercial breeds, and socio-economic shifts in rural communities have led to a steady contraction of local populations (Oldenbroek & van der Waaij, 2014; FAO, 2023). Consequently, many traditional livestock breeds are now endangered or critically endangered, threatening the irreversible loss of genetic biodiversity and unique adaptive traits that could prove invaluable for future climate adaptation strategies (Gizaw *et al*. 2007).

Effective conservation and utilization of animal genetic resources require comprehensive breed characterization. Phenotypic, productive, reproductive, demographic, and socio-economic characterizations represent the foundational steps required to develop viable breeding strategies, conservation plans, and monitoring frameworks (Baumung *et al*. 2004; Taberlet *et al*. 2011). According to international guidelines set by the FAO, compiling comprehensive breed inventories is vital for evidence-based conservation policy and sustainable breeding practices (FAO, 2012; FAO, 2014a). While baseline phenotypic and morphological data exist for Kosova's sheep populations, comprehensive data regarding their productive potential, reproductive performance, and precise conservation risk status remain scarce (Casasús *et al*. 2012; Bytyqi *et al*. 2015). Holistic scientific research addressing these biological and genetic performance traits is therefore urgently needed.

To address these knowledge gaps, this study provides a comprehensive characterization of the four indigenous sheep breeds of Kosova (BAL, KOS, BAR, and SHA), with a specific emphasis on the highly vulnerable BAL and KOS populations. This assessment encompasses phenotypic, morphometric, productive, reproductive, and demographic traits viewed through the lens of gene pool conservation. The specific objectives were to: i) measure breed-specific morphometric traits and markers of local adaptation; ii) evaluate key productivity and reproductive performance metrics under current farming conditions; iii) assess contemporary population structures and determine conservation risk status using standardized FAO guidelines; and iv) identify and prioritize the breeds in greatest danger of genetic erosion due to critically low population sizes.

By establishing a robust baseline of the biological potential, adaptive characteristics, and conservation priorities of these breeds, this study aims to support the implementation of effective *in situ* and *ex situ* conservation strategies in Kosova and the wider Balkan region.

2. MATERIALS AND METHODS

2.1 Study Area

This study was conducted across various municipalities in Kosova where traditional sheep rearing remains an integral component of rural economic activities. The region is highly significant for its indigenous livestock farming practices, which primarily utilize natural grazing resources under extensive and semi-intensive management systems. Kosova experiences a continental climate characterized by distinct seasonal variations that directly influence seasonal forage availability and overall animal productivity. Natural pastures, semi-natural grasslands, and communal rangelands serve as the primary forage base, particularly within traditional low-input production systems. These environmental and management characteristics are representative of small ruminant production systems across Southeastern Europe, where livestock relies heavily on seasonal grazing and native rangelands. Such agro-ecological conditions are uniquely suited for maintaining locally adapted indigenous sheep breeds within low-input, environmentally harsh landscapes (FAO, 2012; Bytyqi *et al*. 2015; FAO, 2015). Similar marginal environments have been globally recognized as critical strongholds for sustaining unique genetic diversity in livestock populations (Cinkulov *et al*. 2008; Oldenbroek & van der Waaij, 2014; Adeniyi *et al*. 2022).

2.2 Study design

This research utilized a cross-sectional field survey design aimed at evaluating the contemporary status of indigenous sheep breeds in Kosova. This methodology was based on standardized international guidelines established by the FAO for the characterization of animal genetic resources, combining direct phenotypic evaluation, production record monitoring, and structured interviews with livestock farmers (FAO, 2014a,b). This methodological framework ensures a standardized data collection process and enhances comparability of the findings. Such an approach has been widely deployed in studies assessing indigenous small ruminants managed under extensive and semi-intensive conditions (Gizaw *et al*. 2007; Dagnew *et al*. 2017).

2.3 Geographic Distribution of Indigenous Sheep Breeds

The native sheep populations of Kosova are primarily represented by four recognized indigenous breeds: Balusha (BAL), Bardhoka (BAR), Sharri (SHA), and Kosova (KOS), all of which belong to the broader long-tailed Pramenka group. Although indigenous crossbred sheep (CRO) occupy a significant share of national sheep production, they fell outside the scope of this study. The four purebred populations are distributed across distinct agro-ecological zones-including lowland plains, hilly regions, and mountainous areas-frequently managed in mixed flocks or interspersed with crossbred animals (Figure 1).

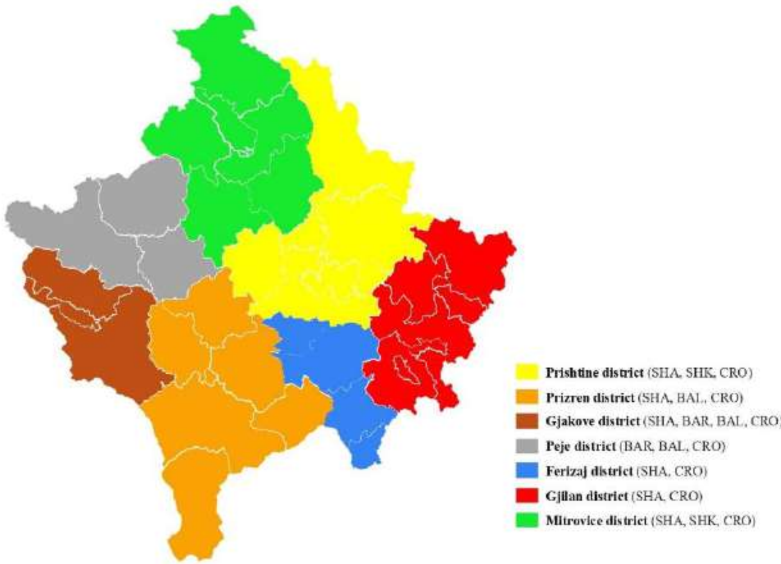

Fig.1. Geographic distribution of indigenous sheep population breeds and their crosses in Kosova. *Source: KAS, 2024; MAFRD, 2025.*

2.4 Sampling Strategy and Farm Selection

A purposive sampling strategy was implemented to ensure the inclusion of farms maintaining purebred indigenous sheep populations. The selection criteria included:

- Breed Purity: The confirmed presence of locally adapted purebred indigenous sheep.
- Production System Variety: Diverse representation of traditional production management (extensive and semi-intensive systems).
- Geographic Coverage: Balanced distribution across distinct agro-ecological zones, including lowland plains, hilly areas, and mountainous uplands.
- Producer Cooperation: Farmers' willingness to participate in the study and provide reliable production records.

Breed identification was initially based on farmer reports and subsequently verified through phenotypic classification in accordance with FAO standards. Field evaluations were conducted by animal science experts specializing in the native sheep breeds of Kosova. Within each selected farm, individual animals were randomly chosen for detailed morphometric and phenotypic evaluation-including body size, fleece coloration, tail morphology, wool structure, and body conformation-to minimize selection bias.

Furthermore, extensive efforts were made to mitigate misclassification by selecting farms that strictly maintained breed purity and avoided breed admixture. Special care was taken to exclude farms where unmonitored crossbreeding occurred within mixed flocks. This rigorous approach aligns with field-based livestock genetic resource studies where population structures are often fragmented or unbalanced (Tesema *et al.* 2024), thereby ensuring accurate interpretation of the results.

2.5 Data Collection Procedures

Data were gathered using a combination of structured questionnaire surveys, direct field observations, and personal interviews. The field surveys and observations were strategically timed during the breeding and lactation seasons to capture accurate seasonal variations in reproductive and productive performance.

The questionnaire was adapted from the standardized FAO guidelines for livestock characterization (FAO, 2012; 2023) and was structured to capture data on:

- Flock composition and demographic structure;
- Management practices and breeding strategies;
- Feeding systems and seasonal forage resources; and
- Reproductive performance and productive traits (e.g., milk yield, lamb survival).

This mixed-method approach enabled the integration of quantitative production metrics with qualitative management data, allowing for a comprehensive contextual interpretation of performance traits under real-world farming conditions (Bytyqi *et al.* 2015; Dagnew *et al.* 2017).

Table 1. Morphometric, reproductive, and production traits of sheep with key references

Trait	Measures	Unit	Key Notes	References
Body Weight	Live weight of the sheep	kg/	Growth, nutrition, breed potential	Serradilla, 2014

Fertility (%)	% of ewes that become pregnant	%	Only conception, not litter size	Silveira Cougo et al., 2024
Lambing Rate (%)	Number of lambs per ewe mated	%	Includes fertility + prolificacy	Priolo *et al.* 2001
Milk Yield	Total milk produced per lactation	kg/lactation	Reflects milk production ability, nutrition, and health	FAO, 2023
Withers Height	Height at shoulders	cm	Skeletal growth and breed type	Serradilla, 2014
Body Length	Distance from shoulder to pin bone	cm	Body frame, meat yield potential	Serradilla, 2014
Chest Girth	Circumference behind front legs	cm	Muscle development, body condition	Silveira Cougo *et al.* 2024
Average Ewe Weight	Mean live weight of adult females	kg	Productivity, reproductive potential	Anim-Jnr, 2023
Average Ram Weight	Mean live weight of adult males	kg	Breeding potential, growth	Silveira Cougo *et al.* 2024
Age at First Lambing	Age at first birth	months	Onset of reproduction; generation interval	Anim-Jnr, 2023
Fertility Rate (%)	% of ewes that become pregnant	%	Only conception, not litter size	Silveira Cougo *et al.* 2024
Stillbirth (%)	% of lambs born dead	%	Reflects perinatal losses	Anim-Jnr, 2023
Lamb Survival (%)	% of lambs alive at a set age (weaning)	%	Early life survival; health & management	Anim-Jnr, 2023
Lambing Interval (months)	Time between successive lambing	months	Shorter interval = higher reproductive efficiency	Anim-Jnr, 2023

2.6 Recorded Parameters

2.6.1 Flock Structure and Breed Composition

The experimental sample comprised 20 farms (5 farms per breed) and 180 individual animals (45 animals per breed) monitored during the year 2025. Management data analysis encompassed total flock size, the number of breeding females and males, the number of replacement stock, feeding regimens, veterinary intervention records, and breed purity (purebred versus crossbred individuals).

2.6.2 Reproductive Efficiency

Reproductive efficiency indicators included age at first lambing, lambing interval, fertility rate (percentage of ewes lambing), and lamb survival rates up to weaning age (Table 1).

2.6.3 Milk Production

Milk production traits evaluated included total milk yield per lactation, lactation length, milking frequency, and primary milk utilization (domestic consumption or artisanal cheese processing) during the systematic sampling periods (Table 1).

2.6.4 Management and Feeding Systems

Information regarding feeding regimens, dietary supplementation, housing, and seasonal management practices was compiled to categorize the traditional production frameworks into three primary grazing systems: extensive rangeland, semi-intensive, and transhumant grazing systems. To establish traditional adaptation characteristics within their respective native habitats, no chemical feed analyses were performed in this study.

2.7 Phenotypic Description

Phenotypic characterization was conducted in strict accordance with the guidelines provided by the FAO (FAO, 2012). Breeds were identified and characterized based on physical appearance, including mature body weight, coat and fleece colour patterns, wool structural traits, head profiles, ear position/orientation, presence or absence of horns, tail morphology, and overall body conformation.

2.8 Data Validity and Quality Control

Data validation involved cross-verifying farmer interview responses against direct field observations, conducting repeat interviews on selected baseline farms, and discarding erroneous or incomplete data entries. This rigorous cross-checking framework ensured data integrity and minimized observational bias (FAO, 2012).

2.9 Statistical Analysis

Descriptive statistics-including means, standard deviations, ranges, and frequencies-were calculated for all evaluated traits. Comparative analyses of continuous variables were performed using a Generalized Linear Model (GLM) with breed designated as a fixed factor. Least Squares Means (LSM) and Standard Errors (SE) were calculated for primary quantitative traits, including body weight, fertility rate, litter size, and milk production (McCulloch and Neuhaus, 2013). Analytical interpretation prioritized biological significance and effect sizes alongside absolute p-values (Kutner *et al*. 2005).

2.10 Ethical Issues

All applicable international and institutional guidelines for the care and use of agricultural animals in research were strictly followed. Farmer participation was entirely voluntary, and written or verbal informed consent was secured prior to data collection. Animal handling and morphometric measurements were strictly non-invasive, causing no distress to the livestock.

2.11 Compliance with Methodology

The experimental design and protocols complied with the FAO guidelines on livestock phenotypic characterization (FAO, 2012), global monitoring frameworks for animal genetic resources (FAO, 2015), and established statistical methodologies standard in animal breeding and genetics literature.

PRISMA-Based Review of Published Literature Related to Balkan Sheep Breeds

A systematic literature review was integrated into this study to establish context and provide comprehensive comparative data regarding sheep breeds across the wider Balkan region. This review followed the Preferred Reporting Items for Systematic Reviews and Meta-Analyses (PRISMA) framework, enhancing the scientific validity of the comparative discussion in alignment with contemporary standards in international animal science journals.

Table 2. PRISMA-style summary and topic distribution of studies on Balkan sheep breeds

Category / Research Topic	**Number of Records / Studies**
PRISMA Flow of Records	
Records identified through database searching (Scopus, Web of Science, CAB Abstracts)	215
Additional records from institutional reports and FAO publications	32
Total records identified	247
Records after removal of duplicates	201
Records screened (title and abstract)	201
Records excluded (irrelevant topics)	118
Full-text articles assessed for eligibility	83
Studies excluded after full review	50
Studies included in analysis	30
Distribution of Included Studies by Topic	
Genetic diversity characterization	5
Production traits and performance	5
Conservation and biodiversity	4
Milk production and dairy traits	5
Adaptation to mountain systems	4
Institution reports	7

3. RESULTS AND DISCUSSIONS

3.1 Population structure

The population structure of indigenous sheep in Kosova exhibits a pronounced imbalance in both numerical size and conservation status across breeds, reflecting historical selection pressures and contemporary shifts in breeding management systems (Table 3). Among the populations evaluated, SHA is the most populous breed, numbering approximately 126,000 head (including 85,000 breeding ewes), which indicates its successful integration into modern production systems and a stable demographic baseline. The BAR breed represents the second largest purebred population at approximately 31,800 head, followed by indigenous crossbreds (CRO type) at roughly 50,800 head. In stark contrast, the BAL breed exhibits a critically restricted population size, consisting of only about 450 breeding ewes and 180 lambs. The demographic outlook for the KOS breed is even more critical, with fewer than 100 breeding females and only a few remaining rams. Such precipitous declines in population size expose these two native genotypes to acute risks of genetic drift, inbreeding depression, and stochastic extinction. Cumulatively, while the total native sheep census stands at approximately 209,300 head, this figure masks a highly skewed distribution heavily favouring the dominant SHA and BAR breeds at the expense of the disappearing BAL and KOS lineages. These demographic trends align closely with global assessments by the FAO (2023), which document rapid genetic erosion among European native livestock due to commercial breed replacement, indiscriminate crossbreeding, and rural depopulation. Similar severe genetic bottlenecks have been reported across various Balkan sheep populations, markedly increasing the risk of inbreeding while reducing the effective population size (N_e) necessary to sustain long-term adaptive potential (Baumung *et al*. 2004; Oldenbroek and van der Waaij, 2014).

Table 3. Estimated population structure of indigenous sheep breeds in Kosova

Category	**Estimated number**					**Total**
	KOS	**BAL**	**BAR**	**SHA**	**CRO**	
Breeding ewes	50	450	23,000	85,000	34,000	≈142,500
Replacement lambs	30	180	7,500	36,000	15,000	≈58,700
Breeding rams	3	30	1,300	5,000	1,800	≈8,100
Totalpopulation	**<83**	**≈660**	**≈31,800**	**≈126,000**	**≈50,800**	**≈209,300**

Source: MAFRD, 2025; CRO=Crosses for different sheep breeds

3.2 Production performance and adaptive efficiency

Significant differences among breeds ($P < 0.05$) were observed for primary production characteristics-including pre-mating body weight, prolificacy index, and milk yield-across the heterogeneous agro-ecological zones of Kosova (Table 4).

The phenotypic variations captured across these performance traits highlight the distinct genetic profiles and evolutionary adaptations of the four breeds to their localized environments:

- **Pre-Mating Body Weight:** The mean pre-mating body weight was highest for the BAL breed (48.8kg), closely followed by BAR (48.2kg), whereas significantly lower body weights were recorded for SHA (46.8kg) and KOS (44.6kg). The superior body weights observed in BAL and BAR sheep suggest a highly efficient capacity to utilize seasonal forage resources within their respective agricultural niches.
- **Reproductive Efficiency:** Prolificacy varied markedly among the evaluated groups. The highest lambing index was recorded in SHA sheep (1.31), demonstrating distinct reproductive superiority. This high index highlights the robust maternal capacity and phenotypic adaptation of the SHA breed to harsh, extensive mountainous grazing landscapes. Strong reproductive performance was also evident in the BAR breed (1.26), followed by moderate performance in BAL sheep, and a critically depressed rate in the KOS breed (1.22). This low reproductive efficiency in KOS sheep likely signifies severe demographic decline compounded by inbreeding depression within its highly restricted gene pool.
- **Dairy Performance:** Total milk production exhibited the most pronounced inter-breed variation. The BAR breed produced the highest milk yield (138.4kg/lactation), outperforming BAL (101.1kg/lactation), SHA (95.2kg/lactation), and KOS (84.2kg/lactation).

Table 4. Least square means (LSM ± SE) of production traits in selected Balkan sheep breeds

Breed	**No. of farms**	**No. of animals**	**Body weight at mating (kg)**	**Lambing rate (%)**	**Milk yield (kg/lactation)**	**Adaptation**
BAL	5	45	48.8 ± 1.8^{a}	1.27 ± 0.03^{b}	101.1 ± 5.6^{b}	Lowland adaptation and Mountain grazing
KOS	5	45	44.6 ± 1.5^{c}	1.22 ± 0.03^{c}	84.2 ± 4.9^{c}	Extensive systems
SHA	5	45	46.8 ± 2.1^{b}	1.31 ± 0.05^{a}	95.2 ± 5.1^{b}	High altitude
BAR	5	45	48.2 ± 2.3^{a}	1.26 ± 0.03^{b}	138.4 ± 6.4^{a}	Lowland adaptation and Mountain grazing

***** Different superscripts within columns indicate **significant differences ($P < 0.05$)**.

This clearly highlights the physiological trade-off between production potential and adaptive efficiency: the BAR breed is highly adapted for specialized dairy production within semi-intensive lowland systems, whereas the SHA breed prioritizes reproductive efficiency and environmental resilience over high milk yields. In contrast, the KOS breed performed poorly across all evaluated traits, a trend likely attributable to cumulative genetic drift within its small population pool alongside management inadequacies. This phenotypic pattern aligns with established livestock literature, which demonstrates that indigenous sheep populations under marginal conditions optimize adaptive resilience and survival traits at the expense of high production metrics when compared to commercial breeds managed under optimized nutritional regimens (Gizaw *et al*. 2007; Devendra, 2012).

3.3 Morphometric differentiation and ecological adaptation

Pronounced phenotypic variations among the four breeds were further validated by morphometric evaluation, reflecting long-term adaptation to specific ecological niches and historical selection goals (Table 5).

The distinct skeletal architectures observed across the populations highlight how environmental demands shape breed morphology:

- **Sharri (SHA):** This breed exhibited the largest overall body frame, characterized by a height at withers of 65–70 cm, a body length of 68–74 cm, and a chest circumference of approximately 110 cm, alongside a substantial mature ewe body weight ranging from 60–75 kg. This larger skeletal structure and enhanced thoracic capacity are indicative of an evolutionary adaptation to rugged mountainous habitats, where greater mobility and physical stamina are required to forage effectively across steep, high-altitude terrain.
- **Bardhoka (BAR):** The BAR breed also displayed a well-developed body frame (height at withers: 65–70 cm; body length: 70–75 cm), reflecting its adaptation to favourable lowland environments and semi-intensive management. Morphologically, SHA sheep maintained a slightly deeper chest girth and longer body profile than BAR sheep, supporting their specialized adaptation to the rigorous conditions of transhumant mountain management.
- **Kosova (KOS):** In stark contrast, the KOS sheep represented the smallest and most compact phenotype evaluated (height at withers: 60–65 cm; mature ewe weight: 40–50 kg), adapted to highly marginal environments.

Reduced mature body size is recognized as a fundamental biological adaptation mechanism in low-input farming systems; a smaller body mass lowers fasting maintenance energy requirements, thereby enhancing survival capacity during periods of severe seasonal feed scarcity (Gizaw *et al.* 2007).

Table 5. Morphometric measurements of BAL, KOS, BAR, SHA

Trait	**BAL**	**KOS**	**BAR**	**SHA**
Withers height (cm)	68–74	60–65	65–70	65–70
Body length (cm)	72–80	65–70	70–75	68–74
Chest girth (cm)	90–105	80–90	85–100	95–110
Average ewe weight (kg)	55-65	40–50	48–55	60–75
Average ram weight (kg)	75-80	60–70	65–75	65–75

In general, the documented diversity in morphometric traits confirms that these four breeds belong to the broader genetic complex of Balkan long-tailed sheep, having evolved through distinct natural and artificial selection pressures across varied ecological conditions. Such distinct morphological differentiation aligns with patterns previously reported among indigenous livestock populations across other Balkan and Mediterranean regions, where mature body size and skeletal conformation are highly dependent on altitude, seasonal nutritional planes, and localized production management systems (Bytyqi *et al*. 2014; Serradilla, 2014).

3.4 Reproductive performance and population viability

Additional reproductive metrics further illustrate the physiological differentiation between these breeds and underscore the critical urgency of their conservation (Table 6). The SHA breed exhibited the highest reproductive potential, characterized by exceptional fertility rates (92–96%) and high lamb survival rates (90–95%), coupled with low pre-weaning mortality (2–4%). The BAR breed similarly demonstrated high reproductive efficiency, validating its robust adaptability to semi-intensive lowland production systems. In contrast, the reproductive performance of the BAL breed was moderate; while it maintained acceptable fertility rates, it suffered from elevated stillbirth and mortality rates. This compromised reproductive efficiency is closely linked to its restricted population size and the subsequent erosion of genetic diversity. The KOS breed exhibited the poorest reproductive performance among the evaluated populations, with depressed fertility rates (82–88%) and significantly elevated stillbirth rates (4–7%).

Table 6. Reproductive parameters of selected Balkan sheep breeds

Breed	**Age at first lambing (months)**	**Fertility rate (%)**	**Stillbirth (%)**	**Lamb survival (%)**	**Lambing interval (months)**
BAL	14–16	88–92	3–5	85–90	12
KOS	15–17	82–88	4–7	80–85	12–13
SHA	15–17	92–96	2–4	90–95	11–12
BAR	14–16	90–94	2–5	88–92	12

These results strongly suggest the presence of inbreeding depression and a concomitant loss of genetic variability, driven by critically small population sizes (N_e). Similar demographic and genetic patterns have been widely documented in isolated livestock populations, where a restricted effective population size accelerates genetic drift, leading to reproductive inefficiency and a decline in overall fitness traits (Hoda *et al*. 2014; FAO, 2015). Conversely, the relatively stable lambing intervals observed across all evaluated breeds (11–13 months) indicate that basic reproductive cyclicity has been maintained. Nevertheless, net reproductive efficiency differs substantially among the populations, with SHA and BAR exhibiting clear competitive advantages in terms of long-term productive sustainability.

3.5 Conservation status and genetic resource implications

The integration of demographic census data and field performance metrics demonstrates highly divergent conservation risks among Kosova's indigenous sheep breeds (Table 7). The SHA sheep population is currently classified as ”not at risk” due to its large, stable census numbers exceeding 120,000 head. Conversely, while the BAR population is numerically stable, it exhibits vulnerability to genetic dilution from indiscriminate crossbreeding. The demographic trends for the BAL and KOS populations are critical; numbering approximately 500–800 and fewer than 100 animals, respectively, these breeds fall directly into the FAO ”endangered” and "critically endangered" risk categories, placing them under immediate threat of extinction. These findings align closely with global assessments by the FAO (2023) regarding the accelerated depletion of local livestock genetic resources across Europe. The precipitous decline of the BAL and KOS breeds is particularly alarming given that they harbor unique adaptive traits. These evolutionary characteristics include high resilience to extreme environmental stressors, the capacity to efficiently utilize low-quality lignocellulosic forage, and potential genetic resistance to endemic pathogens and climate-induced stress factors (Ajmone-Marsan *et al*. 2010).

Table 7. Conservation status of sheep breeds in Kosova

Breed	Estimated population	FAO risk status
SHA	>120,000	Not endangered
BAR	About 30,000	Not endangered currently with tendency to Vulnerable
BAL	500–800	Endangered
KOS	<100	**Critically endangered**

Source: FAO, 2023; MAFRD, 2025

3.6 Integrated implications for conservation and sustainable breeding

The combined analysis of population demographics, morphometric profiles, production characteristics, and reproductive efficiencies highlights a clear gradient of conservation urgency among Kosova's indigenous sheep genetic resources. While the SHA and BAR breeds demonstrate contemporary demographic stability and production viability, the BAR breed requires active genetic monitoring to mitigate rising crossbreeding tendencies. Conversely, the BAL and KOS breeds have reached critical thresholds that require immediate, structured *in situ* and *ex situ* conservation interventions. To prevent irreversible genetic erosion and safeguard these unique genotypes, a coordinated conservation framework should be implemented in the following chronological and structural order:

1. Establish Nucleus Breeding Flocks;
2. Implement Controlled Mating Schemes;
3. Develop Farmer Incentive Frameworks;
4. Initiate Structured Breeding Programs;
5. Execute Systematic Cryopreservation.

These targeted conservation strategies comply fully with global operational guidelines for the management and preservation of small animal genetic resources (Baumung *et al*. 2004; FAO, 2012). In the absence of immediate policy and management interventions, further genetic degradation of the BAL and KOS populations will be unavoidable, culminating in the permanent loss of unique, locally adapted alleles. Ultimately, the indigenous sheep breeds of Kosova represent an intricate network of genetically distinct populations shaped by centuries of ecological adaptation and traditional production demands. While the SHA and BAR breeds possess immediate commercial value for sustainable modern livestock production, the highly vulnerable BAL and KOS genotypes represent indispensable genetic reservoirs that demand urgent, uncompromising protection.

4. CONCLUSIONS

The findings of this study provide a systematic evaluation of the indigenous sheep breeds of Kosova, demonstrating their critical significance to regional livestock biodiversity and the long-term sustainability of small ruminant production systems. Pronounced variations were identified across the evaluated genotypes, namely the BAL, KOS, BAR, and SHA breeds, regarding their morphometric traits, prolificacy indexes, dairy performance, and adaptive capacities within distinct agro-ecological zones. Specifically, the SHA and BAR breeds exhibit superior production and reproductive efficiencies, driven by their successful adaptation to mountainous and lowland production systems, respectively. Conversely, the BAL and KOS breeds are characterized by depressed production metrics and dangerously restricted population sizes, rendering them highly vulnerable to genetic drift, inbreeding depression, and stochastic extinction. Under the framework established by global conservation guidelines, the KOS breed is classified as a ”critically endangered” population, while the BAL breed is categorized as ”endangered”. Ultimately, this study underscores that comprehensive phenotypic and productive characterization provides the baseline data necessary for making evidence-based policy decisions regarding the conservation and strategic utilization of native animal genetic resources ($AnGR$). Preserving these indigenous genotypes is paramount not only for maintaining agricultural biodiversity, but also for securing the climate resilience, food security, and adaptive sustainability of livestock farming systems across Kosova and the broader Balkan region.

ACKNOWLEDGMENT

The authors owe a debt of a special gratitude to all participating farmers for their invaluable involvement, dedication, and excellent cooperation throughout this study.

Ethics. All experimental work with animals was performed according to international standards for the ethical treatment of livestock and national regulations on animal welfare in Kosovo. The fieldwork was aimed at minimizing the impact on animals; sampling and handling were conducted by skilled personnel following standard husbandry practices used by farmers.

Data accessibility. The datasets used and/or analyzed during the current study are available from the corresponding author upon reasonable request. Some herd data from the participating farmers and farm owners are unavailable due to privacy agreements but can be provided in an aggregated form.

Declaration of AI use. No artificial intelligence technologies were employed for data generation, experimental execution, or statistical analysis in this paper. AI-based technologies were solely used to enhance language editing and provide editorial assistance during the manuscript writing process, without affecting the scientific content or results.

Authors' contributions. H.B.: conceptualization, methodology, project administration, supervision, writing-original draft; **H.M.**: conceptualization, investigation; **A.K.:** conceptualization, investigation; **Xh.R.:** conceptualization, investigation, data curation; **F.K.:** methodology, formal analysis, writing-review and editing.

All authors gave final approval for publication and agreed to be held accountable for the work performed therein.

Conflict of interest declaration. The authors declare that they have no competing financial interests or personal relationships that could have appeared to influence the work reported in this paper.

Funding. The authors received no external funding for this research. This study was carried out at the personal expense of the researchers without any financial aid.

Acknowledgements. The authors greatly appreciate the contribution of the livestock farmers from Kosovo who participated in this research and provided access to their flocks.

REFERENCES

Adeniyi OO, Simon R, Bytyqi H, Kugler W, Mehmeti H, Berisha K, Simčič M, Magdy M, Lühken G. 2022. Capturing genetic diversity and selection signatures of the endangered Kosovar Balusha sheep breed. *Genes*, ***13*****(5):** 866. https://doi.org/10.3390/genes13050866.

Ajmone-Marsan P, Garcia JF, Lenstra, JA. 2010. On the origin of cattle: How aurochs became cattle and colonized the world. *Evolutionary Anthropology,* ***19*(3):** 148–157. https://doi.org/10.1002/evan.20267.

Anim-Jnr AS, Sasu P, Bosch C, Mabiki FP, Frimpong YO, Emmambux MN, Greathead HMR. 2023. Sustainable small ruminant production in low- and middle-income African countries: Harnessing the potential of agroecology. *Sustainability,* ***15*(21):** 15326. https://doi.org/10.3390/su152115326.

Baumung R, Simianer H, Hoffmann I. 2004. Genetic diversity studies in farm animals: A survey. *Journal of Animal Breeding and Genetics,* ***121*(6):** 361–373. https://doi.org/10.1111/j.1439-0388.2004.00479.x.

Bytyqi H, Baumung R, Mehmeti H, Fuerst-Waltl B. 2014. Phenotypic characterization and description of production systems of autochthonous sheep breeds in Kosova. *Animal Genetic Resources,* ***54***: 163–170. https://doi.org/10.1111/j.1439-0388.2004.00479.x.

Bytyqi H, Fuerst-Waltl B, Mehmeti H, Baumung, R. 2015. Economic values for production traits for different sheep breeds in Kosova. *Italian Journal of Animal Science,* https://doi.org/10.4081/ijas.2015.3808.

Casasús I, Riedel JL, Blanco M, Bernués A. 2012. Extensive livestock production systems and the environment. In *Animal farming and environmental interactions in the Mediterranean region* (EAAP Scientific Series, 131, pp. 81–88). Wageningen Academic Press. https://doi.org/10.3920/978-90-8686-741-7_9.

Cinkulov M, Popovski Z, Porcu K, Tanaskovska B, Hodzić A, Bytyqi H, Mehmeti H, Margeta V, Djedović R, Hoda A, Trailović R, Brka M, Marković B, Vazić B, Vegara M, Olsaker I, Kantanen, J. 2008. Genetic diversity and structure of the West Balkan Long-tail sheep types as revealed by microsatellite and mitochondrial DNA analysis. *Journal of Animal Breeding and Genetics,* ***125*(6):** 417–426. https://doi.org/10.1111/j.1439-0388.2008.00742.x.

Dagnew Y, Urge M, Tadesse Y, Gizaw S. 2017. Sheep production and breeding systems in northwestern lowlands of Amhara region, Ethiopia: Implication for conservation and improvement of Gumz sheep breed. *Open Journal of Animal Sciences,* ***7***: 179–197. 10.4236/ojas.2017.72015.

Food and Agriculture Organization of the United Nations (FAO). 2011. *Surveying and monitoring of animal genetic resources* (*FAO Animal Production and Health Guidelines No. 7*). Rome, Italy. https://www.fao.org/4/ba0055e/ba0055e00.pdf .

Food and Agriculture Organization of the United Nations (FAO). 2012. *Phenotypic characterization of animal genetic resources* (*FAO Animal Production and Health Guidelines No. 11*). Rome, Italy. https://www.fao.org/4/i2686e/i2686e00.pdf.

Food and Agriculture Organization of the United Nations (FAO). 2014a. *Synthesis progress report on the implementation of the Global Plan of Action for Animal Genetic Resources - 2014.* (*Information Document, Eighth Session of the Intergovernmental Technical Working Group on Animal Genetic Resources for Food and Agriculture, CGRFA/WG-AnGR-8/14/Inf.5*). Rome, Italy. http://www.fao.org/3/a-at136e.pdf.

Food and Agriculture Organization of the United Nations (FAO). 2014b. *Status and trends of animal genetic resources - 2014* (*Information Document, Eighth Session of the Intergovernmental Technical Working Group on Animal Genetic Resources for Food and Agriculture, CGRFA/WG-AnGR-8/14/Inf.4*). Rome, Italy. http://www.fao.org/3/a-at135e.pdf.

Food and Agriculture Organization of the United Nations (FAO). 2015. *The second report on the state of the world's animal genetic resources for food and agriculture*. FAO. http://www.fao.org/3/a-at136e.pdf

Food and Agriculture Organization of the United Nations (FAO). 2023. Domestic Animal Diversity Information System (DAD-IS). https://www.fao.org/dad-is.

Gandini G, Pizzi F, Stella A, Boettcher PJ. 2007. The costs of breed reconstruction from cryopreserved material in mammalian livestock species. *Genetics, Selection, Evolution,* ***39*****:** 465–479. PMID:17612484. PMCID:PMC2682823. DOI:10.1186/1297-9686-39-4-465.

Gizaw S, Van Arendonk JAM, Komen H, Windig JJ, Hanotte O. 2007. Population structure, genetic variation and morphological diversity in indigenous sheep of Ethiopia. *Animal Genetics,* ***38*****(6):** 621–628. https://doi.org/10.1111/j.1365-2052.2007.01659.x

Handley LL, Byrne K, Santucci F, Townsend S, Taylor S, Bruford MW, Hewitt GM. 2008. Genetic structure of European sheep breeds. *Heredity*, ***99*****(6):** 620–631. https://doi.org/10.1038/sj.hdy.6801039

Hoda A, Bytyqi H, Bozgo V. 2014. Genetic diversity of sheep breeds from Albania and Kosova revealed by mtDNA. *Journal of Endocytobiosis and Cell Research, 25*, 66–69. https://zs.thulb.uni-jena.de/content/main/journals/ecb/info.xml.

Kosova Agency of Statistics (KAS). 2024. Retrieved April 2025, from https://askdata.rks-gov.net/pxweb/en/ASKdata/ASKdata__Agriculture__Agricultural%20Household%20Survey/aeb11delee.px/

Kutner MH, Nachtsheim CJ, Neter J, Li W. 2005. *Applied linear statistical models* (5th ed.). McGraw-Hill. https://d1b10bmlvqabco.cloudfront.net/attach/is282rqc4001vv/is6ccr3fl0e37q/iwfnjvgvl53z/Michael_H_Kutner_Christopher_J._Nachtsheim_JohnBookFi.org.pdf

McCulloch CE, Neuhaus JM. 2013. Generalized linear mixed models. In *Wiley StatsRef: Statistics Reference Online*. Wiley. https://doi.org/10.1002/9780470057339.vag009.pub2Digital Object Identifier (DOI)

Ministry of Agriculture, Forestry and Rural Development (MAFRD). 2025. *Green report 2025*. Retrieved on May, 2026 https://mbpzhr.rks-gov.net/wp-content/uploads/2026/01/Raporti_i_Gjelber_2025_Final.pdf.

Notter DR. 1999. The importance of genetic diversity in livestock populations of the future. *Journal of Animal Science*, ***77*****(1):** 61–69. https://doi.org/10.2527/1999.77161x.

Johnsson M. 2023. Genomics in animal breeding from the perspectives of matrices and molecules. *Hereditas, 160*(1), 18. https://doi.org/10.1186/s41065-023-00285-w

Priolo A, Micol D, Agabriel J. 2001. Effects of grass feeding systems on ruminant meat colour and flavour: A review. *Annales de Zootechnie,* ***50*****(3):** 185–200. https://doi.org/10.1051/animres:2001125.

Serradilla JM. 2014. Breeding programs for small ruminants in Spain. In *Proceedings of the Internationally Participated Small Ruminant Congress* (pp. 16–18). Konya, Turkey.

Silveira Cougo AC, Brito G, Luzardo S. 2024. Carcass and meat quality of lambs from intensive grazing systems differing in the age of slaughter. *Meat and Muscle Biology,* ***8*****(1):** 1–12. https://doi.org/10.22175/mmb.16089.

Taberlet P, Coissac E, Pansu J, Pompanon F. 2011. Conservation genetics of cattle, sheep, and goats. *Comptes Rendus Biologies,* ***334*****(3):** 247–254. https://doi.org/10.1016/j.crvi.2010.12.007.

Tesema Z, Alemayehu K, Getachew T, Kebede D, Tilahun M, Deribe B, Lakew M, Worku Alebachew G, Taye M, Gizaw S. 2024. Genetic analysis of efficiency-related traits in Boer x Central Highland goats. *PLoS ONE,* ***19*****(7):** e0305749. https://doi.org/10.1371/journal.pone.0305749.

ESTIMATING RAMP TRAFFIC STATES IN SENSOR-SPARSE FREEWAY ENVIRONMENTS USING TRANSFER LEARNING

Kleona BINJAKU[1], Elinda KAJO MEÇE[2], Cecilia PASQUALE[3] and Simona SACONE[4]

[1,2]Department of Computer Engineering, Faculty of Information Technology, Polytechnic University of Tirana, Albania

[3,4]Department of Informatics, Bioengineering, Robotics and Systems Engineering, University of Genova, Italy

Author for correspondence: kleona.binjaku@fti.edu.al

KB, 0009-0006-9019-2481; EM, 0009-0002-7353-476X;
CP, 0000-0002-0760-4769; SS, 0000-0002-7114-8972

ABSTRACT

The lack of accurate readings on on-ramps and off-ramps, where sensors are frequently missing due to installation, maintenance, and financial constraints, is a key issue in freeway traffic condition estimation. The accuracy of traffic monitoring, modelling, and control applications is thus limited, especially in complex highway networks, by the associated lack of ramp flow and speed data. This study proposes a transfer-learning-based method for estimating on- and off-ramp traffic conditions using only mainline readings to overcome this difficulty. Specifically, we design a Bidirectional Long Short-Term Memory (Bi-LSTM) neural network that uses data-rich freeway segments with both mainline and ramp measurements to learn spatiotemporal traffic patterns. Seven days' worth of traffic data from seven Dutch freeway segments representing various traffic situations, geometric patterns, and ramp configurations are used to train the model. The trained network is then applied to sensor-limited freeway stretches with missing ramp data by utilizing transfer learning, which makes it possible to infer ramp traffic volume and speed without the need for additional physical equipment. The findings show that under different demand levels and congestion regimes, the proposed technique accurately reconstructs ramp traffic conditions. This suggests that the learned temporal representations can successfully substitute for missing ramp measurements and generalize well across various highway conditions. The proposed system supports improved traffic management and control in real-world applications by providing a practical and affordable way to improve traffic state estimation in freeway networks with sparse sensing equipment.

***Keywords*:** transfer learning, Bi-LSTM, ramp flow estimation, freeway traffic, sensor-limited sites

Publisher: Academy of Sciences of Albania

Citation: Binjaku K, Kajo Meçe E, Pasquale C, Sacone S. 2026. estimating ramp traffic states in sensor-sparse freeway environments using transfer learning. *Albanian Journal of Natural and Technical Sciences* (*AJNTS),* **31 (3):** 109-125. https://doi.org/10.67537/ajnts3103031
Classification: research
Subject Category: computer science + applied sciences + engineering subject area road traffic engineering, traffic flow, and volume dynamics

1. INTRODUCTION

Intelligent Transportation Systems (ITS) rely on accurate and timely traffic status estimation and forecasting to support successful traffic management and control tactics such as ramp metering, variable speed limits (VSL), and proactive congestion reduction. Ramp metering has long been regarded as a high-impact strategy for enhancing freeway throughput and stability. Extensively deployed feedback-based regulators like ALINEA have effectively demonstrated the real-world value of sensor-driven ramp control (Papageorgiou *et al*. 1991; Papageorgiou *et al*. 2002). Similarly, coordinated VSL methods have been proven to reduce stop-and-go waves and shock waves in crowded traffic, thereby enhancing safety and network performance when real-time measurements and predictions are available (Hegyi *et al*. 2005).

However, the availability, coverage, and quality of real-time traffic measurements gathered by loop detectors and other sensing technologies heavily dictate how well these ITS applications perform. Detectors are usually placed along the mainline of many freeway networks, while on-ramps and off-ramps are often uninstrumented because of financial, maintenance, or physical constraints (Ma *et al*. 2024, Ma *et al*. 2025). This sensory asymmetry is troublesome because ramps and weaving sections are crucial zones where traffic conditions can change suddenly due to merging and diverging movements, and where bottlenecks frequently form or propagate. Therefore, incomplete or biased traffic state representations can result in poor control performance (such as sub-optimal ramp-metering choices) and decreased short-term prediction accuracy—particularly during congestion onset, dissipation, or regime transitions.

Loop-detector data can also be compromised by missing or inaccurate readings due to sensor faults or communication difficulties, necessitating reliable reconstruction approaches (Chen *et al*. 2003, Maghrour and Torok, 2018). Standard statistical techniques struggle to capture the nonlinear and spatiotemporal dynamics of highway traffic, particularly around merging and diverging areas, and perform poorly under complicated flow patterns (Vlahogianni *et al*. 2014). Recent deep learning models, including LSTM-based architectures (Zhang *et al*. 2023) and network-level graph techniques like STGCN and DCRNN (Li *et al*. 2018; Yu *et al*. 2018), have improved traffic forecasts, but they rely largely on dense sensor coverage. The accuracy of traffic state estimation drops significantly in freeway segments lacking active ramp detectors. To address this, recent research has demonstrated the efficacy of transfer learning in reconstructing missing ramp traffic states (Ma *et al*. 2024, Pan and Yang 2010; Weiss *et al*. 2016). Transfer learning offers a viable alternative by allowing models trained in data-rich areas to adapt to sensor-limited environments.

This study addresses a persistent challenge of missing on-ramp and off-ramp measurements across freeway segments, which previously limited the scope and accuracy of our work (Binjaku *et al*. 2025a, Binjaku *et al*. 2024). We present a transfer-learning-enabled Bidirectional Long Short-Term Memory (Bi-LSTM) architecture that can infer ramp flow and speed without direct ramp instrumentation.

Unlike traditional reconstruction or localized modelling, our method is trained on a diverse corpus of data-rich freeway segments. This allows the model to learn generalizable spatiotemporal traffic patterns that capture how ramp conditions relate to mainline dynamics under varying geometric layouts, demand profiles, and congestion regimes. After training, the model is fine-tuned and applied to sensor-limited target locations without ramp measurements.

Through this design, the presented framework:

• Eliminates the reliance on ramp sensors, solving one of the most persistent data restrictions in highway traffic monitoring.

• Uses transferable temporal representations from diverse environments to improve prediction accuracy in sparse-data segments.

• Provides a scalable and cost-effective solution for ramp traffic state estimation, ideal for real-world freeway networks without full detector coverage.

• Generalizes across diverse freeway configurations, making it more flexible than previous transfer models that required closely matched source-target segment characteristics.

The primary contribution of this study is demonstrating that transfer-learning-driven Bi-LSTM models can precisely reconstruct ramp traffic states from mainline detector data alone. This offers a workable substitute for the deployment of physical ramp sensors and enables more thorough traffic state estimation in partially monitored networks.

The rest of this paper is structured as follows: The proposed approach, dataset, and preprocessing steps are detailed in Section II. The modelling approach and experimental findings are presented in Section III. Finally, the paper's conclusions and future study directions are outlined in Section IV.

2. RELATED WORK

Freeway traffic monitoring is highly reliant on data obtained from loop detectors; however, these sensors frequently generate missing, noisy, or corrupted observations due to equipment failures, calibration drift, or communication breakdowns. Classical loop-detector diagnostics and imputation methods—such as the real-time detection and replacement algorithms proposed by Chen *et al*. (2003) and the statistical reconstruction framework of Maghrour and Torok (2018)—illustrate the scale of missing data and the critical need for robust reconstruction procedures. Despite their utility, these techniques frequently assume linear relationships or rely on simple temporal smoothing, limiting their capacity to capture the nonlinear, spatiotemporal interdependencies inherent in freeway dynamics, particularly around merging and diverging areas. Comprehensive reviews of short-term forecasting methods highlight that conventional statistical models generally underperform in complex traffic scenarios, lacking the expressive power required to capture regime shifts, shockwave propagation, and localized congestion patterns (Vlahogianni *et al*. 2014).

The advancement of deep learning algorithms has greatly improved traffic state estimation. Recurrent neural networks, especially Long Short-Term Memory (LSTM) architectures, are highly effective at extracting temporal dependencies from traffic time series and remain durable even when training data contains gaps or noise. Indeed, Zhang *et al*. (2023)

found that LSTM-based transfer learning approaches can significantly increase prediction accuracy in the presence of incomplete data. Beyond sequence models, network-level deep architectures have recently gained popularity. For example, the Spatio-Temporal Graph Convolutional Network (STGCN) developed by Yu *et al.* (2018) uses graph convolutions to exploit spatial correlations between roadway segments, while the Diffusion Convolutional Recurrent Neural Network (DCRNN) introduced by Li *et al.* (2018) models traffic evolution as a diffusion process on a directed graph, achieving state-of-the-art performance on large urban networks. However, despite their high accuracy, these models require broad, dense sensor coverage. Their forecasting capability declines in freeway contexts lacking ramp sensors, or where data quality varies greatly across locations, due to domain mismatch and inadequate modelling of ramp-specific dynamics.

To address data scarcity, transfer learning has emerged as an effective paradigm. Foundational surveys by Pan and Yang (2010) and Weiss *et al.* (2016) formalize transfer learning as a method for transferring knowledge between domains with different distributions, feature spaces, or data availability. This makes transfer learning ideal for freeway networks where mainline detectors are abundant but ramp sensors are scarce. Consequently, transfer learning is increasingly utilized in transportation studies to estimate missing variables and enhance prediction when sensing infrastructures are incomplete. Ma *et al.* (2024) developed a data-driven transfer learning approach to predict on-ramp and off-ramp flows using only mainline loop detector data, achieving considerable accuracy improvements across corridors with diverse physical and operational conditions. Additionally, Zhang *et al.* (2023) showed how transfer learning can improve LSTM-based traffic forecasting models operating with incomplete datasets, supporting the premise that information from data-rich freeway segments can help reconstruct traffic states in data-poor sections. Similarly, Li *et al.* (2021) demonstrated that transfer learning techniques can improve the transferability of short-term traffic prediction models under data-deficient scenarios, particularly when historical data availability varies across network links.

The utility of transfer mechanisms in traffic modelling is further supported by recent literature. For instance, Zhou *et al.* (2022) showed that when sensor distributions differ between locations, spatial-temporal domain adaptation techniques can improve traffic forecasting performance. To enhance the spatial and temporal transferability of freeway crash risk prediction models, Liao and Chen (2025) proposed a Model-Agnostic Meta-Learning (MAML) framework. Their findings revealed increased resilience and flexibility across various domains, underscoring the broader potential of meta-learning techniques for effective knowledge exchange and rapid adaptation in traffic situations characterized by limited data or distribution shifts.

In summary, prior research demonstrates three major trends:

• Classical loop-detector diagnostics and statistical reconstruction methods struggle to represent nonlinear and spatiotemporal freeway dynamics under incomplete data conditions (Chen *et al*. 2003; Maghrour and Torok, 2018).

• Deep learning architectures—including LSTM-based models and graph-based networks such as STGCN and DCRNN—substantially improve traffic state estimation but assume dense, reliable sensing infrastructures, limiting their effectiveness in freeway environments with sparse ramp instrumentation (Yu *et al*. 2018; Li *et al*. 2018; Zhang *et al*. 2023).

• Transfer learning approaches successfully mitigate data scarcity by leveraging knowledge from data-rich locations to improve prediction in data-limited sections (Pan and Yang 2010, Weiss et al. 2016, Ma et al. 2024, Zhou *et al*. 2022; Liao and Chen, 2025).

3. PRESENTED APPROACH

The proposed methodology seeks to develop a transferable machine learning model capable of forecasting on-ramp and off-ramp traffic states—specifically flow and speed—across a broad range of congestion patterns. For this purpose, traffic data are gathered directly from the National Road Traffic Database (NWD), which provides high-resolution observations from loop detectors mounted along numerous freeway segments. The constructed dataset includes seven freeway segments, each featuring one on-ramp and one off-ramp, with measurements collected every five minutes over a seven-day period. Only data recorded between 11:00 and 19:55 are retained. Early morning and late evening intervals are eliminated because traffic conditions during these periods are primarily free-flowing and do not provide informative patterns regarding ramp-related congestion dynamics.

Prior to modelling, the dataset underwent extensive preprocessing to ensure data quality and temporal consistency. Non-numeric entries and sensor failures, such as division-by-zero outputs and negative readings, were initially identified and classified as missing values. These missing or faulty observations were subsequently addressed via linear interpolation along the temporal dimension, with forward- and backward-filling used to propagate values as needed to ensure the continuity of traffic dynamics between time steps.

A diverse range of traffic scenarios is represented throughout the entire dataset, including: (i) high-congestion episodes, where queues may form upstream of the off-ramp, between the off- and on-ramps, or downstream of the on-ramp; (ii) moderate or light congestion, where speeds deteriorate but exhibit minimal queue propagation; and (iii) free-flow periods, which serve as a non-congested baseline. Rather than being artificially simulated, these situations emerge naturally from empirical field data, ensuring that the model is exposed to authentic fluctuations in traffic dynamics. This diversity is crucial for the transfer learning framework, as it allows the trained model to operate reliably even on freeway sections where specific congestion patterns are either completely absent from the training data or occur infrequently. Further details are provided in Table 1.

Table 1. Information related to considered highway segments.

Segment position	Length (km)	Lanes (Up/Mid/Down)	Congestion level
A16 North Bound to Rotterdam	1.3	3/2/2	High
A4 South Bound to the Hague	1	2/1/3	Moderate
A22 North Bound to Beverwijk	1.2	2/2/2	Low
A20 West Bound to Hoek Van Holland	1.6	3/3/3	Moderate
A4 South Bound to Rotterdam	1.2	4/3/4	High
A9 North Bound to Alkmaar	2.5	4/3/5	High
A9 North Bound to Alkmaar 2	1.5	4/3/3	High

As input features, mainline flow, speed, and lane-count data are collected at three crucial cross-sections relative to each ramp: upstream of the off-ramp, between the off- and on-ramps, and downstream of the on-ramp. While speed readings are averaged per sensor layer, flow is aggregated to represent the total volume across all available lanes, since lane-by-lane measurements frequently contain missing entries or exhibit irregular lane usage. Because it defines the freeway's physical cross-section and directly influences local traffic bottleneck dynamics, the number of lanes is retained as an instructive structural feature at each measurement site. Contextual factors, such as the day of the week and the hour of the day, are also incorporated to account for systematic temporal variations in traffic demand.

The prediction objective is framed as a supervised learning problem aimed at estimating ramp flow and speed at both the on-ramp and off-ramp using upstream and downstream mainline measurements. Let's

$$x_t \in R^d \qquad (1)$$

represent the vector of input features at time t, which includes mean speeds, lane counts, aggregated flows, and temporal indicators. The corresponding target vector is defined as:

$$y_t = \begin{bmatrix} q_t^{on} \\ v_t^{on} \\ q_t^{off} \\ v_t^{off} \end{bmatrix}, \qquad (2)$$

where q and v denote the flow and speed on the respective on- and off-ramps. The learning goal is to approximate the underlying nonlinear mapping:

$$f: x_t \rightarrow y_t \qquad (3)$$

by minimizing the empirical loss function over the network parameters

$$\min_{\theta} \sum_{t=1}^{N} ||y_t - f_\theta(x_t)||^2 \qquad (4)$$

where θ represents the model's parameters

The primary prediction model is a Bidirectional Long Short-Term Memory (Bi-LSTM) network, selected because traffic dynamics exhibit both forward- and backward-propagating temporal dependencies. Unlike standard LSTMs that process input sequences strictly in chronological order, the Bi-LSTM consists of two distinct hidden layers: one that processes the input from past to future (forward pass), and another that processes it from future to past (backward pass). This architectural structure enables the model to estimate traffic states and ramp behaviour by leveraging contextual insights from both historical and subsequent time steps.

Each directional LSTM modifies its hidden state $h_t$and cell state c_t at time t according to the standard LSTM gating mechanism.

In the Bi-LSTM, the forward hidden state $h_t^{(f)}$and backward hidden state $h_t^{(b)}$are concatenated to form the final representation:

$$h_t^{(Bi)} = [h_t^{(f)} \parallel h_t^{(b)}] \qquad (5)$$

Using all available mainline and ramp measurements, the Bi-LSTM model is initially trained on the aggregated dataset of the seven freeway segments. This allows the network to learn generalized spatiotemporal representations of traffic evolution under varying geometric configurations and demand constraints. To transfer this knowledge to a target segment with missing ramp sensors, the pre-trained model weights are initialized and subsequently fine-tuned utilizing only the target segment's mainline inputs and any available sparse ramp indicators. While the final dense layers are updated to adapt to localized traffic conditions, the early Bi-LSTM layers are partially frozen to preserve the learned structural temporal dynamics during fine-tuning. This transfer strategy enhances model generalization in sensor-limited situations and minimizes overfitting. Figure 1 illustrates the proposed training and transfer learning pipeline, moving from multi-segment pre-training to target-segment fine-tuning.

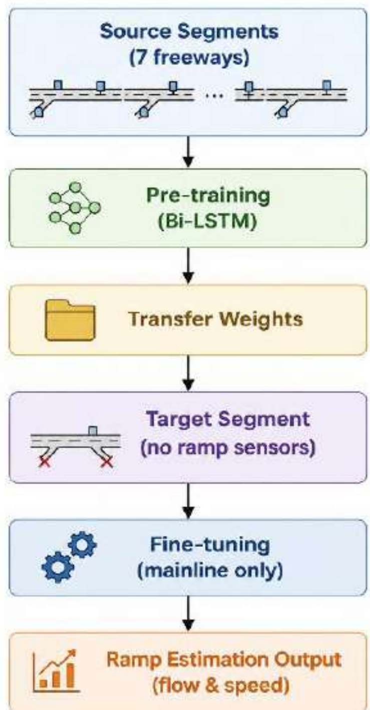

Fig.1. Proposed Bi-LSTM Transfer Learning Pipeline for Ramp Traffic Estimation.

By virtue of this design, the model accounts for both the influence of downstream bottlenecks (via the backward pass) and the delayed impact of upstream congestion waves (via the forward pass), both of which are critical to characterizing freeway–ramp interactions. Incorporating a backward temporal context provides a more comprehensive picture of traffic evolution surrounding the ramp interface, significantly improving its ultimate inference capabilities.

4. RESULTS AND DISCUSSIONS

The Bi-LSTM network described in the previous section was trained to capture complex temporal dependencies between mainline and ramp traffic states. The network architecture and training pipeline were designed to strike an ideal balance between prediction accuracy and generalization to previously unseen roadway segments. Table 2 and Table 3 summarize the key structural model configurations and training hyperparameters:

Table 2. Model parameters

Parameter	Value
LSTM Layers	2 layers (Bidirectional + standard LSTM)
LSTM Units	64 per layer
Dense Layers	2 TimeDistributed Dense (32 ReLU → 4 linear output)
Dropout	0.1

Table 3. Training parameters

Parameter	Value
Optimizer	Adam
Loss Function	MSE
Batch size	16
Epochs	120
Input sequence length	108-time steps (one day)
Scaling	RobustScaler

The sequence length of 108-time steps—corresponding to a full day of 5-minute aggregated data—was selected to capture complete diurnal traffic cycles, including peak and off-peak transitions. This extensive temporal context is critical for modelling recurring congestion patterns and ramp-mainline interactions. Given the relatively small number of freeway segments in the training corpus, the number of LSTM hidden units was set to 64 to balance model capacity with the risk of overfitting. Increasing the unit count beyond this threshold did not yield significant improvements in validation performance and introduced training instability. A batch size of 16 was selected to ensure stable gradient adjustments while maintaining computational efficiency on the compact dataset.

The trained model was evaluated on a hold-out freeway segment: the A20 eastbound toward Gouda. The resulting predictions are illustrated in Figure 2. Within this target segment, empirical field measurements are available only for the on-ramp, whereas physical sensors are entirely absent at the off-ramp. Consequently, the on-ramp predictions are directly compared against observed sensor data, whereas the off-ramp flow predictions are evaluated against estimated values computed via the conservation of flow between upstream and downstream mainline sensors. This baseline calculation follows the validation methodology established by Binjaku *et al*. (2025b) to assess estimation reliability. Regarding off-ramp speed, because the model relies predominantly on flow dynamics and the target section lacks off-ramp validation sensors, a direct comparative analysis against ground-truth data was not feasible.

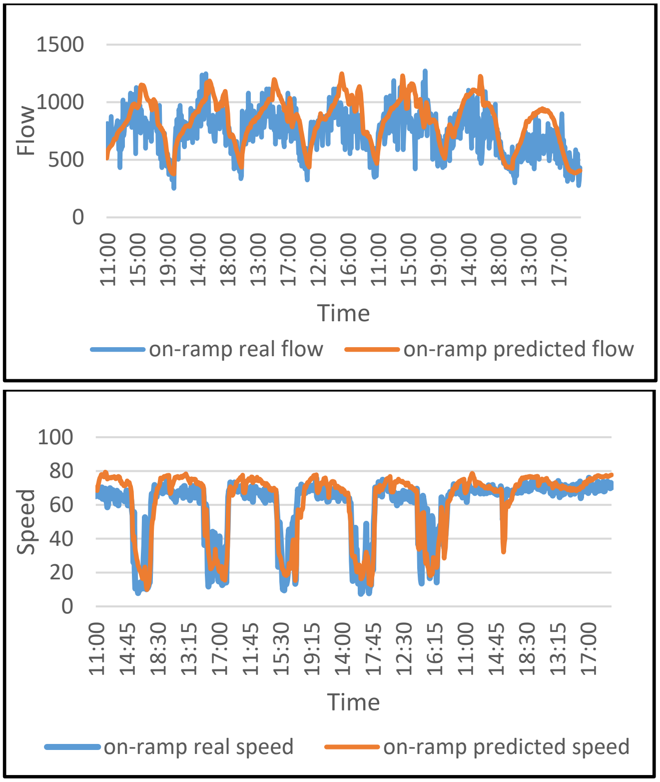

(a)

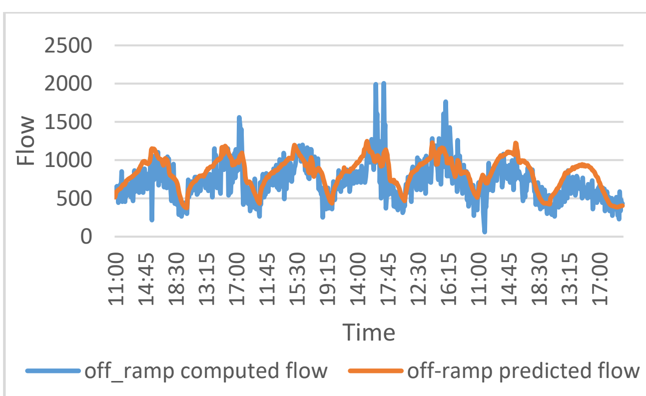

(b)

Fig. 2: Predicted versus observed on-ramp flow and speed (a), and estimated off-ramp flow (b).

To quantify prediction accuracy, we utilized the Mean Absolute Percentage Error (MAPE), which expresses the average absolute deviation between the predicted and reference values as a percentage of the actual value. The calculated validation errors are summarized in Table 4. These results demonstrate reasonable predictive accuracy, particularly considering the highly restricted size of the training dataset, which incorporates only seven freeway segments featuring highly heterogeneous traffic configurations. Despite this sparse data footprint, the model successfully captures underlying temporal traffic dynamics and delivers valuable operational estimates for sensor-limited environments.

To investigate model behaviour across varying traffic conditions, predictions were tested under distinct regimes: free-flow, moderate congestion, and heavy congestion. The network achieves its highest accuracy under free-flow and moderate conditions, where traffic dynamics are smoother and more predictable. Prediction errors increase marginally during peak congestion periods, particularly for ramp flow, due to abrupt changes in vehicle merging behaviour and localized shockwave propagation. Nevertheless, the Bi-LSTM maintains robust temporal tracking and does not diverge during congestion onset or dissipation phases, demonstrating strong stability during traffic regime shifts.

Table 4. MAPE Errors

	MAPE Error
On-ramp flow	0.220
On-ramp speed	0.155
Off-ramp flow	0.288

It is critical to remember that off-ramp target values are not direct sensor observations, but rather computed estimations based on mainline flow conservation between upstream and downstream detectors. As a result, the reported off-ramp errors should be viewed as the model's performance in comparison to the reconstructed reference values, rather than against ground-truth sensor data.

However, several limitations of the proposed approach must be acknowledged. First, the model was trained on a relatively small number of freeway corridors, which may restrict its immediate generalizability to vastly different regional networks. Second, model performance under non-recurrent traffic anomalies—such as traffic accidents, lane closures, or severe weather conditions—has not yet been validated. Finally, lane-specific ramp behaviour cannot be explicitly represented because the input features exclude ramp lane configurations or per-lane flows, which may limit the model's fine-grained microscopic accuracy.

5. CONCLUSIONS

This study presented a transfer-learning-enabled Bidirectional Long Short-Term Memory (Bi-LSTM) architecture designed to infer missing on-ramp and off-ramp traffic states using only upstream and downstream mainline detector measurements. The proposed framework addresses a persistent data restriction in freeway monitoring: the systematic absence of ramp instrumentation due to logistical and financial constraints. Unlike traditional approaches that depend on localized statistical reconstruction or require full sensor configurations, this study proves that reliable ramp traffic state estimation can be achieved by learning generalized spatiotemporal representations across data-rich corridors and transferring that knowledge to sensor-sparse target locations.

The architecture improves upon previous methodologies by integrating transfer learning with a bidirectional recurrent framework, thereby capturing both the forward and backward propagation of congestion dynamics. The proposed framework differs fundamentally from existing deep learning approaches that rely on dense sensor environments or require explicit ramp data to maintain estimation stability. Furthermore, incorporating highly heterogeneous freeway segments during the training phase exposes the model to diverse geometric layouts, demand profiles, and merging behaviours, markedly improving its structural resilience.

Experimental results indicate that the Bi-LSTM model generates reliable off-ramp flow estimates and accurately predicts on-ramp dynamics, despite operating under limited supervision and utilizing a compact training dataset. These findings demonstrate that data-driven temporal networks can successfully substitute for physical infrastructure gaps when enhanced by transfer mechanisms. Consequently, this methodology offers a practical, cost-effective framework for transportation agencies operating under tight capital or maintenance budgets.

Several promising avenues for future research remain. To further refine performance, physics-informed neural network (PINN) constraints could be integrated into the objective function to enforce strict traffic-flow conservation principles during training. This could enhance model stability under non-recurrent or extreme congestion anomalies. Additionally, expanding the network to accommodate multi-class traffic streams (e.g., separating passenger cars from heavy trucks) would yield a richer representation of ramp-mainline interactions. Generalization capabilities could also be extended through advanced domain adaptation, meta-learning, or multi-source transfer frameworks. Finally, integrating supplementary external data streams—such as real-time weather feeds, incident logs, or connected vehicle telemetry—would further strengthen the model's forecasting capacities under unpredictable road network regimes.

In summary, this work establishes a scalable and highly viable framework for inferring ramp traffic states solely from mainline data. By eliminating the necessity for total loop-detector coverage while sustaining robust prediction performance, this framework enhances freeway operational awareness and directly supports advanced, data-driven intelligent transportation management.

Ethics: This work did not require ethical approval from a human subject or animal welfare committee.

Conflict of Interest. We declare we have no competing interests.

Originality and Authorship. This work is based on the original data and ideas developed by the authors. No artificial intelligence tools were employed in the writing or preparation of this manuscript.

Author contributions. K.B.: ideation, conceptualization, methodology, model development, data acquisition, data preprocessing, model training, formal analysis, data interpretation, writing—original draft preparation, and corresponding author. Binjaku had full access to all the data and assumes responsibility for the accuracy and integrity of the data and results. **E.K.M.**: conceptualization, methodology, data interpretation, review and editing, and supervision. **C.P.**: supervision, methodological guidance, data interpretation, review and editing. **S.S.:** conceptualization, methodological guidance, supervision, data interpretation, and critical review and editing.

All authors have read and agreed to the published version of the manuscript.

Declaration of AI use: We confirm that no AI-assisted technologies were used to create this article.

REFERENCES

Binjaku K, Pasquale C, Sacone S, Meçe EK. 2024. A traffic model integrating long short-term memory networks with multi-class macroscopic equations. In *Proceedings of the IEEE 20th International Conference on Automation Science and Engineering (CASE 2024)*, Bari, Italy, pp. 4112–4118. https://doi.org/10.1109/CASE59546.2024.10711512.

Binjaku K, Pasquale C, Meçe EK, Sacone S. 2025a. Freeway traffic modelling by physics-regularized Gaussian processes. *IEEE Open Journal of Intelligent Transportation Systems*, **6:** 116–130. https://doi.org/10.1109/OJITS.2025.3532796.

Binjaku K, Meçe EK, Pasquale C, Siri S, Sacone S. 2025b. Predictive ramp metering control based on physics-informed LSTM with queue length constraints on entering ramps. In *Proceedings of the 20th Annual System of Systems Engineering Conference (SoSE 2025)*, Tirana, Albania, pp. 1–6. https://doi.org/10.1109/SoSE66311.2025.11083877.

Chen C, Kwon J, Rice J, Skabardonis A, Varaiya P. 2003. Detecting Errors and Imputing Missing Data for Single-Loop Surveillance Systems. *Transportation Research Record: Journal of the Transportation Research Board*, **1855(1)**: 160-167. https://doi.org/10.3141/1855-20.

Hegyi A, De Schutter B, Hellendoorn J. 2005. Optimal coordination of variable speed limits to suppress shock waves. *IEEE Transactions on Intelligent Transportation Systems*, **6(1):** 102–112. doi: https://doi.org/10.1109/TITS.2004.842408.

Li J, Guo F, Sivakumar A, Dong Y, Krishnan R. 2021. Transferability improvement in short-term traffic prediction using stacked LSTM network. *Transportation Research Part C: Emerging Technologies*, **124:** 102977. https://doi.org/10.1016/j.trc.2021.102977.

Li Y, Yu R, Shahabi C, Liu Y. 2018. Diffusion Convolutional Recurrent Neural Network: Data-driven traffic forecasting. In *International Conference on Learning Representations (ICLR 2018)*.https://doi.org/10.48550/arXiv.1707.01926.

Liao C, Chen X. 2025. A meta-learning approach to improving transferability for freeway traffic crash risk prediction. *Digital Transportation and Safety* **4(1):** 21−30. https://doi.org/10.48130/dts-0024-0027.

Ma X, Karimpour A, Wu YJ. 2025. Data-driven transfer learning framework for estimating on-ramp and off-ramp traffic flows. *Journal of Intelligent Transportation Systems: Technology, Planning, and Operations*, **29(1):** 67–80. https://doi.org/10.1080/15472450.2023.2301696.

Maghrour Zefreh M, Torok A. 2018. Single loop detector data validation and imputation of missing data. *Measurement*, **116:** 193–198. https://doi.org/10.1016/j.measurement.2017.10.066.

Pan SJ, Yang Q. 2010. A survey on transfer learning. *IEEE Transactions on Knowledge and Data Engineering*, **22(10):** 1345–1359. https://doi.org/10.1109/TKDE.2009.191.

Papageorgiou M, Haj-Salem H, Blosseville J-M. 1991. ALINEA: A local feedback control law for on-ramp metering. *Transportation Research Record*, **1320:** 58–64. https://onlinepubs.trb.org/Onlinepubs/trr/1991/1320/1320-008.pdf.

Papageorgiou M, Kotsialos A. 2002. Freeway ramp metering: An overview. *IEEE Transactions on Intelligent Transportation Systems*, **3(4):** 271–281. https://doi.org/10.1109/TITS.2002.806803.

Vlahogianni EI, Karlaftis MG, Golias JC. 2014. Short-term traffic forecasting: Where we are and where we're going. *Transportation Research Part C*, **43(1):** 3–19. https://doi.org/10.1016/j.trc.2014.01.005

Weiss K, Khoshgoftaar TM, Wang D. 2016. A survey of transfer learning. *Journal of Big Data*, **3(9).** https://doi.org/10.1186/s40537-016-0043-6.

Yu B, Yin H, Zhu Z. 2018. Spatio-temporal graph convolutional networks: A deep learning framework for traffic forecasting. In *Proceedings of the International Joint Conference on Artificial Intelligence (IJCAI 2018)*, pp. 3634-3640. https://doi.org/10.24963/ijcai.2018/505.

Zhang Z, Yang H, Yang X. 2023. A transfer learning–based LSTM for traffic flow prediction with missing data. *Journal of Transportation Engineering, Part A: Systems*, **149(10):** https://doi.org/10.1061/JTEPBS.TEENG-7638.

ISSN 2074-0867
EISSN 3135-1115